Role Of Impurities On Deformation Of HCP Crystal: A Multi-Scale Approach

by

Mehul Anoopkumar Bhatia

A Dissertation Presented in Partial Fulfillment
of the Requirements for the Degree
Doctor of Philosophy

Approved November 2014 by the
Graduate Supervisory Committee:

Kiran Solanki, Chair
Pedro Peralta
Hanqing Jiang
Narayanan Neithalath
Jagannathan Rajagopalan

ARIZONA STATE UNIVERSITY

December 2014

ABSTRACT

Commercially pure (CP) and extra low interstitial (ELI) grade Ti-alloys present excellent corrosion resistance, lightweight, and formability making them attractive materials for expanded use in transportation and medical applications. However, the strength and toughness of CP titanium are affected by relatively small variations in their impurity/solute content (IC), e.g., O, Al, and V. This increase in strength is due to the fact that the solute either increases the critical stress required for the prismatic slip systems $(\{10\bar{1}0\}\langle 1\bar{2}10\rangle)$ or activates another slip system $(\{0001\}\langle 11\bar{2}0\rangle, \{10\bar{1}1\}\langle 11\bar{2}0\rangle)$. In particular, solute additions such as O can effectively strengthen the alloy but with an attendant loss in ductility by changing the behavior from wavy (cross slip) to planar nature. In order to understand the underlying behavior of strengthening by solutes, it is important to understand the atomic scale mechanism. This dissertation aims to address this knowledge gap through a synergistic combination of density functional theory (DFT) and molecular dynamics. Further, due to the long-range strain fields of the dislocations and the periodicity of the DFT simulation cells, it is difficult to apply ab initio simulations to study the dislocation core structure. To alleviate this issue we developed a multiscale quantum mechanics/molecular mechanics approach (QM/MM) to study the dislocation core. We use the developed QM/MM method to study the pipe diffusion along a prismatic edge dislocation core. Complementary to the atomistic simulations, the Semi-discrete Variational Peierls-Nabarro model (SVPN) was also used to analyze the dislocation core structure and mobility. The chemical interaction between the solute/impurity and the dislocation core is captured by the so-called generalized stacking fault energy (GSFE) surface which was determined from DFT-VASP calculations. By

taking the chemical interaction into consideration the SVPN model can predict the dislocation core structure and mobility in the presence and absence of the solute/impurity and thus reveal the effect of impurity/solute on the softening/hardening behavior in α-Ti. Finally, to study the interaction of the dislocation core with other planar defects such as grain boundaries (GB), we develop an automated method to theoretically generate GBs in HCP type materials.

DEDICATION

I dedicate this dissertation to four pillars of my life, my mother, my wife and my two sisters.

ACKNOWLEDGMENTS

I would like to express sincere gratitude to the many people without whose selfless assistance, this dissertation could not have materialized. First, I would like to thank Prof. K.N. Solanki, my advisor, for his guidance, countless hours of reading, encouraging, helping, believing and patiently working with me throughout this research. Next, expressed appreciation is also due to my committee members Prof. P. Peralta, Prof. N. Neithalath, Prof. J. Rajagopalan and Prof. H. Jiang for their support and suggestions throughout my dissertation. I would like to extend special thanks to my colleagues Mr. I. Adlakha, Ms. M. Rajagopalan, Mr. S. Turnage, Mr. M. Azarnoush and Mr. B. Gholami for their valuable suggestions. I would also like to thank:

- All the group members for the useful suggestions and inspiring environment, specifically, Ilaksh, Vipin and Sudhansu for the helpful discussions.
- My friends for their direct contribution to my progress at different stages of my Ph.D.
- My wife for her belief in me and her support that led to the completion of the program requirements after marriage.
- My parents for their patient co-operation during the long course.

Finally, I also want to thank the support of the AFOSR under grant FA9550-13-1-0144, Program Manager Dr. David Stargel, for funding this research.

TABLE OF CONTENTS

Page

CHAPTER Page

CHAPTER Page

CHAPTER Page

APPENDIX

LIST OF TABLES

LIST OF FIGURES

Figure Page

Figure Page

Figure Page

Figure Page

CHAPTER 1

1 MOTIVATION

Titanium (Ti) and its alloys have been traditionally used for structural applications in automotive, aerospace, and biomedical applications due to their high strength-to-weight ratio (Leyens and Peters 2003; Davis 1990). Commercially pure (CP) and extra low interstitial (ELI) Ti-alloys in particular are attractive materials due to their excellent corrosion resistance, light weight, and formability. However, the strength and toughness of these alloys are affected by relatively small variations in their impurity content (IC), e.g., oxygen (O). Specifically, it has been shown that IC can cause a material to either harden or soften by interacting with dislocations or twins (Churchman 1954; Cerreta et al. 2006; Dallas R. Trinkle and Woodward 2005; Trinkle III 2003; Zeng and Bieler 2005; Brandes et al. 2012; Dong and Li 2000; Liu and Welsch 1988; Okabe, Oishi, and Ono 1992), as shown in Figure 1a. Table 1 lists the compositions for four common CP Ti alloys (ASTM grades 1-4) along with values for elongation, ultimate strength, and yield strength (Davis 1990). A comparison of the properties and compositions listed in Table 1 shows that a relatively small increase in the oxygen impurity content results in a significant increase in the mechanical strength. Figure 1a further shows that the same increases in oxygen content give rise to a pronounced decrease in room-temperature ductility. Notably with higher percentages of IC, a transition from wavy to planar dislocation slip has been reported (Leyens and Peters 2003).

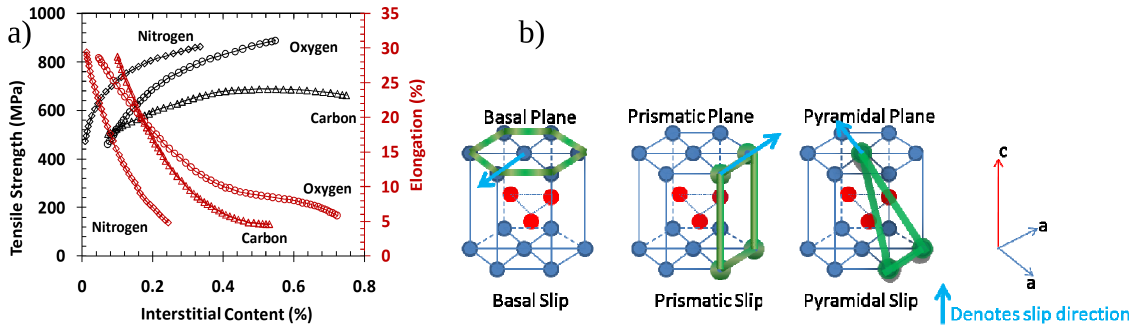

Figure 1: a) Effect of interstitial-element content on strength and ductility of unalloyed Ti (Davis 1990), and b) slip planes of Ti (Leyens and Peters 2003).

While the origin of impurity effects on the mechanical properties of CP and ELI Ti-alloys has been well documented (Leyens and Peters 2003; Davis 1990; Churchman 1954; Cerreta et al. 2006; Dallas R. Trinkle and Woodward 2005; Trinkle III 2003; Zeng and Bieler 2005; Brandes et al. 2012; Dong and Li 2000; Liu and Welsch 1988; Okabe, Oishi, and Ono 1992; Hanson 1986; Vitek and Paidar 2008; Richard G. Hennig et al. 2005; Albaret, Finocchi, and Noguera 1999; Minato et al. 2009; Rogers Jr et al. 1986; Stringer 1960; Bieler, Glavicic, and Semiatin 2002) remarkably there have been few systematic studies exploring the effect of IC on the deformation mechanisms. In fact, a recent macroscopic experimental study shows significant tension-compression strength asymmetry for high oxygen content CP-Ti (Brandes et al. 2012). However, the exact physical mechanisms and mechanistic parameters, e.g., stress dependence of critical resolved shear stresses (CRSSs), related to this strength asymmetry are still unclear. This work aims to address this knowledge gap through a synergistic combination of first principle calculations and molecular dynamics (MD) simulations of pure Ti with relatively small amounts of IC (e.g., oxygen, vanadium, aluminum etc.).

Table 1: Composition, ultimate strength, and elongation for CP Ti ASTM grades 1-4 (Leyens and Peters 2003).

Designation	**Wt.%H**	**Wt. %C**	**Wt. %O**	**Wt. %N**	**Wt. %Fe**	**Ultimate strength (MPa)**	**Elongation (%)**
Grade 1	0.01	0.1	0.18	0.03	0.2	240	24
Grade 2	0.01	0.1	0.25	0.03	0.3	343	20
Grade 3	0.01	0.1	0.35	0.05	0.3	440	18
Grade 4	0.01	0.1	0.40	0.05	0.5	550	20

CHAPTER 2

2 BACKGROUND AND SPECIFIC RESEARCH OBJECTIVE

2.1 BACKGROUND

Churchman (Churchman 1954) experimentally observed that deformation in CP Ti is governed by the three slip systems shown in Figure 1b (also ref. (Churchman 1954; Brandes et al. 2012; Vitek and Paidar 2008; Partridge 2013)). He also demonstrated that interstitial impurities not only affect the magnitude of CRSSs, but also the relative differences in the CRSS values for the three slip systems, where $\{10\bar{1}0\}\langle 1\bar{2}10\rangle$ is the principal slip system in Ti (Churchman 1954). Furthermore, using a hard sphere model, he proposed that interstitial sites occupied by oxygen atoms obstructs the slip activity on the basal and prismatic planes; resulting in an increase in the <c+a> dislocation activities. Similarly, Naka et al. (Naka et al. 1988) have shown that interstitial impurities provide a very strong hardening effect at lower temperatures ($T \leq 500$ K) and observed cross slip of <a> type dislocation from the prism to pyramidal planes. Further, they concluded breakdown on the Schmidt law due to the presence of a non-planar core structure (Figure 2).

The CRSS for <c+a> dislocations has been measured to be several times (~8 times) larger than that for <a>-type slip on prismatic and basal planes (Churchman 1954; Brandes et al. 2012; Vitek and Paidar 2008; Partridge 2013), see Figure 3. In addition, the microstructure of the alloy makes a difference, for example in α/α+β alloys, the alpha phase will deform one way and the lamellar α+β will deform in another (Bieler, Glavicic, and Semiatin 2002). The secondary slip is in the $\langle 11\bar{2}0\rangle$ direction of the basal $\{0001\}$

plane. Other systems present are pyramidal slip in the $\langle 11\bar{2}0\rangle$ and $\langle 11\bar{2}\bar{3}\rangle$ directions of the $\{10\bar{1}1\}$ plane and in the $\langle 11\bar{2}\bar{3}\rangle$ direction of the $\{11\bar{2}2\}$ plane. Accurate atomistic modeling of non-basal defects is essential to correctly predict deformation behavior of hexagonal close packed (HCP) metals and alloys (Dallas R. Trinkle and Woodward 2005; Trinkle III 2003; Vitek and Paidar 2008; Richard G. Hennig et al. 2005; Vitek and Igarashi 1991). However, due to the long-range strain fields of the dislocations and the periodicity of the density functional theory (DFT) simulation cells, it is difficult to apply ab initio simulations to study dislocation core structure (Dallas R. Trinkle and Woodward 2005; Trinkle III 2003; D. R. Trinkle 2007), especially with non-planar spreading of the dislocation cores. Stacking faults on the other hand are more straightforwardly represented in an ab initio model (Vitek and Paidar 2008; Vitek and Igarashi 1991; Yamaguchi, Shiga, and Kaburaki 2005; Van Swygenhoven, Derlet, and Frøseth 2004; G. Lu et al. 2000a; X. Wu, Wang, and Wang 2010) or modeling planar defects using coupled quantum and molecular mechanics (Y. Zhao and Lu 2011).

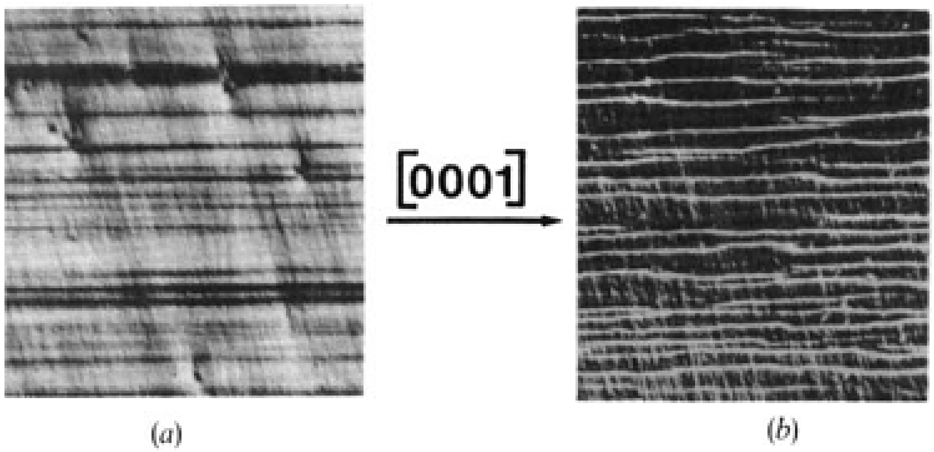

Figure 2: slip traces on compression specimen at a) 77 K and b) 472 K. Composition of specimen is Ti+3270 at.p.p.m O. Note transition from a planar to wavy nature of slip at different temperature. Figure adapted from (Naka et al. 1988)

In high strength grade Ti-alloys oxygen and iron are intentionally added to the initial amounts already present in the melt to provide extra strength (Leyens and Peters 2003; Davis 1990). The addition of oxygen improves the corrosion and wear resistance of Ti and its alloys (Davis 1990; Stringer 1960). However, at elevated temperatures the oxide layer at the Ti surface will grow and oxygen will rapidly diffuse into the base metal (Liu and Welsch 1988; Rogers Jr et al. 1986; Rogers Jr et al. 1988; Thorwarth, Mändl, and Rauschenbach 2000) instigating hardening of the Ti (Dong and Li 2000). On the other hand, at lower temperatures and even with low concentration oxygen can initiate crack formation (Dong and Li 2000; Thorwarth, Mändl, and Rauschenbach 2000). Also, impurities such as oxygen and nitrogen render slip more difficult on two of the three slip planes in Ti (Churchman 1954; Brandes et al. 2012; Conrad 1981; Ogden and Jaffee 1955). Cerreta et al. (Cerreta et al. 2006) found that 1 at.% oxygen impurities in Ti would completely suppress the pressure-driven (shock-induced) transformation from the α (HCP) to the ω (simple hexagonal) phase in Ti. Ti-alloys with higher interstitial content also show cleavage on the basal plane of the HCP structure (Churchman 1954), in contrast to a ductile fracture (Davis 1990; Churchman 1954). Twinning is an additional deformation mode observed most commonly in Ti-alloys with less IC. As the IC increases, however, the degree of twinning generally decreases in Ti (Conrad 1981; Ogden and Jaffee 1955)**.** Recent experimental studies of the deformation behavior in Ti-alloys (Zeng and Bieler 2005; Bieler et al. 2009; Leyun Wang et al. 2011; Y. M. Wang et al. 2007; Y. J. Chen et al. 2010; May 2010; Xing and Sun 2008) have revealed that nanoscale interactions are the underlying cause for this behavior.

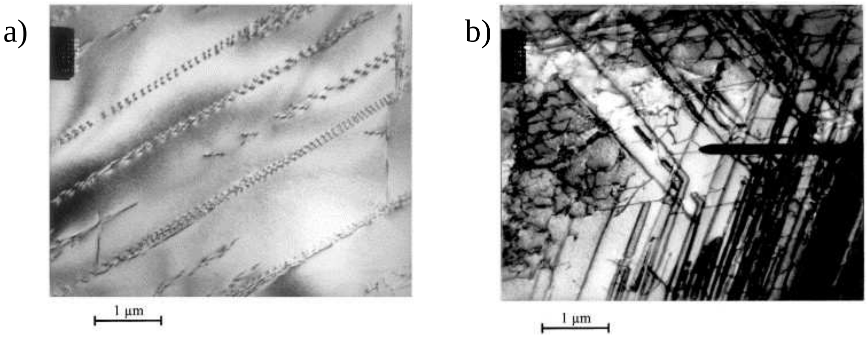

Figure 3: a) Prismatic dislocations with edge character in Ti; and b) <a> and <c+a> dislocations with edge or mixed character in Ti+1000 ppm O. Adapted from Zaefferer 2003.

2.2 RESEARCH OBJECTIVE

The pronounced effects of IC on the mechanical properties shown in Table 1 and Figure 1 are thus accompanied by qualitative changes in the mechanisms underlying strength, ductility, and creep behavior. These observations suggest that, in principle, it should be possible to strongly influence the mechanical strength-ductility relationship in Ti through the addition of alloying elements and/or through microstructural changes selected to counteract or enhance the impurity effects influencing the underlying mechanisms of deformation and failure. Such a strategy requires an expanded understanding of the atomistic origins of the impurity effects reviewed above. As such, this dissertation addresses three fundamental questions concerning the mechanisms underlying these deformation mechanism and impurity effects on deformation according to the following topics:

1. Role of IC on the ratio of stacking fault energies (SFEs) on prismatic, pyramidal, and basal planes.
2. Effect of IC on Peierls stresses, and the tension-compression asymmetry observed

during deformation.

3. The role of grain boundary (GB) character on the nucleation and interaction behavior of slip deformation.

Also, this work provides a novel database on chemo-mechanical effects, i.e., IC contributions, into the strength and ductility response (structure-property relationships) to add insight into macroscale modeling (e.g. dislocation drag coefficient, dislocation mobility etc.). The research objectives of this proposal are as follows:

- To investigate and compare the fundamental deformation mechanisms for Ti- with known amounts of IC additions; and
- To identify the nanoscale mechanisms that enhance the impurity effects, including synergistic interactions between solutes and defects, such as dislocations, grain boundaries etc.

Towards this goal, we will

- Develop a coupled quantum and molecular mechanics framework to the direct effect of IC on dislocation core stability and other core properties.
- Quantify a composition-dependent generalized stacking fault energy (GSFE) landscape using DFT to address the deformation anisotropy.
- Encourage future work to quantify dislocation-grain boundary interactions and correlate the subsequent deformation event in the neighboring grain with the help of Luster Morris and Fatemi Socie parameters.

This research and the resulting generic crystal plasticity principles and parameters related to the CRSS are expected to provide a foundation for designing and accelerating adoption of future Ti-alloys that are cost-effective, energy-efficient, and structurally-tailored for widespread applications, such as powertrain components for the transportation sector and/or prosthetic components for biomedical applications.

To meet these objectives this dissertation is divided into two parts. The first part focuses on implicit and explicit modelling of different dislocation core structures. In the implicit method, the generalized stacking fault energy (GSFE) is used to compute dislocation core properties (Chapters 3 and 5); whereas, in the explicit method we directly model different dislocation core structures (Chapter 4). The second part focuses on grain boundary modelling (Chapter 6), solute effects (Chapter 7) and dislocation-GB interactions (Chapter 8). Finally, recommendations for future research are also presented (Chapter 9).

CHAPTER 3

3 DISLOCATION CORE STRUCTURES: GENERALIZED STACKING FAULT ENERGY (GSFE) APPROACH

3.1 INTRODUCTION

Deformation in titanium is plastically anisotropic and dictated by dislocation and twinning mechanisms. The most common slip modes in titanium are $\{10\bar{1}0\}$ (prism), $\{10\bar{1}1\}$ (pyramidal), and (0001) (basal) along the $< 11\bar{2}0 >$ (<a> direction) as the slip direction. Hence, there are four independent slip systems with three glide planes. However, to maintain the deformation compatibility (Chichili, Ramesh, and Hemker 1998) of five independent slip systems, twinning occur during plastic deformation which gives rise to the plastic anisotropy (Leclercq, Nguy, and Bensussan 1989). Earlier work of Akhtar (Akhtar 1975) and Teghtsoonian (Akhtar and Teghtsoonian 1975) using single crystal titanium concluded that deformation at lower temperatures involves twinning; whereas dislocation on the prismatic and basal planes was observed at higher temperatures.

Dislocation motion in response to external load plays a crucial role in understanding the plastic deformation of metallic material. Over the last few decades, the long range elastic strain fields of a dislocation core have been well studied using continuum theories (Hirth and Lothe 1982), but continuum theory breaks down near the dislocation core. In the past to circumvent this issue, two approaches have been employed to study the dislocation core properties: a) the first approach utilizes the SVPN model, but it fails to measure the dislocation velocity and also hardening due to the dislocation-dislocation interaction. The second approach is direct modeling of the dislocation core using first principles methods or empirical interatomic potential. In this study, we used both the approaches to study the <a> type dislocation core in titanium. Studies of dislocation cores with various interatomic potentials have been discussed in Chapter 4. Overall, the aim of this chapter is to investigate the <a> type dislocation lying on the basal, prismatic, and pyramidal planes using first principle, molecular static, and dynamic methods along with the SVPN model.

3.2 METHODOLOGY

Here, DFT calculations to characterizes GSFE curves were performed using the Vienna Ab-initio Simulation Package (VASP) plane wave electronic structure code (G. Kresse and Hafner 1993; G. Kresse and Furthmüller 1996a; G. Kresse and Furthmüller 1996b). Projector augmented wave (PAW) (P. E. Blöchl 1994; G. Kresse and Joubert 1999) potentials were used to represent the nuclei and core electrons up to the 3p shell with $3d^3$ and $4s^1$ as valence electrons for α-Ti. Exchange and correlation was treated with GGA using the PBE (Perdew, Burke, and Ernzerhof 1997) form with an energy cutoff of 289 eV and the Monkhorst Pack k-point with gamma mesh of 1x10x16, 1x12x14, and 1x16x9 for the prismatic, basal, and the pyramidal planes, respectively, were employed. The ionic relaxation was carried out using a conjugate gradient algorithm with 30 meV/Å force and 1 meV energy convergence criteria.

For GSFE curves from semi-empirical potentials, a parallel molecular dynamics code (Large-scale Atomic/Molecular Massively Parallel Simulator, LAMMPS (Plimpton

1995)) was used. Here, we tested four different interatomic potentials which are based on the embedded atom method (EAM) (Daw and Baskes 1984), FS (Ercolessi and Adams 1994), and MEAM (Baskes 1992) methods. The first potential was developed by Zope and Mishin (Zope and Mishin 2003) based on the EAM method. The database of this potential includes experimental lattice and elastic constants and ab initio crystal structure volume pressure data for fitting. The second potential was developed by Ackland (Ackland 1992) based on the FS method. This potential was fitted using point defects, the surface energies of basal, prismatic, and pyramidal surfaces, as well as the stacking fault energies of the basal and pyramidal planes. The third and fourth potentials were developed by Hennig (R. G. Hennig et al. 2008) where one of the potentials is a spline based MEAM potential and another is a spline based MEAM potential with Stillinger Weber (Stillinger and Weber 1985) functional form. The fitting database for this potential includes energies, forces, elastic constants, and defects for various Ti phases and also energies of transformation paths from α to ω. Calculated GSFE serves as the interfacial term in the SVPN method described in Eq. 3 of Section 3 required for calculation of dislocation core properties. Moreover, Table 2 shows the comparison of some of the structure properties obtained using different empirical potentials with experimental and DFT work.

Table 2: Unit cell parameters and elastic properties of a α-Ti single crystal obtained using our own first principles calculations (at 0 K), various empirical potentials, and their comparisons with available experimental data (at ~300 K)(Fisher and Renken 1964).

	a (Å)	**c (Å)**	**Young's Modulus (GPa)**	**Shear Modulus (GPa)**	**Poisson's ratio**
Experiment	2.951	4.686	121.556	46.500	0.307
DFT	2.938	4.657	128.091	48.960	0.308
Mishin EAM	2.951	4.686	99.727	36.935	0.350
Ackland FS	2.967	4.720	103.938	38.785	0.340
Hennig Spline	2.935	4.673	84.731	30.783	0.376
Hennig Swspline	2.940	4.669	84.141	30.594	0.375

3.3 SEMI DISCRETE VARIATIONAL PEIERLS NABARRO MODEL (SVPN):

The non-atomistic P-N model describes dislocation core structure in the continuum scale framework and has been used to estimate the critical stress needed for the dislocation motion, i.e., the Peierls stress (G. Lu 2005; Vitek 2005; Bulatov and Kaxiras 1997b; Peierls 1940; Nabarro 1947). However, the original P-N model was found to be slightly inaccurate in estimating core properties of real materials due to various modeling assumptions (see detail in G. Lu 2005; Bulatov and Kaxiras 1997b; G. Lu et al. 2000b). The difference between periodicity of the Peierls stress and dislocation barrier, in general (Christian and Vítek 1970; J. N. Wang 1996; Schoeck 1999), lead to the development of the SVPN model (G. Lu 2005; Bulatov and Kaxiras 1997b; G. Lu et al. 2000b).

The SVPN model has recently been presented to study dislocation core properties (G. Lu et al. 2000b; Bulatov and Kaxiras 1997b). In this method, the equilibrium structure can be obtained by minimizing the total energy (U_{dis}) with respect to the dislocation density or the disregistry vector using numerical methods such as the conjugate gradient method. The total energy (U_{dis}) can be described as

$$U_{dis} = U_{elastic} + U_{misfit} + U_{stress} + Kb^2 ln\, L. \tag{1}$$

where $\boldsymbol{L}$ and $\boldsymbol{b}$ are the outer cutoff radius for the elastic energy and magnitude of the Burgers vector, respectively. The first term in Eq. (1) is the discretized elastic energy, $U_{elastic}$, and is given by

$$U_{elastic} = \sum_{i,j} \frac{1}{2}\, \chi_{ij}\, [K_e\left(\rho_i^{(1)}\rho_j^{(1)} + \rho_i^{(2)}\rho_j^{(2)}\right) + K_s\rho_i^{(3)}\rho_j^{(3)}] \tag{2}$$

The second term in Eq. (1) is the interfacial energy, U_{msifit}, which is a function of a disregistry vector ($\overline{f_i}$) and is given by

$$U_{misfit} = \sum_i \Delta x \gamma_3(\overline{f_i}) \tag{3}$$

The core energy, (U_{core}), is the sum of elastic and interfacial energies which are the dislocation configuration-dependent part of the total energy and is described as

$$U_{core} = U_{elastic} + U_{misfit} \tag{4}$$

The third term in Eq. (1) describes the plastic work performed on the dislocation line, which is given by

$$U_{stress} = -\sum_{i,l} \frac{x_i^2 - x_{i-1}^2}{2}\, (\rho_i^{(l)}\tau_i^{(l)}) \tag{5}$$

The last term in Eq. (1), i.e., $Kb^2 ln\, L$, is independent of the disregistry (dislocation density). In Equations (1-5), the superscript *l=1, 2 and 3* corresponds to the edge, vertical, and screw components of variables, respectively, and subscript *i* represents the i-th nodal point. The general interplanar dislocation density at the i-th nodal point, $\rho_i^{(l)}$, is defined as $\rho_i^{(l)} = (f_i^{(l)} - f_{i-1}^{(l)})/(x_i - x_{i-1})$ where $f_i^{(l)}$ and x_i are the disregistry vector and the coordinate of the i-th nodal point (atomic row), respectively, and $\gamma_3(\overline{f_i})$ is the three dimensional misfit potential computed using DFT (Hohenberg and Kohn 1964; Kohn and Sham 1965). The corresponding components of the applied stress interacting with $\rho_i^{(1)}$, $\rho_i^{(2)}$ and $\rho_i^{(3)}$ are $\tau^{(1)} = \sigma_{21}$, $\tau^{(2)} = \sigma_{22}$ and $\tau^{(3)} = \sigma_{23}$, respectively. K is the pre-logarithmic energy factor,

$$K = \frac{\mu}{2\pi}\left(\frac{sin^2\theta}{1-\upsilon} + cos^2\theta\right) \tag{6}$$

where $\boldsymbol{\theta}$ is the angle between the Burgers vector and the dislocation line. Therefore the energy factor for an edge and a screw dislocation are $K_e = \mu/(2\pi(1-\nu))$ and $K_s = \mu/2\pi$, respectively. μ and ν are the shear modulus and Poisson's ratio, correspondingly. The x-axis is considered the dislocation gliding direction. The rest of the quantities can be computed by the following equations

$$\chi_{ij} = \frac{3}{2}\phi_{i,i-1}\phi_{j,j-1} + \psi_{i-1,j-1} + \psi_{i,j} - \psi_{i,j-1} - \psi_{j,i-1} \tag{7}$$

$$\phi_{i,j} = x_i - x_j \tag{8}$$

$$\psi_{i,j} = \frac{1}{2}\phi_{i,j}^2 \ln|\phi_{i,j}| \tag{9}$$

The interfacial term (Eq. 3) requires an estimation of two-dimensional displacement parallel to the slip plane, i.e., the generalized stacking fault energy (GSFE). The GSFE was first introduced by Christian and Vitek (Christian and Vítek 1970) who suggested that under applied stress alongside a certain plane, a crystal is cut into two parts that have relative displacements with respect to each other resulting in stacking faults. These faults produce an extra energy which can be computed using DFT.

3.4 DISLOCATION CORE PROPERTIES: GSFE

Figure 4 shows the generalized stacking fault energy curves on basal, prismatic, and pyramidal planes as a function of the applied shear displacement computed with DFT and empirical potentials. Legrand (P. B. Legrand 1984) investigated the slip system in transition and non-transition metals theoretically and suggested a criteria $R = {}_{basal}C_{66} \big/ {}_{prism}C_{44}$ to predict the dominant slip system. This ratio explains the relative easiness of dislocation dissociation in the corresponding plane. If value of R<1, basal slip dominates. If R>1 prismatic slip dominates, and for R≅1 both slip systems are activated. Table 3 shows the comparison of stacking fault energies for the basal and prismatic planes along with the elastic properties computed using different potentials. Legrand never found a stable prismatic stacking fault as predicted by DFT calculation in Figure 8c. Instead he used an average value of ${}_{prism}$ along the $< 1\bar{2}10 >$ direction which resulted in a little higher value of 2.5 in his calculation. Moreover, none of the potentials are able to capture the stable stacking fault energy for the prismatic plane as predicted by DFT (valley in the figure) in Figure 4c. Furthermore, all potentials predict Legrand's ratio R<1 (Table 3) which concludes the basal slip as dominant slip and contradicts with the findings of Ghazisaeidi and Trinkle (Ghazisaeidi and Trinkle 2012) where they were able to reproduce preferential prismatic screw dislocation core structure with Hennig (R.

G. Hennig et al. 2008) MEAM potential. Moreover, it will be shown in chapter 4 that the dislocation core energy on the prismatic plane has lower energy than the dislocation core energy on the basal plane, and hence, raising questions to the validity of Legrand's criteria. To overcome this we employed the SVPN method which takes the whole GSFE into consideration instead of just the stacking fault (I_2) on the basal and prismatic planes.

Table 3: Stacking fault on the basal and prismatic planes and elastic properties of a α-Ti single crystal obtained using our own first principles calculations (at 0 K), various empirical potentials, and their comparison with Legrand calculation(P. B. Legrand 1984).

	$\gamma_{basal}(I_2)$ (mJ/m^2)	γ_{prism} (mJ/m^2)	C_{44} (GPa)	C_{66} (GPa)	Legrand Ratio R
Legrand	290.00	110.00	50	47.4	2.50
DFT	278.45	237.00	43.03	43.52	1.19
Mishin EAM	65.66	268.06	26.04	28.20	0.27
Ackland FS	71.29	266.11	24.31	26.35	0.29
Hennig Spline	191.49	277.00	17.40	18.02	0.72
Hennig Swspline	164.19	281.69	17.44	18.28	0.61

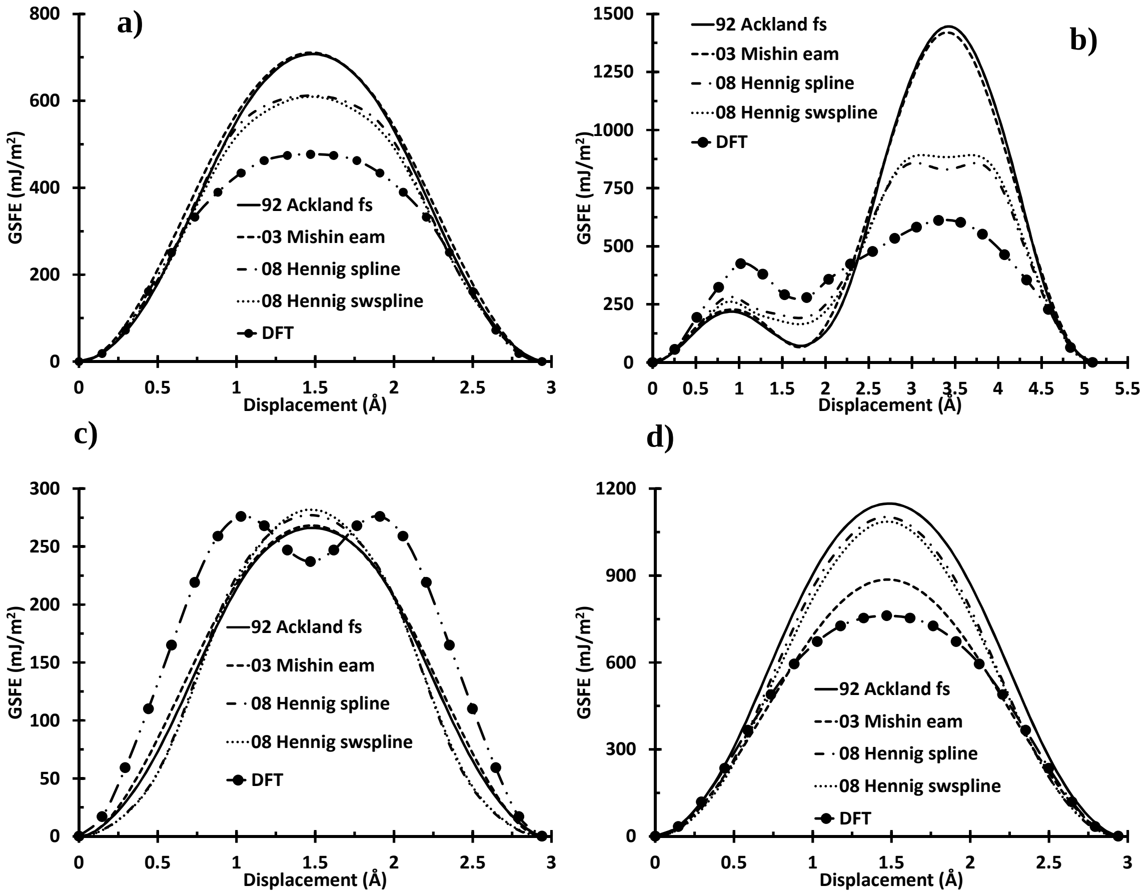

Figure 4: The stacking fault energy as a function of applied shear displacement a) along the $[1\bar{2}10]$ direction on the basal plane, b) along the $[10\bar{1}0]$ direction on the basal plane, c) along the $[1\bar{2}10]$ direction on the prismatic plane, and d) along the $[1\bar{2}10]$ direction on the pyramidal plane.

In order to use SVPN to find the core energetics and Peierls stress for different types of dislocations along the basal, prismatic, and pyramidal planes, one needs to find the dislocation dissociation reactions. Dislocation dissociation reactions are on the basal plane (Figure 4b) and GSFE surfaces (Pei et al. 2013). In each slip system there is only one absolute maximum value of GSFE along perfect dislocations named as the unstable stacking fault, *USF*, with energy γ_{usf}. In other directions, the stacking fault energy has both local minimum and maximum values. The local minimum stacking fault energy is the so-called stable or intrinsic stacking fault, *ISF*, with energy γ_{isf}. These local minima and local maxima of stacking fault energies allow the dissociation of the perfect dislocations into two imperfect dislocations with partial Burgers vectors. Having found perfect dislocation ($\boldsymbol{b}$) and one partial dislocation ($\boldsymbol{b_1}$), the other partial dislocation ($\boldsymbol{b_2}$) can be perceived by subtracting the two other dislocations as seen for basal slip. Table 4 lists the value of Pierels stress computed for different interatomic potentials and DFT. With different interatomic potentials we observe the basal slip to be the dominant slip which contradicts experimental and first principle calculation predictions of prismatic slip as the dominant slip. This discrepancy can be attributed to the prediction of lower stable stacking fault energy, γ_{isf}, with the potentials compared to first principle. Hence, there is a need of a development of a better potential which takes stacking fault energy and other defects calculated from first principles in the database of the fitting procedure.

Table 4: Table of Pierels stress calculated using a semi discrete variational Peierls Nabarro method for different interatomic potentials.

Method	**Peierls Stress (MPa)**		
	Basal	**Prismatic**	**Pyramidal**
DFT	40	24	144
Mishin EAM	14	36	170
Ackland FS	14	36	213
Hennig Spline	27	48	213
Hennig Swspline	26	48	240

Next, we employ DFT method to study the effect of solutes/impurities on the dislocation core behavior through so-called GSFE surfaces. Figure 5 shows the effect of substitution solute on the generalized stacking fault energy. There is a reduction in energy and more splitting of the core with the addition of aluminum as compared to without aluminum on the prismatic and basal planes (γ_{isf}). Whereas, with the addition of vanadium, there is an increase in energy on the prismatic plane and a decrease in energy of the basal plane (γ_{isf}). Moreover, aluminum decreases Peierls stresses on the basal plane from 40 MPa to 26 MPa and on the prismatic plane from 24 MPa to 18 MPa. Whereas, vanadium increases Peierls stresses on the prismatic plane from 24 MPa to 46 MPa and decreases Peierls stress on the basal plane from 40 MPa to 26 MPa. Hence, aluminum increases the ductility in titanium; whereas, vanadium changes the slip system from prismatic slip to basal slip. Moreover, vanadium increases strength in titanium by increasing the Peierls stress for the prismatic dislocation.

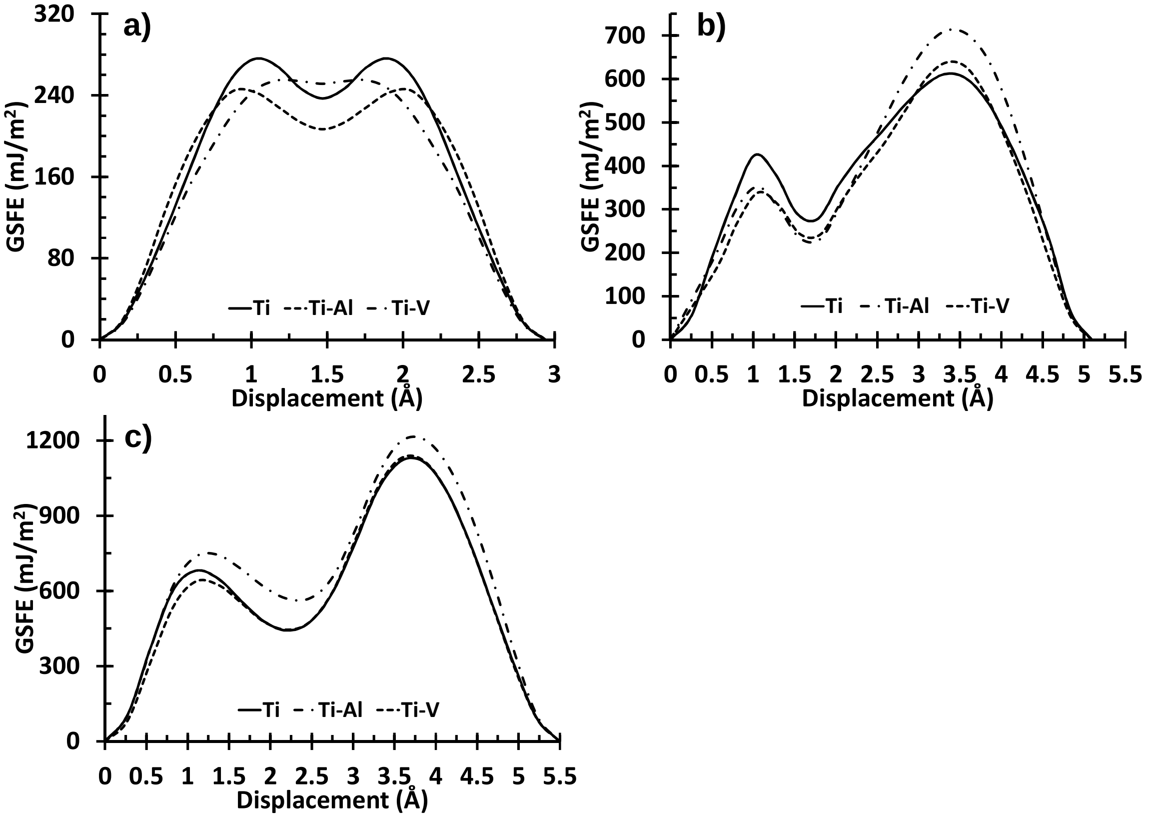

Figure 5: Stacking fault energy as a function of applied shear displacement with solute at the shear plane a) along the $[10\bar{1}0]$ direction on the basal plane, b) along the $[1\bar{2}10]$ direction on the prismatic plane, and c) along the $[11\bar{2}3]$ direction on the second order pyramidal plane.

3.5 SUMMARY

In summary, using first principles simulations we show that the prismatic plane has a metastable stacking fault at $\frac{a}{6} < 11\bar{2}0 >$ (Figure 4c), whereas the various interatomic potentials investigated fail to reproduce this behavior. Furthermore, we use the Legrand's ratio, R, and the Peierls stress calculations (using SVPN method) to show that interatomic potentials predict the basal to be a preferred slip system in Ti, which contradicts experimental observations and first principles prediction, i.e., the prismatic slip being the most preferred slip system. For the case of substitution solute strengthening, vanadium changes the preference of slip from the prismatic to basal (Figure 5); whereas, aluminum increases the ductility of <a> type dislocation and increases the Peierls barrier for <c+a> type dislocation. Hence, intuitively aluminum enhances the tension compression symmetry by increasing the barrier for <c+a> type dislocation and decreasing the barrier for <a> type dislocation. However, vanadium increases the tension compression asymmetry by increasing the Peierls barrier for <a> type dislocation on the prismatic plane and decreasing the barrier for <c+a> type dislocation. In the case of interstitial solute strengthening, oxygen increases the barrier for <a> type dislocation on the prismatic plane and decreases the barrier for <c+a> type dislocation as also seen in the experiment carried out by Zaefferer (Zaefferer 2003) and confirmed in Chapter 5.

CHAPTER 4

4 DISLOCATION CORE STRUCTURE: MOLECULAR STATIC AND DYNAMIC APPROACH

4.1 INTRODUCTION

In this chapter we discuss the direct modeling of the dislocation core at the atomic level using first principle or empirical potentials. The benefit of using an empirical interatomic potential for the dislocation core modeling is the gain in computational time and, hence, the ability to model bigger systems (~1 million atoms), but the drawback is that these potentials are fitted from a confined database and may not be able to describe the dislocation core due to involvement of large lattice distortion (bond breaking and bond formation) which requires a quantum mechanical description of the core. Moreover, even though the first principles descriptions of the dislocation core are more reliable and accurate, it is computationally very expensive.

In this chapter, we use atomistic tool to model explicitly the dislocation core structures, which are essential to correctly predict the deformation behavior of HCP metals and alloys (Dallas R. Trinkle and Woodward 2005; Vitek and Igarashi 1991; Trinkle III 2003; Vitek and Paidar 2008; Richard G. Hennig et al. 2005). The mechanical response of a material is govern by i) interactions between dislocations and ii) average dislocation velocity. Dislocation-dislocation interactions control hardening in the material as described in detail by Franciosi et al. (Franciosi, Berveiller, and Zaoui 1980) for FCC materials, and dislocation velocity controls the plastic flow in the material. Earlier works on a numerical investigation of dislocation mobility and core properties using molecular statics and dynamics were performed on FCC materials, such as Cu (Mordehai et al. 2003), Ni, and Al(Olmsted et al. 2005), on BCC materials like Mo (Chang et al. 2002) and Fe (Chaussidon, Fivel, and Rodney 2006; Bhatia, Groh, and Solanki 2014), and, recently, on HCP material like Mg (Groh et al. 2009). In open literature, dislocation core properties in titanium have been studied by Girshick et al. (Girshick, Pettifor, and Vitek 1998), Legrand (B. Legrand 1985), and Vitek and Igrashi (Vitek and Igarashi 1991) , but the dynamic properties of a dislocation has not been studied numerically. In this study, we used molecular statics and molecular dynamics to study the dissociation of core structure and numerically investigate the mobility rule for the titanium.

4.2 METHODOLOGY

For direct modeling of dislocation cores, the edge dislocation was created as described by Osetsky and Bacon (Osetsky and Bacon 2003) in LAMMPS (Plimpton 1995) using Mishin's EAM potential (Zope and Mishin 2003). The simulations were performed on a rectangular cell with y-axis oriented along the respective slip plane and x-axis oriented along the burger's vector $[1\bar{2}10]$ directions and z-axis along the dislocation line direction. The overall dimensions were: 293 Å x 468 Å x 51 Å for the basal dislocation, 293 Å x 511 Å x 46 Å for the prismatic dislocation and 293 Å x 233 Å x 85 Å for the pyramidal dislocation. During dynamic loading, the x and z direction were periodic; whereas, the y-direction was fixed and shear stresses ranging from 20MPa to 800MPa were applied along the x-direction (burger's direction) on the slip plane(y plane) for a temperature range of 100K – 1000K. In contrast, a screw dislocation was created using an elastic displacement field along the burger's vector direction (z direction) given by equation 10.

$$u_z = \frac{b}{2\pi} * arctan\ ({}^{y}/_{x}) \qquad (10)$$

The z-axis was oriented along the burger's vector $[1\bar{2}10]$ direction, and the y-axis was oriented along the normal to the slip plane direction. The overall dimensions were: 460 Å x 510 Å x 30 Å for the basal, prismatic, and pyramidal dislocations. During dynamic loading, only the z direction was periodic; whereas, the x and y-directions were fixed and shear stresses ranging from 20MPa to 800MPa were applied along the z-direction (burger's direction) on the slip plane (y plane) for a temperature range of 100k – 1000k.

4.3 EDGE DISLOCATION: STATIC AND DYNAMIC

To analyze the preference of a dislocation core spreading on the basal and prismatic planes, it is important to calculate dislocation energy. From anisotropic elasticity theory, the energy stored within a cylinder of radius R centered at the dislocation line is given by

$$E_{disl}(R) = \frac{Kb^2}{4\pi} * \ln\left(\frac{R}{r_0}\right) + E_{core} \qquad (11)$$

where E_{core} is the core energy, r_0 is the core radius, K is a constant which depends on elastic moduli and orientation, b is the burger's vector (in present case the lattice constant a), R is the radius of the cylinder.

Figure 6 shows the dislocation core energy as a function of ln(R/r_0). Figure 6 demonstrates the preferred edge dislocation core which is basal in the case of EAM and FS potentials; whereas, the MEAM potential predicts the prismatic plane as the preferred slip plane. These results also match with the prediction of the SVPN method where EAM and FS predict basal slip to be the dominant slip as opposed to prismatic slip seen in experiments. The dislocation core energy can be predicted by taking the limit of $\ln(R/r_0)$ which tends to zero. The dislocation core energies for the prismatic and basal planes are 0.52 eV/□ and 0.34 eV/□, 0.46 eV/□ and 0.34 eV/□, and -0.56 eV/□ and -0.35 eV/□ with EAM, FS, and MEAM potentials, respectively.

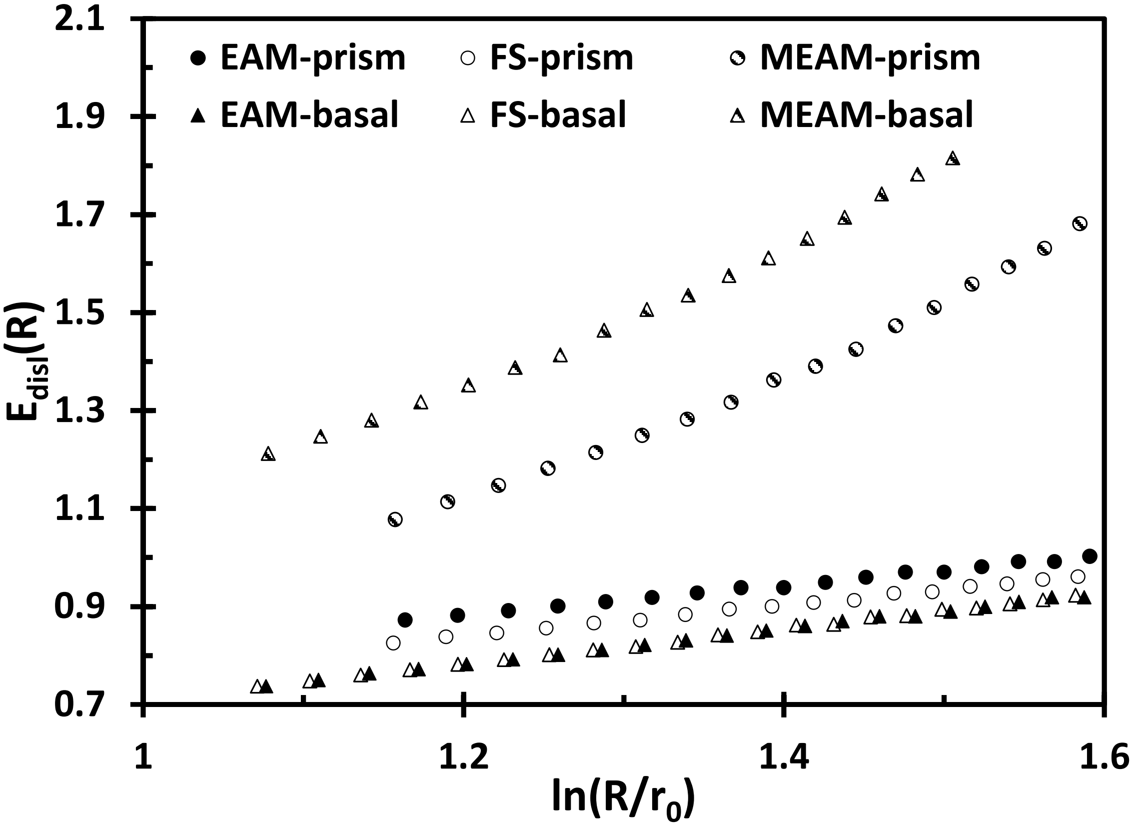

Figure 6: Energy of an edge dislocation stored within a cylinder of radius R as a function of ln(R/r). Filled points are EAM results. Open points are FS calculation, and half-filled points are MEAM results.

Figure 7 shows the dislocation core of an edge dislocation on the basal (Figure7a), prismatic (Figure7b), and pyramidal planes (Figure7c). The dislocation core along the basal plane dissociates into two partials with a stacking width of ~2.5nm between the two partials; whereas, the core width on the prismatic and pyramidal planes were 0.9 nm and 0.75 nm. Once a dislocation core is created and minimized with the conjugate gradient algorithm and energy criteria of 0.01 pico-eV/Å, a strain increment of 10^{-4} was applied on the top surface to calculate the Peierls stress with minimization criteria of 0.01 pico-eV/Å at each step until total strain was 1%. For the basal dislocation, a strain increment of 10^{-6} was applied to capture the stress. Figure 7d shows the shear stress vs. shear strain curve for an edge dislocation on the basal, prismatic, and pyramidal planes. The slope of the stress strain curve gives a value of C_{44} to be 27 GPa. Peierls stress was found to be 2.12 MPa, 25 MPa and 26 MPa for the basal, prismatic, and pyramidal, respectively. Based on the Peierls stress calculation, there is anisotropy seen in the slip system which suggests basal slip is an easy mode of deformation followed by prismatic and pyramidal which agrees with the prediction of SVPN model for the EAM potential. Once a dislocation starts motion, all the excess energy is dissipated in the form of oscillatory stress which is attributed to the boundary condition. The uncertainty related to Peierls stress calculation can be estimated by calculating back stress generated from the finite dimension and boundary condition which is given by ${}^{\mu b^2}/_{L^2}$. Hence uncertainty in Peierls stress was 2.7 MPa.

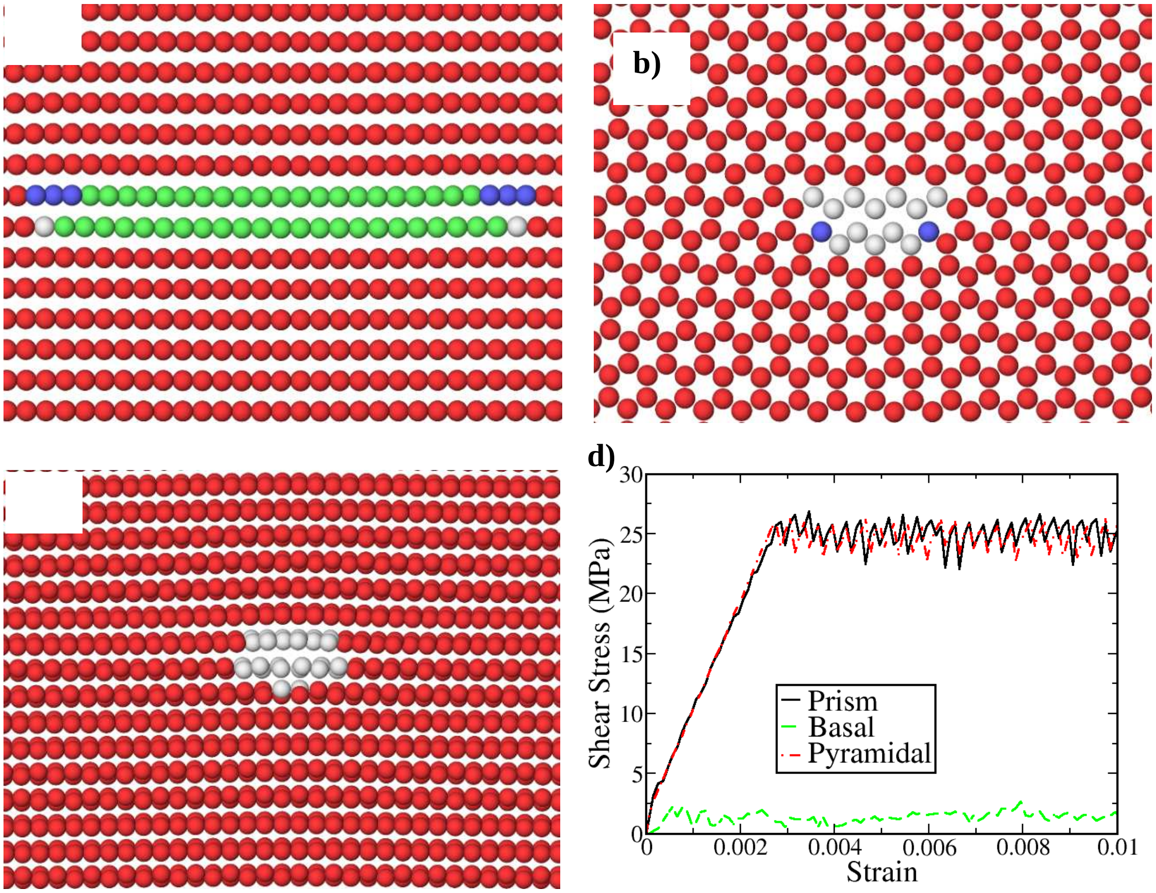

Figure 7: Edge dislocation core structure on a) basal plane b), prismatic plane, and c) pyramidal plane and d) Peierls stress as a function of strain for edge dislocation on the basal, prismatic, and pyramidal planes. Note edge dislocation on the basal plane dissociates into two partials with a stacking fault in between. Peierls stress was found to be 2.12 MPa, 25 MPa, and 26 MPa for basal, prismatic, and pyramidal respectively. Atoms are colored according to common neighbor analysis (CNA) where red atoms are HCP atoms, green are FCC atoms, blue are BCC atoms and white are other atoms.

Figure 8 shows the evolution of velocity as a function of applied stress for different temperatures. As seen from figure 8, velocity is linear up to an 80 MPa load for the basal and prismatic edge dislocations as compared to up to 60 MPa for the pyramidal edge dislocation. There are three regions, the first region where velocity linearly increases with the applied load, the second region where there is curvature or non-linearity as shown in figure 8, and the third region where velocity saturates out and corresponds to maximum velocity in the material (forbidden velocity). We found the forbidden velocity to be 1800 m/s, 2200 m/s, and 800 m/s for the basal, prismatic, and pyramidal dislocation, respectively. Transverse sound waves travel at the speed of 3100 m/s in titanium. The linear part (first region) of the figure was fitted using the least squares procedure with

$$v = \alpha\left(\frac{b\sigma}{T}\right) \tag{12}$$

where v is the velocity, α is a material constant, b is the burger's vector, σ is the applied load, and T is the temperature. The drag coefficient was found to be in the range of 9.94E-6 Pa.s to 7.12E-5 Pa.s. The drag coefficient for the basal and prismatic edge dislocation was very similar at all temperature; whereas, the drag coefficient for the pyramidal plane was higher by a factor of 10. This can be attributed to more screw components in the edge pyramidal plane as compared to the basal and prismatic planes. We can conclude from these results that dislocation is more mobile on the prismatic and basal planes as compared to the pyramidal plane.

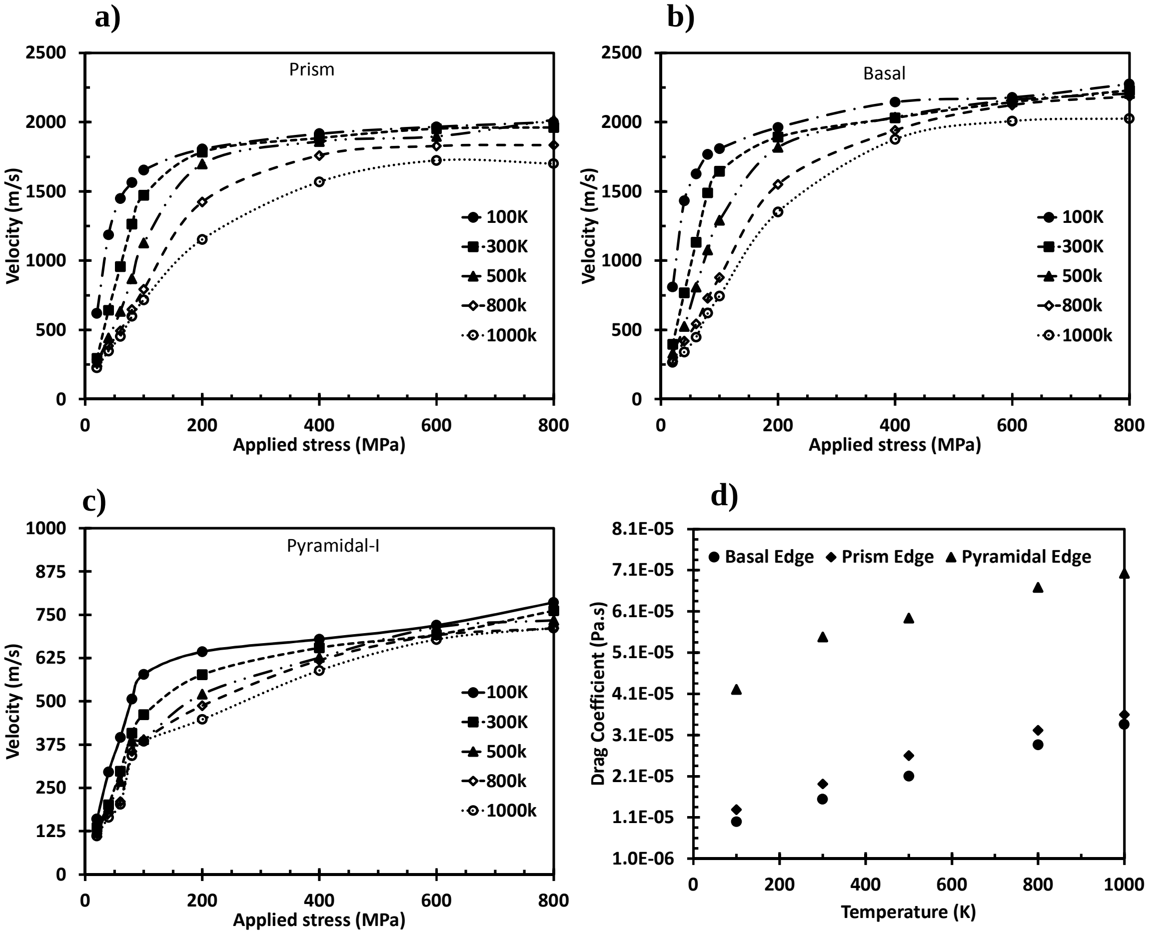

Figure 8: Velocity as a function of applied load for <a> type edge dislocation on the a) prismatic plane b), basal plane, and c) pyramidal plane and d) drag coefficient as a function of temperature on basal, prismatic, and pyramidal planes. The edge dislocation velocity on the basal and prismatic planes is more than on the pyramidal plane.

4.4 SCREW DISLOCATION: STATIC AND DYNAMIC

Figure 9 shows the differential displacement for <a> type screw dislocation in titanium with the EAM potential (Figure 9a), FS potential, (Figure 9b) and SW spline MEAM potential (Figure 9c) for two different origins of the anisotropic displacement field, i.e., dislocation center 1 (DC1) and dislocation center 2 (DC2). In the case of DC1, the EAM potential predicts a planar dislocation core which resolved along the basal plane. The FS potential predicts a planar dislocation core along the prismatic plane. The MEAM potential, a non-planar dislocation core with partially resolved along the prismatic, pyramidal, and basal planes. For the case of DC2, all the three potentials predict the planar dislocation core spreading on the prismatic plane which is in good agreement with earlier work of Rao et al. (Rao, Venkateswaran, and Letherwood 2013). To further evaluate the critical stress required for a screw dislocation to move, we applied a shear strain of 10^{-4} along the burger's vector direction (z-direction) on the prismatic plane for the DC2 dislocation core configuration. The critical stress was found to be 5.2 MPa and 10 MPa for the prismatic and pyramidal plane loading with EAM potential; whereas, stress was 224 MPa and 340 MPa for the prismatic and pyramidal plane loading using the MEAM potential, respectively. Results with the MEAM potential are higher because of the angular term included in fitting the potential. Moreover, this potential has 3rd and 4th nearest neighbors as a cutoff parameter which makes the material stiffer and has been reported by Rao (Rao, Venkateswaran, and Letherwood 2013). Moreover, to see the orientation effect, loading was applied with $-45^\circ < \theta < 45^\circ$ where $\theta=0^\circ$ is the prismatic plane. Figure 10 shows the critical stress with different orientations and it follows the Schmidt law. Hence, results suggest very little orientation effect on the peirels stress of an <a> type screw dislocation. This behavior is due to little non-planarity of the dislocation core (Figure 9) which agrees with the experiment where an hcp crystal follows the Schmidt law.

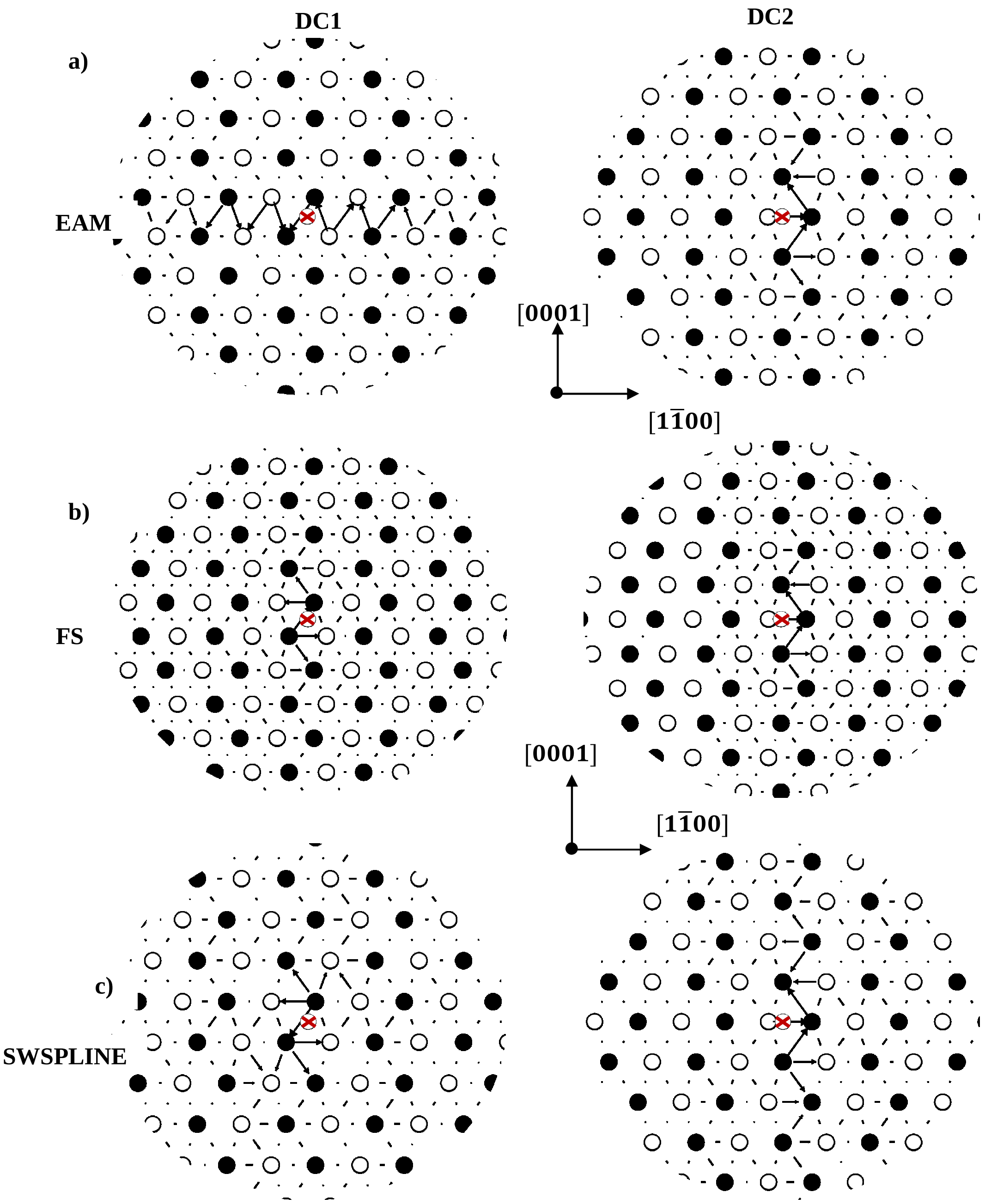

Figure 9: Differential displacement plot for screw dislocation core structure with different interatomic potentials a) EAM b), FS and c) SW-spline MEAM at two different dislocation center points as shown with a cross in figure. The screw dislocation with the EAM potential dissociates on the basal plane for DC1; whereas, FS and SW-spline dissociate on the prismatic, pyramidal, and basal planes. The Core structure with DC2 compares well with previous works (Rao, Venkateswaran, and Letherwood 2013) (Ghazisaeidi and Trinkle 2012). Note: the filled circles represent atoms at z=0 and open circles at z=$\vec{b}/2$. DCi is the center of the dislocation marked with cross.

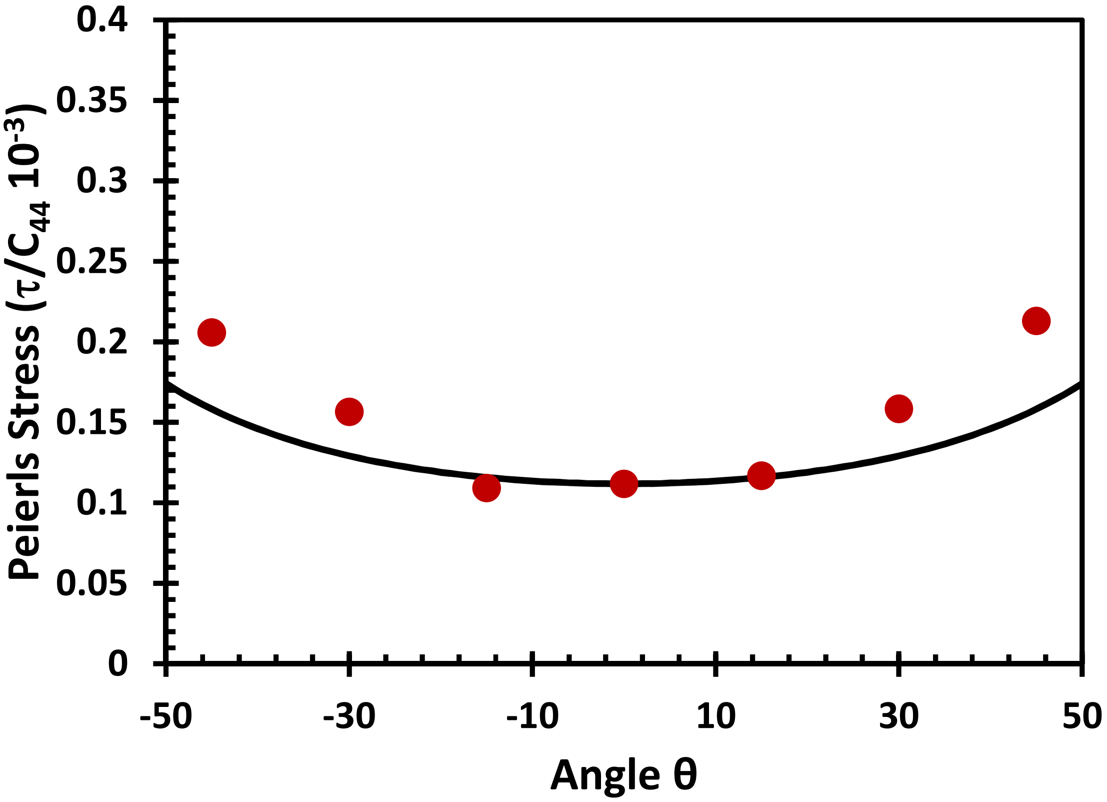

Figure 10: Peierls stress as a function of misorientation from prismatic plane. Small deviation from the expected Schmidt behavior was due to the presence of small edge character in the dislocation core structure and the non-planar core structure.

Figure 11 shows the dislocation core energy for the screw dislocation as a function of ln(R/r_0) for two dislocation centers (i.e., DC1 and DC2). The dislocation core energies with DC1 center were found to be -0.005 eV/□, 0.12 eV/□, and -0.15 eV/□ using the EAM, FS, and the MEAM potentials, respectively. Similarly, with the DC2 centers, the dislocation core energies were found to be 0.15 eV/□, 0.11 eV/□, -0.19 eV/□ using the EAM, FS, and the MEAM potentials, respectively. Based on these results, it can be concluded that there is a high probability for a DC2 core to transform into a DC1 core using the EAM potential. The preferred screw dislocation core for the EAM potential resolves along the basal (DC1); and along the prismatic (DC2) for the FS and MEAM potentials. In the next section, this phenomena has been seen when a screw dislocation core with a DC2 origin is sheared at temperature. These results are comparable with the work of Girshick et al. (Girshick, Pettifor, and Vitek 1998) where they have shown the spreading of a dislocation core on the prismatic plane to be the preferred plane with the Bond Order Potential.

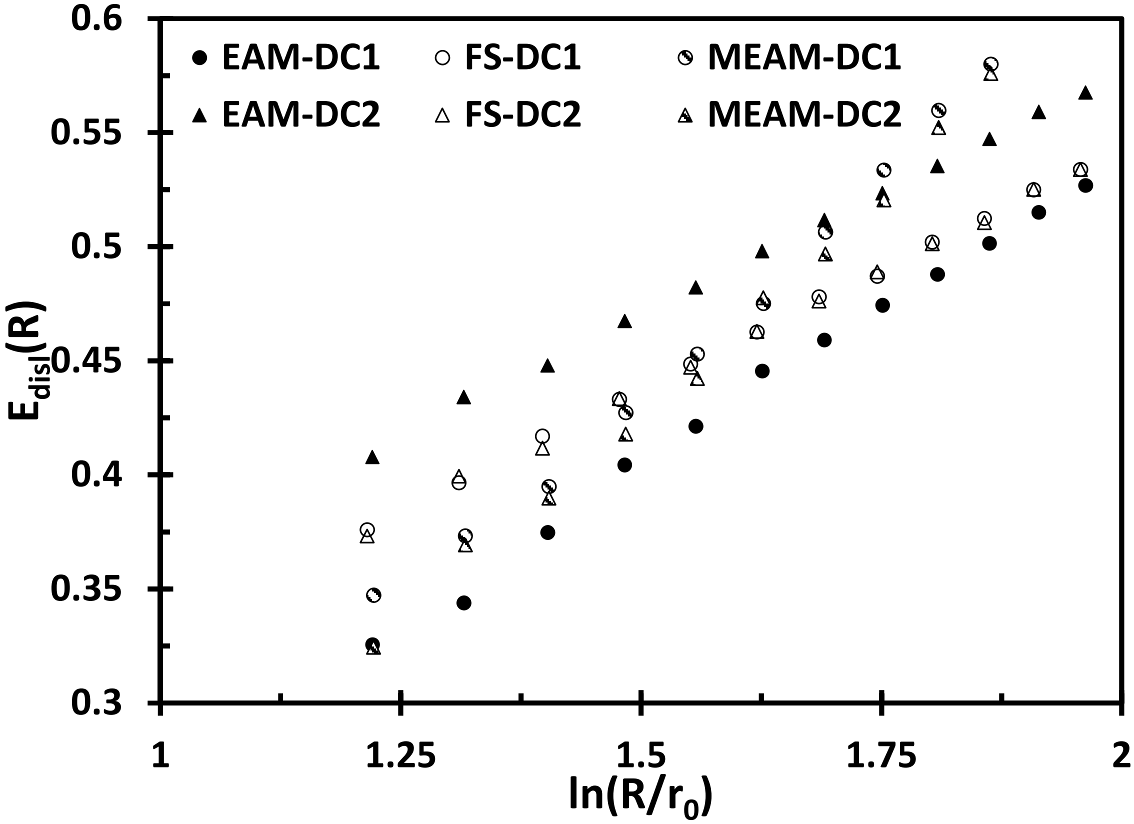

Figure 11: Energy of a screw dislocation stored within a cylinder of radius R as a function of ln(R/r) for origin DC1 and DC2. Filled points are EAM results; open points are FS calculation; and half-filled points are MEAM results.

Figure 12 shows the evolution of velocity for <a> type screw dislocation on various slip planes as a function of the applied stress with different temperatures. As seen from Figure 12, velocity increases linearly up to an applied load of 80 MPa for the <a> type basal, and prismatic screw dislocations. The velocity for a screw dislocation on the pyramidal plane increases with the applied load and does not saturate to a constant value. Moreover, at room and higher temperatures, enough thermal energy is available to change the initial structure of the DC2 (prismatic spread) dislocation core into DC1 (basal spread) dislocation core due to lower dislocation core energy for DC1 (-0.005 eV/ □) as compared to the DC2 (0.15 eV/ □) (Figure 11). Hence, Figure 12 only reports all the dislocation core velocity where DC2 dislocation core structure is stable and doesn't migrate into a DC1 dislocation core structure. We found the maximum velocity to be 550 m/s and 600 m/s for the prismatic and basal dislocations, respectively. Again the linear part (first region) of the figure was fitted using a least squares procedure to quantify the drag coefficient for the screw dislocation. Drag coefficient was found to be in the range of 2.9E-5 Pa.s to 6.35E-5 Pa.s. The drag coefficient for the basal and prismatic edge dislocation was very similar at 100 K temperature; whereas, the drag coefficient for the pyramidal plane was higher by a factor of 2 compared to other slip planes. Therefore, we can conclude that the screw dislocation mobility was highest on the prismatic plane followed by the basal and pyramidal planes respectively. Moreover, the edge dislocation mobility was found to be greater when compared to the screw dislocation as shown in Figures 8 and 12.

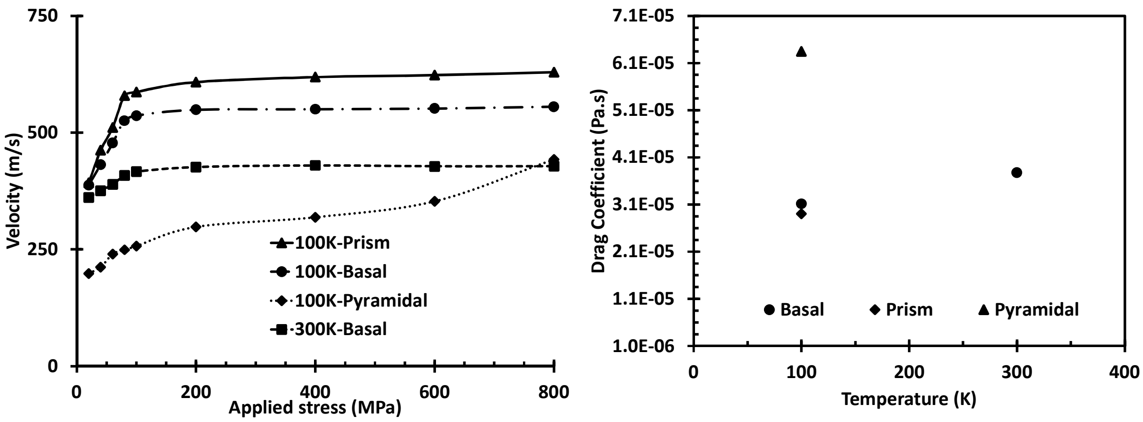

Figure 12: a) The dislocation velocity as a function of the applied load for <a> type screw dislocation on the basal, prismatic, and pyramidal planes and b) the drag coefficient as a function of temperature on the basal, prismatic, and pyramidal planes. Note: the screw dislocation dissociates into the DC2 structure on the basal plane above 500K for the basal plane and above 300K for prismatic and pyramidal planes.

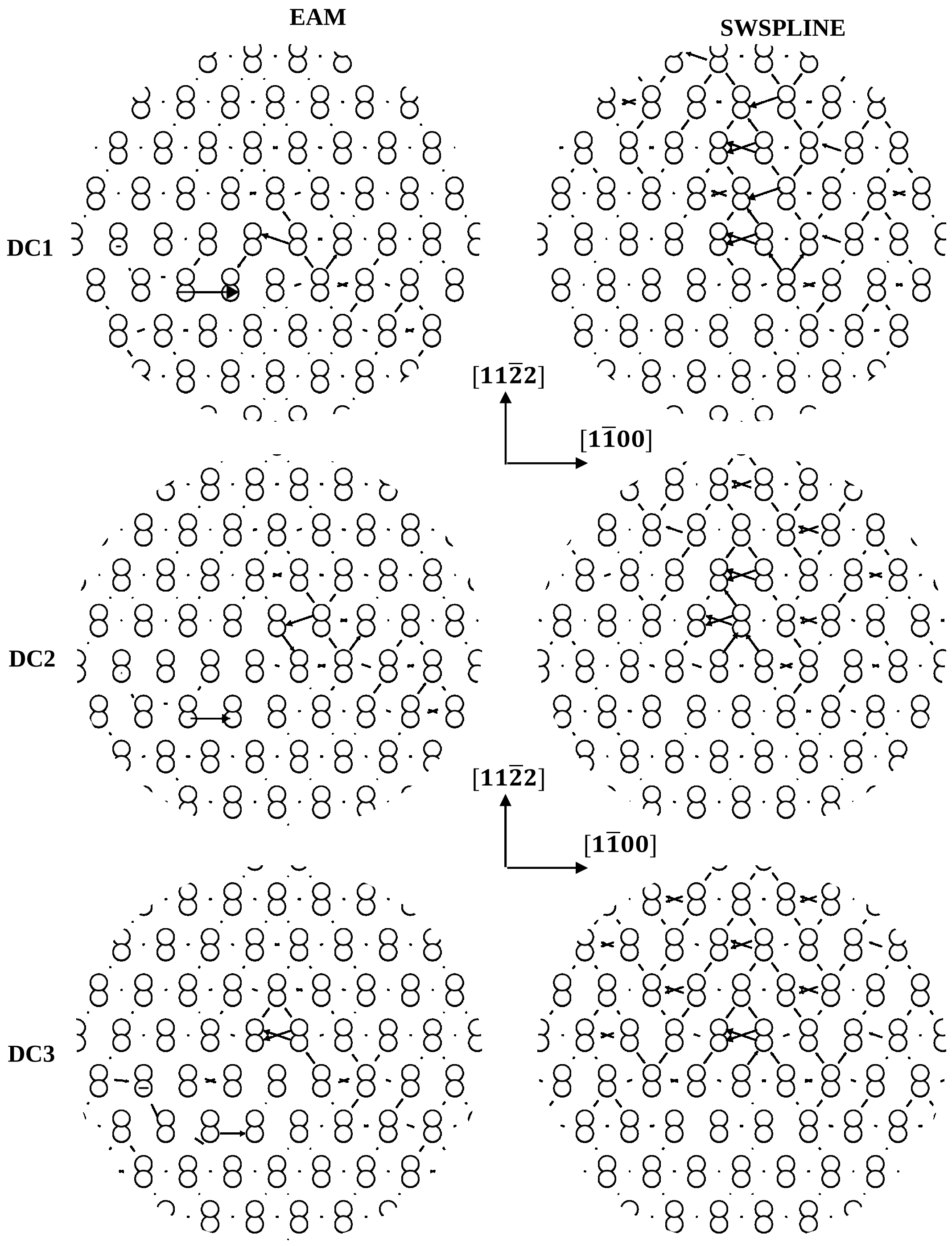

Figure 13: Differential displacement plot for <c+a> type screw dislocation core structure with a) Yuri Mishin EAM potential and b) Hening swspline MEAM potential at three dislocation center points. Note that the screw dislocation with EAM potential shows spreading on the first order pyramidal plane $\{10\bar{1}1\}$, whereas SWSPLINE dissociates on the first order $\{10\bar{1}1\}$ and second order pyramidal planes $\{11\bar{2}2\}$.

4.4 SUMMARY

In summary, based on the dislocation core energy, the EAM and FS potentials prefer the minimum core energy of an edge dislocation on the basal plane; whereas, the MEAM potential predicts the prismatic plane (Figure 6). Furthermore, for an <a> type screw dislocation, the MEAM potential predicts the dislocation core to resolve on the prismatic plane (DC2) with small non planar components on the pyramidal and basal planes (Figure 11). In case of the EAM potential, the dislocation core was resolved on the basal plane (DC1), since the DC2 shows a small non planar character and very little orientation effect, i.e., follows the Schmidt law. Whereas, the DC1 core structure for the MEAM potential was resolved along all the three slip planes, so it will have a non-Schmidt component playing a role in the dislocation motion which will be a good study for the future. For the dynamic part, the motion of an edge dislocation is higher than that of a screw dislocation which is in agreement with experiments. At room temperature and higher temperatures with the EAM potential, the <a> type screw dislocation core with the DC2 structure (Figure 9a) rearranges to the DC1 (Figure 9b) dislocation core structure during minimization due to the availability of excess thermal energy. The drag coefficients for edge and screw dislocations have been reported, and these findings can be utilized for the development of higher length scale models.

CHAPTER 5

5 EFFECT OF OXYGEN ON THE DISLOCATION CORE: A QUANTUM MECHANICS / MOLECULAR MECHANICS (QM/MM) APPROACH

5.1 INTRODUCTION

Titanium (Ti) and its alloys have been traditionally used for structural applications in automotive, aerospace, and biomedical applications due to their high strength-to-weight ratios (Leyens and Peters 2003). Commercially pure (CP) Ti-alloys, in particular, are attractive materials due to their excellent corrosion resistance, light weight, and formability. However, the strength and toughness of these alloys are affected by relatively small variations in their impurity contents, such as oxygen (O). Specifically, it has been shown that an increase in impurity contents can cause a material to either harden or soften by interacting with dislocations or twins (Brandes et al. 2012; Dong and Li 2000; Liu and Welsch 1988). In high strength grade Ti-alloys, the addition of oxygen improves the corrosion and wear resistance of α-Ti and its alloys (Stringer 1960; Leyens and Peters 2003). However, at elevated temperatures, the oxide layer at the Ti surface will grow and oxygen will rapidly diffuse into the base metal (Liu and Welsch 1988), instigating hardening of the α-Ti (Dong and Li 2000). Notably, with higher percentages of impurity contents (e.g., oxygen), a transition from wavy (dominant cross slip nature) to planar dislocation slip has been reported (Williams, Sommer, and Tung 1972) along with an increase in <c+a> dislocation activities (Brandes et al. 2012). Consequently, understanding the mechanisms behind such a behavior has been of particular interest in both experimental and simulation research (H. H. Wu and Trinkle 2011; Williams, Sommer, and Tung 1972; Brandes et al. 2012). In fact, the indeterminate mechanistic nature of such a behavior hinders our ability to satisfactorily address the role of oxygen in important technological applications, including nuclear power plants and other large-scale, industrial infrastructure (e.g., wind turbines).

5.2 METHODOLOGY

In this chapter, to elucidate the complex nature of interactions between prismatic faults and an oxygen solute and to shed light on experimental results, we employed a coupled quantum and molecular mechanics (QM/MM) framework along with a climb-based nudge elastic band (C-NEB) method of Henkelman et al. (Henkelman, Uberuaga, and Jónsson 2000) and the semi-discrete variational based generalized Peierls-Nabarro model (SVPN) (Bulatov and Kaxiras 1997a). First, we systematically assessed the energetically favorable site near the prismatic dislocation ($\{10\bar{1}0\}\langle 1\bar{2}10\rangle$) and used the new found stable site to assess the oxygen diffusional barrier (high or low). Quantifying the diffusional barrier is instrumental to understanding the observed oxygen strengthening effects in α-Ti. In addition, the stable site and dislocation core structure can be used to study oxygen effects on the softening or hardening behavior, i.e., effect on the dislocation glide stress (Peierls stress). However, calculation of the change in the dislocation glide stress due to oxygen using explicit modeling of the dislocation core requires extra care because of periodic boundary conditions and the need to model sufficiently large dislocation line lengths to minimize periodic solute effects (also computationally expensive). Thus, in this work, the generalized stacking fault energy

(GSFE) and the SVPN formulation were used to provide non-empirical predictions of oxygen effects on the softening or hardening behavior. The GSFE curves are often employed as an alternate method to measure and understand dislocation core properties. Further, we also calculated the charge density to qualitatively understand charge transfer in the presence of an oxygen atom. The interaction between a prismatic fault and an oxygen solute atom is particularly important as it has a significant impact on the dislocation-based mechanical properties of α-Ti (see (Song, Guo, and Yang 2002)).

In the QM/MM approach, the entire system is partitioned into three spatial domains: I) core (QM-DFT), II) transition (DFT for the energy and EAM for the force balance), and III) elastic (MM-EAM). The QM region treated by the constrained DFT (Q. Zhao and Parr 1993; Q. Zhao, Morrison, and Parr 1994) within the Vienna Ab-initio Simulation Package plane wave electronic structure code (DFT-VASP) (Georg Kresse and Hafner 1993) and an MM region is treated by empirical atomistic simulations (Daw and Baskes 1983) (see Zhang and Lu (Zhang, Lu, and Curtin 2013),(Zhang and Lu 2007) and also supplemental section for the QM/MM methodology). The semi-empirical embedded atom potential (EAM) developed by Zope and Mishin (Zope and Mishin 2003) was used to model the defect free EAM region in the QM/MM (see the Supplemental section). Table 5 lists the lattice properties of Ti with EAM potential and its comparison with DFT data. The EAM potential was modified to match the lattice constant of DFT for QM/MM study to minimize the misfit energy at the boundary of coupling.

Table 5: Comparison of lattice constants and bulk modulus of the Ti EAM Potential with the DFT value.

	a (Å)	□=c/a	K (GPa)	SF (J/m^2)
DFT	2.94	1.58	109.62	0.268
EAM	2.951	1.588	113.47	0.237

An edge dislocation was created, as described by Osetsky and Bacon (Osetsky and Bacon 2003), initially in LAMMPS (Plimpton 1995). The edge dislocation structure obtained using the EAM potential was further relaxed using QM/MM with a conjugate gradient algorithm with 30 meV/Å force and 1 meV energy convergence criteria. The QM region had 196 atoms containing the dislocation core with/without an oxygen impurity and the MM region consisted of the remainder of the system (11926 atoms) including the long-range elastic field of the dislocation. The overall dimensions of different regions were: 30 Å x 27 Å x 9.26 Å for the QM region and 143.67 Å x 155.07 Å x 9.26 Å for the MM region which is large enough to have no effect by simulation cell size. The simulations were performed on a rectangular cell having x, y, and z-axes oriented along the $[1\bar{2}10]$, $[10\bar{1}0]$, and $[0001]$ directions, respectively. The length along the dislocation line [0001] was set to $2c$ (c = 4.645 Å) to avoid interaction of oxygen atoms due to periodic boundary conditions. For the pipe diffusion of an oxygen atom along the dislocation line, the energy required by an oxygen atom to overcome the barrier was studied using the QM/MM with a C-NEB with sixteen intermediate images between the global minimums.

For the DFT part, projector augmented wave (PAW) (Peter E. Blöchl 1994) potentials were used to represent the nuclei core with valence electrons on *s* and *d* orbitals for α-Ti and valence electrons on *s* and *p* orbitals for oxygen atoms. Exchange and correlation was treated with GGA using the PBE (Perdew, Burke, and Ernzerhof 1997) form with an energy cutoff of 289 eV and the Monkhorst Pack k-point mesh of 1 x 1 x 5 along the $[1\bar{2}10]$, $[10\bar{1}0]$, and [0001], respectively. For GSFE calculations, the k-point mesh is 18 x 1 x 10. The ionic relaxation was carried out using a conjugate gradient algorithm with 30 meV/Å force and 1 meV energy convergence criteria. A single oxygen atom was introduced on the prismatic shearing plane (along with six Ti atoms), i.e., a monolayer (ML) oxygen concentration of 16.67% and the model was subsequently sheared along the $[1\bar{2}10]$ direction. It should be noted here that the oxygen atom was free to relax in all directions during the minimization whereas Ti atoms were free to move along the *y*-direction ($[10\bar{1}0]$).

5.3 OXYGEN DIFFUSION IN BULK TITANIUM

First, we present oxygen diffusing in bulk α-Ti. In α-Ti there are three positions for an interstitial atom to occupy, i.e., octahedral, crowdion, and hexahedral. An interstitial oxygen atom prefers the octahedral site in bulk α-Ti (H. H. Wu and Trinkle 2011). The hexahedral is a position on the basal plane; whereas, the octahedral and crowdion are in-between A and B stackings along the [0001] direction (H. H. Wu and Trinkle 2011). The transition pathways and energy barriers between different interstitial sites for an oxygen atom in bulk α-Ti were investigated using the C-NEB method with 4 intermediate images to find the transition pathways and barriers between different interstitial sites. Figure 14 shows the energy barrier for an oxygen atom to diffuse from an octahedral position to a crowdion position (O-C) then from a crowdion position to a hexahedral position (C-H) and finally from a hexahedral position to an octahedral position (H-O). Also, the migration pathway is illustrated by showing the oxygen position along the transition path in Figure 14. The potential energy of the hexahedral position is 1.43 eV higher than that of the octahedral position. Moreover, the excess energy of the crowdion position over the octahedral position is 1.95 eV. Both these positions (crowdion and hexahedral) are local minima along the migration pathway and thus require excess thermal energy for the oxygen atom to reach the energetically favorable octahedral positions. The crossover energy barriers for crowdion and hexahedral positions to the octahedral positions are 120 meV and ~550 meV, respectively, which compares well with the work of Wu and Trinkle (H. H. Wu and Trinkle 2011).

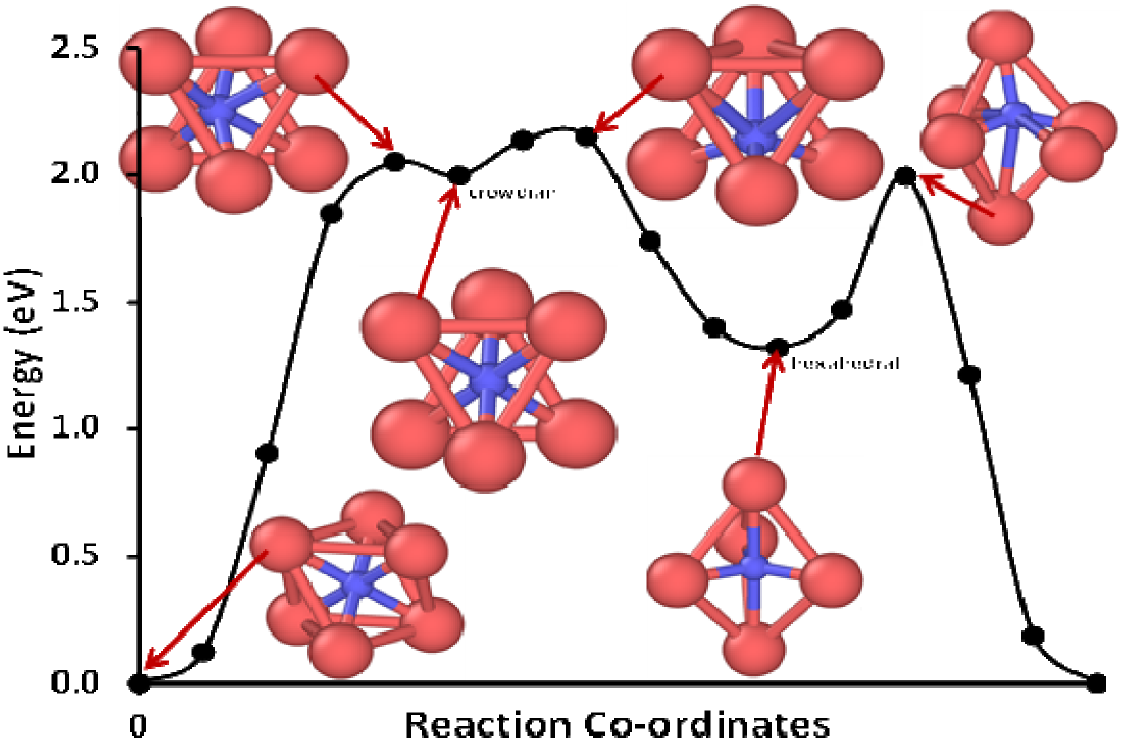

Figure 14: C-NEB path for an oxygen diffusing in bulk α-Ti with the energy barrier for an oxygen atom to diffuse between different interstitial sites.

5.4 OXYGEN DIFFUSION AT EDGE DISLOCATION CORE

Next, our main objective was to understand the atomistic mechanisms of oxygen-dislocation interaction in α-Ti. To achieve this, the relative site preference of oxygen at the prismatic edge dislocation is addressed. The total energy of a single oxygen atom situated near the dislocation core region (various interstitial sites) and further away from the core as far as possible within the supercell size has been calculated. Figure 15a shows the optimized equilibrium geometry of oxygen at the prismatic edge dislocation in α-Ti when viewed along the [0001] direction. The local geometry changes from an HCP octahedral to a BCC octahedral site. The oxygen atom binds with four Ti atoms on the same basal plane and with another two Ti atoms above and below it. This position is the same as the hexahedral position in bulk α-Ti, except that now there are four atoms on the basal plane (see Figure 15b) instead of three (Figure 14) due to the dislocation core.

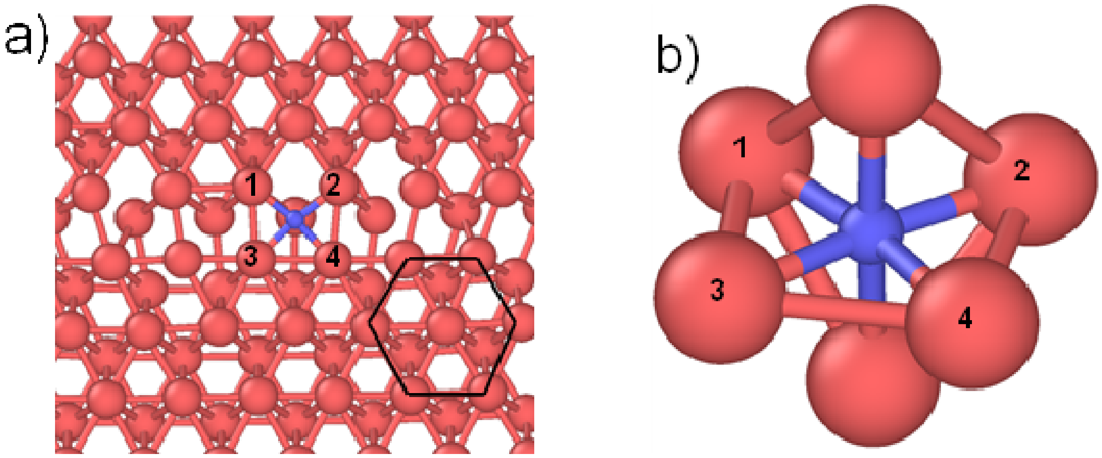

Figure 15: a) Oxygen binding at the prismatic dislocation core with the plane of sight along the [0001] direction. b) Oxygen binds with six α-Ti atoms at the dislocation core. Atoms are marked by number on the basal plane.

Having obtained the stable oxygen site at the dislocation core, the transition pathways and energy barriers between different interstitial sites for an oxygen atom at the dislocation core (diffusion along a dislocation line) was explored using the C-NEB method with 16 intermediate images. Figure 16a shows the initial path for an oxygen atom to diffuse over a distance of c (4.645 Å) along the dislocation line (i.e., along the $[0001]$ direction with ABAB stacking). The energy barrier and transition path for the pipe diffusion of oxygen along the dislocation line are depicted in Figure 16b. Also, the migration pathway is illustrated by showing the oxygen position along the path in Figure 16a. The energy barrier for the diffusion path from one BCC octahedral position to another BCC octahedral position is 1.24 eV along the edge dislocation line, which is much smaller than the bulk diffusion barrier of ~2.0 eV. The probability of an oxygen atom penetrating from one octahedral position to another octahedral position in bulk at room temperature is very small, since the potential barrier is high: 2.0 eV. However, the probability increases with the increase in system temperature as given by the probability $\Gamma = 10^{13} \exp(-E_b/k_B T)$ where the phonon frequency is typically considered to be 10^{13}/sec (Penetration barrier E_b, Boltzmann Constant k_B, and absolute temperature is T). Considering the present case where E_b is 2 eV, for a unit probability, the temperature turns out to be 775 K. In the case of one oxygen atom penetrating along the edge dislocation from one octahedral position to another octahedral position and for a unity probability, the temperature turns out to be 496 K.

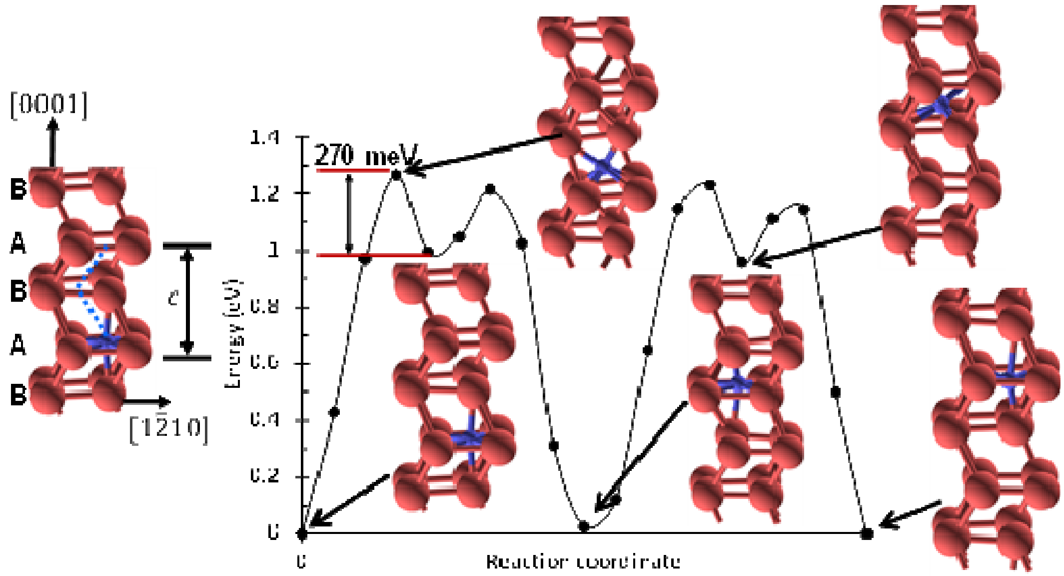

Figure 16: a) Diffusion path of an oxygen atom along the dislocation line ([0001] direction) of the prismatic edge dislocation with ABAB stacking sequence. b) The C-NEB path for oxygen diffusing along the dislocation line (pipe diffusion) in a prismatic edge dislocation.

5.5 GENERALIZED STACKING FAULT ENERGY

With high diffusion barrier, we now explore the effect of oxygen on the softening or hardening behavior and establish non-empirical parameters through GSFE calculations along with the SVPN model, since the modeling of dislocation mobility in DFT is relatively expensive. Figure 16a illustrates GSFE curves as a function of shear displacement along the [1$\bar{2}$10] direction for α-Ti with and without oxygen (1/6 ML). The unstable stacking fault energy for pure Ti is increased from 237 mJ/m^2 to 303 mJ/m^2 (27.85% increases) with addition of 1/6 ML oxygen on the shear plane. Since oxygen increases the unstable stacking fault energy, we employed an SVPN framework (see details in (Bulatov and Kaxiras 1997b)) to quantify the role of oxygen on plastic deformation in α-Ti. The core width and the Peierls stress were calculated using the

SVPM method with DFT data as shown in Figure 16a for the cases with and without oxygen on the shear plane. The Peierls stress for prismatic slip in Ti with and without 1/6 ML oxygen was found to be 96.6 MPa and 24 MPa, respectively (~400% increase with addition of oxygen). The simulations also revealed that the prismatic dislocations were small in core width with the addition of oxygen, i.e., the core width with 1/6 ML oxygen on the shear plane is 0.9 Å as compared to 1.1 Å for pure Ti.

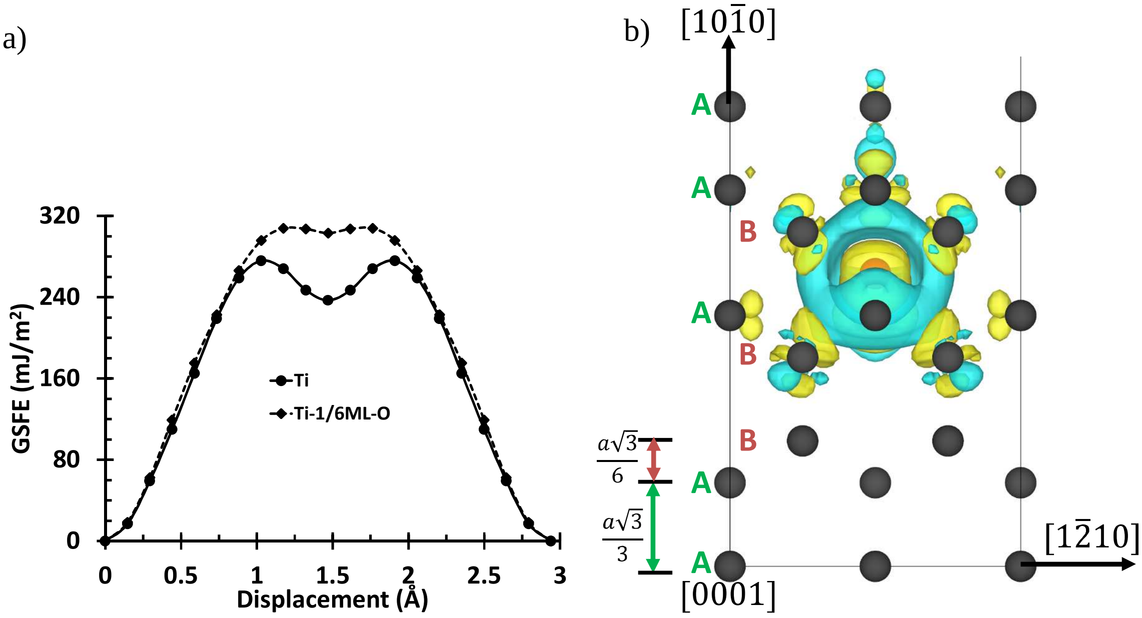

Figure 17: a) GSFE as a function of shear displacement along the [1$\bar{2}$10] direction of α-Ti with and without 1/6 ML oxygen on the slip plane. b) A 3D iso-surface plot for charge density showing the effect of O at the prismatic stacking fault. The orange and black atoms represent oxygen and Ti atoms, respectively. The yellow and cyan iso-surfaces represent charge accumulation and depletion, respectively.

5.6 CHARGE DENSITY WITH OXYGEN

The mechanical properties of a material are defined by the nature of the atomic bonding. Bonding between atoms is the result of the polarization of charge densities around the nuclei. Both the shear strength and cohesive strength are affected by bond directionality and also by charge distribution around atoms. Therefore, understanding the change in charge density with a solute is necessary for evaluating the shear strength of a material and the subsequent effect on the plastic deformation behavior (see (Song, Guo, and Yang 2002)). Figure 17b presents a 3D iso-surface plot for charge density (differential) showing the effect of oxygen at the prismatic stacking fault. The yellow and cyan iso-surfaces represent charge accumulation and depletion, respectively. In comparison with the charge density distribution of pure α-Ti, the main change for oxygen at the prismatic stacking fault seems to be around the octahedral position as seen in Figure 17b. The charge densities between Ti atoms were evidently increased with the addition of oxygen at the prismatic fault, resulting in an increase in the shear modulus, which affects the dislocation mobility as the shear stress is proportional to the shear modulus.

5.7 SUMMARY

In summary, the effect of oxygen on a prismatic edge dislocation in α-Ti was examined. According to impurity formation/binding energies calculated using the QM/MM method, it was found that oxygen prefers the BCC octahedral position at the edge dislocation. Moreover, the energy barrier for the reaction path from a BCC octahedral position to an HCP octahedral position is 1.24 eV along the edge dislocation line, which is much smaller than the bulk diffusion barrier of 2.0 eV. We also observed that oxygen can increase the Peierls energy barrier significantly, i.e., the Peierls stress for α-Ti with and without 1/6 ML oxygen was 96.6 MPa and 24 MPa, respectively. The charge densities between Ti atoms were evidently increased with the addition of oxygen at the prismatic fault, resulting in an increase in the shear modulus. The simulations also revealed that the prismatic dislocations were small in core width with the addition of oxygen. Hence, the addition of oxygen increases the stacking fault energy (and Peierls stress) and also decreases the dislocation core width on the prismatic plane which may result in an increase in <c+a> dislocation activities as seen in experiments (Zaefferer 2003). We will pursue the study of oxygen effects on the<c+a> core in future work. Generally, the observed effect of oxygen on plasticity in this study is consistent with the experimental observations, as it has been shown that an increase in oxygen content can instigate hardening of the α-Ti (Dong and Li 2000).

CHAPTER 6

6 ENERGETICS OF VACANCY SEGREGATION TO SYMMETRIC TILT GRAIN BOUNDARIES IN HCP MATERIALS

6.1 INTRODUCTION

Quantifying how point defects interact with defect sinks, such as grain boundaries, is also important for understanding strength of material interfaces in various environments, such as titanium (Ti) in a high oxygen environment, zirconium (Zr) in an irradiation environment, and magnesium (Mg) in a corrosive environment. For instance, during irradiation-induced segregation, the flux of solute and impurity elements is highly coupled with the flux of vacancies and interstitials. As vacancies and interstitials tend to diffuse and bind to microstructural sinks, solute and impurity atoms are spatially redistributed in the vicinity of these sinks (de la Rubia et al. 2000; D. Chen et al. 2013). The net result is an accumulation or a depletion of solutes at these defect sinks, which can have deleterious effects on polycrystal properties (Möslang and Wiss 2006). Hence, the objective of the present research was to understand the atomistic relationship between the local structure and the point-defect energetics at the grain boundary interface in HCP materials, such as Ti, Mg, and Zr. Molecular statics (MS) simulations of Ti, Mg, and Zr bicrystals were used for various $[1\bar{2}10]$ and $[0\bar{1}10]$ tilt grain boundaries to clarify the role of the interface character on point-defect energetics. Of particular interest was how the grain boundary character in HCP materials affects the vacancy binding energies and associated spatial variations in the vicinity of the grain boundary.

6.2 METHODOLOGY

To investigate grain boundary sink efficiency in different c/a ratio materials, we employed MS simulations using embedded atom method (EAM) potentials. Initially, a database of 190 minimum energy STGBs of Ti, Mg, and Zr with the tilt axes as $[1\bar{2}10]$ and $[0\bar{1}10]$ was generated with MS simulations, which were performed using the classical molecular dynamics code, Large-scale Atomic/Molecular Massively Parallel Simulator (LAMMPS) (Plimpton 1995). Here, the analysis cell consisted of a standard bicrystal cell with a single grain boundary that divides the HCP crystal into two single crystals, as shown in Figure 18a. The initial single crystals were created with x, y and z along the $[0\bar{1}10]$, $[0001]$ and $[1\bar{2}10]$ directions, respectively, for the $[1\bar{2}10]$ tilt axis; and along the $[1\bar{2}10]$, $[0001]$ and $[0\bar{1}10]$ directions, respectively, for the $[0\bar{1}10]$ tilt axis. Then, the upper half crystal was rotated clockwise and the lower half crystal counter-clockwise by angle θ with respect to the tilt axis, as shown in Figure 18b. Several successive rigid body translations, followed by an atom-deletion technique and energy minimization using a non-linear conjugate method (Solanki et al. 2013; Tschopp et al. 2012; Friedel 1952), were used to generate final relaxed minimum structure with the grain boundary plane along the x-z plane as shown in Figure 18c. This procedure was replicated to generate several 0 K minimum-energy grain boundary structures for Mg, Ti, and Zr. The EAM potentials of Sun et al.(Sun et al. 2006) for Mg, Zope and Mishin(Zope and Mishin 2003) for Ti, and Mendelev and Auckland (Mendelev and Ackland 2007) for Zr were used.

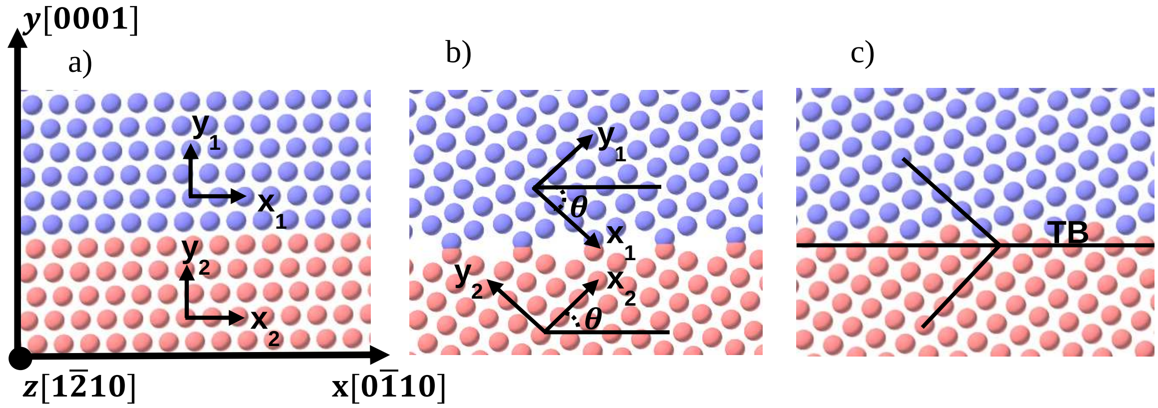

Figure 18: a) Single crystal model with x, y and z along the $[0\bar{1}10]$, $[0001]$ and $[1\bar{2}10]$, respectively, b) Upper half crystal rotated θ (~42˚) clockwise and lower half crystal rotated counter-clockwise, and c) Final grain boundary structure; rotated crystal is minimized with 1 pN force on each atom using conjugate gradient algorithm. Note: TB is the twin boundary.

Table 6: Bulk properties of Ti, Mg, and Zr.

	Lattice parameter a (Å)	**c/a ratio**	**Cohesive energy E_{coh} (eV/atom)**	**Grain boundary free volume (Å^3/atom)**	**Bulk vacancy formation energy E_f (eV)**
Ti	2.95	1.581	-4.850	17.577	1.819
Mg	3.20	1.633	-1.528	22.829	0.868
Zr	3.23	1.581	-6.013	23.072	1.385

Following the grain boundary dataset generation, the role of grain boundary character on sink efficiency for vacancies was assessed by calculating the formation energies for vacancies using MS for the generated 190 STGBs in Ti, Zr, and Mg, whereby a vacancy was placed at all sites within in a block of 3x2 nm near the grain boundary center. The database consisted of 125 $[1\bar{2}10]$ and 65 $[0\bar{1}10]$ STGBs. The vacancy formation energy for a site α is given by:

$$E_f^{\alpha} = E_{Gb}^{\alpha} - E_{Gb} + E_{coh}, \tag{13}$$

where E_{coh} is the cohesive energy/atom of a perfect HCP lattice (see Table 6), and E_{Gb}^{α} and E_{Gb} are the total energies of the grain boundary simulation cell with and without the vacancy, respectively. The cohesive energy for one atom is added to account for the extra atom in the case of the grain boundary simulation cell without the vacancy.

6.3 GRAIN BOUNDARY ENERGY AND ATOMIC FREE VOLUME

Understanding the structure and energy of the grain boundary system is crucial for engineering materials intended for advanced applications because grain boundary properties can vary widely (coherent twin versus low angle versus high angle grain boundaries). In this study, a range of grain boundary structures and energies that are representative of some of the variations observed in the grain boundary character distribution of polycrystalline as well as nanocrystalline metals was used to investigate the role of grain boundary character on point-defect energetics such as the vacancy binding energy in different c/a ratio materials. Figure 19 shows grain boundary energies as a function of the misorientation angle for the $[1\bar{2}10]$ and $[0\bar{1}10]$ tilt axes in Mg, Ti, and Zr. The trend observed for the grain boundary energy as a function of a misorientation angle is comparable to what has been previously reported in the literature for the Mg, and Ti (Jian Wang and Beyerlein 2012a; Jian Wang and Beyerlein 2012b). The energy cusps for the $[1\bar{2}10]$ system were identified as $(\bar{1}013)\theta = 32.15°$, $(\bar{1}012)\theta = 43.31°$, $(\bar{1}011)\theta = 62.06°$ and $(\bar{2}021)\theta = 75.21°$ twin boundaries for magnesium, in order of increasing misorientation angle. Similarly, in the case of the $[0\bar{1}10]$ tilt axis, the energy cusps were $(\bar{2}116)$, $(\bar{2}114)$, $(\bar{2}112)$, and $(\bar{2}111)$ twin boundaries.

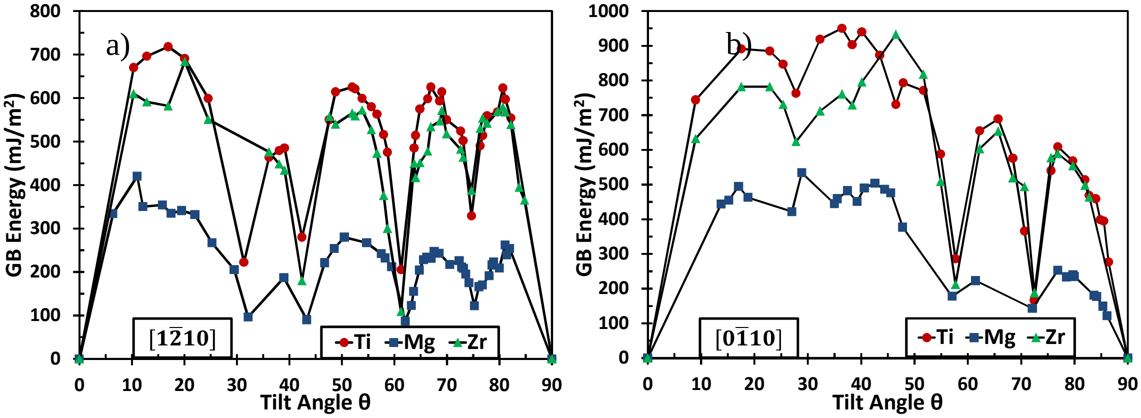

Figure 19: The plot of grain boundary energy as a function of grain boundary misorientation angle for a) the $[1\bar{2}10]$ tilt axis, and b) the $[0\bar{1}10]$ tilt axis in Ti, Mg, and Zr. Note that the energy cusps for the $[1\bar{2}10]$ system were identified as $(\bar{1}013)$, $(\bar{1}012)$, $(\bar{1}011)$ and $(\bar{2}021)$ twin boundaries, in order of increasing misorientation angle. Similarly, in the case of the $[0\bar{1}10]$ tilt axis, the energy cusps were $(\bar{2}116)$, $(\bar{2}114)$, $(\bar{2}112)$, and $(\bar{2}111)$ twin boundaries.

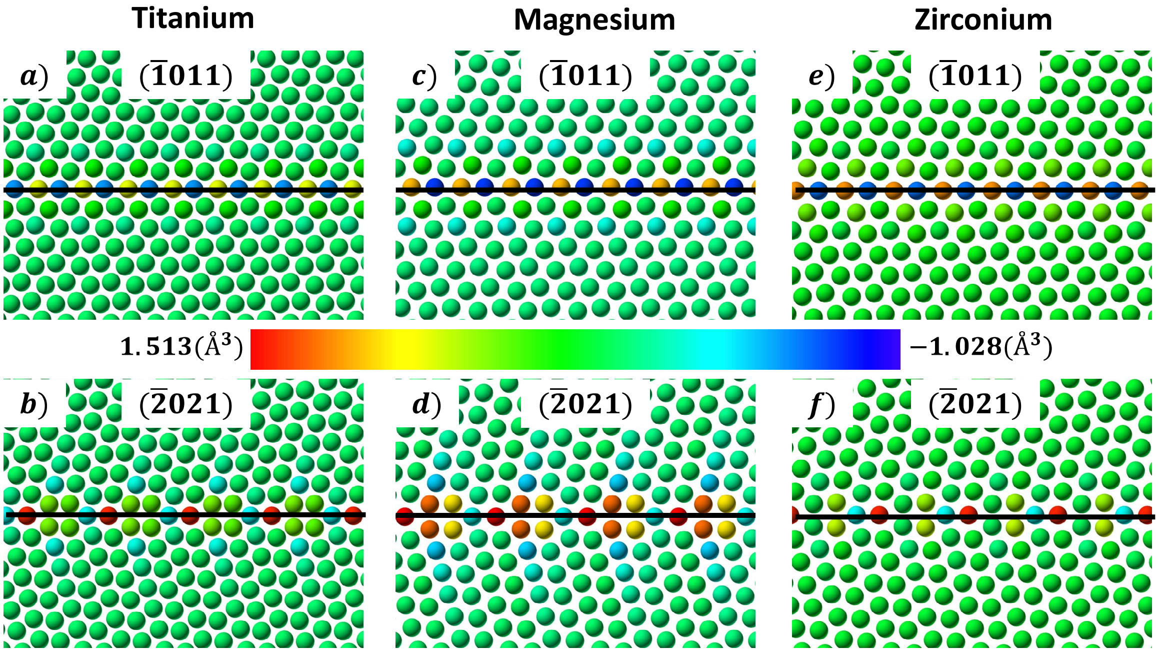

Figure 20: Atomic representation of $(\bar{1}011)$ and $(\bar{2}021)$ grain boundaries depicting the distribution of the excess Voronoi volume in Ti (a and b), Mg (c and d), and Zr (e and f) for the $[1\bar{2}10]$ tilt axis. The bulk Voronoi volume was found to be 17.57, 22.82 and 23.07 Å^3 for the Ti, Mg and Zr, respectively. The black line indicates the twin boundary plane.

The structure-energy correlation can provide more details about the variation in grain boundary energies, as each grain boundary has characteristic SUs describing its atomistic morphology. Low-angle boundaries can be represented by an array of discrete dislocations. However, at higher misorientation angles (high-angle grain boundaries), the dislocation cores overlap, and dislocations rearrange to minimize the boundary energy. The resulting grain boundary structures are often characterized by grain boundary dislocations or SUs(Jian Wang and Beyerlein 2012a; Jian Wang and Beyerlein 2012b; Sutton and Vitek 1983). Figure 20 shows the spatial distribution of atomic excess volume for $(\bar{1}011)$ and $(\bar{2}021)$ grain boundaries with the $[1\bar{2}10]$ tilt axis in Ti, Mg and Zr. Similarly, Figure 21 shows the spatial distribution of excess atomic volume for $(\bar{2}112)$

and $(\bar{2}116)$ grain boundaries with the $[0\bar{1}10]$ tilt axis in Ti, Mg and Zr. Notice that the atoms far away from the boundary are green (0 Å^3 excess Voronoi volume), indicating that there is no atomic volume difference over the bulk lattice. The bulk Voronoi volume was found to be 17.57, 22.82 and 23.07 Å^3 for the Ti, Mg and Zr, respectively. The excess Voronoi volume is highest/lowest (tensile versus compressive) at the grain boundary center and converges to the bulk Voronoi volume as distance from the grain boundary increases. Interestingly, the $(\bar{1}011)$ and $(\bar{2}112)$ plane twin boundaries in Mg and Zr have higher/lower (tensile versus compressive) excess Voronoi volumes than the Ti twin boundary, potentially due to the larger interplanar spacing. That is, near the twin boundary, the interplanar spacing changes and can increase or decrease associated atomic volume due to twinning dislocations (shuffling of atoms)(Serra, Pond, and Bacon 1991; J. Wang, Beyerlein, and Hirth 2012). In the case of $(\bar{2}021)$ and $(\bar{2}116)$ plane grain boundaries, Mg has higher/lower (tensile versus compressive) excess Voronoi volumes than the Ti and Zr. This grain-boundary metric can in turn be correlated to other energetics associated with the grain boundaries to derive a structure-property relationship.

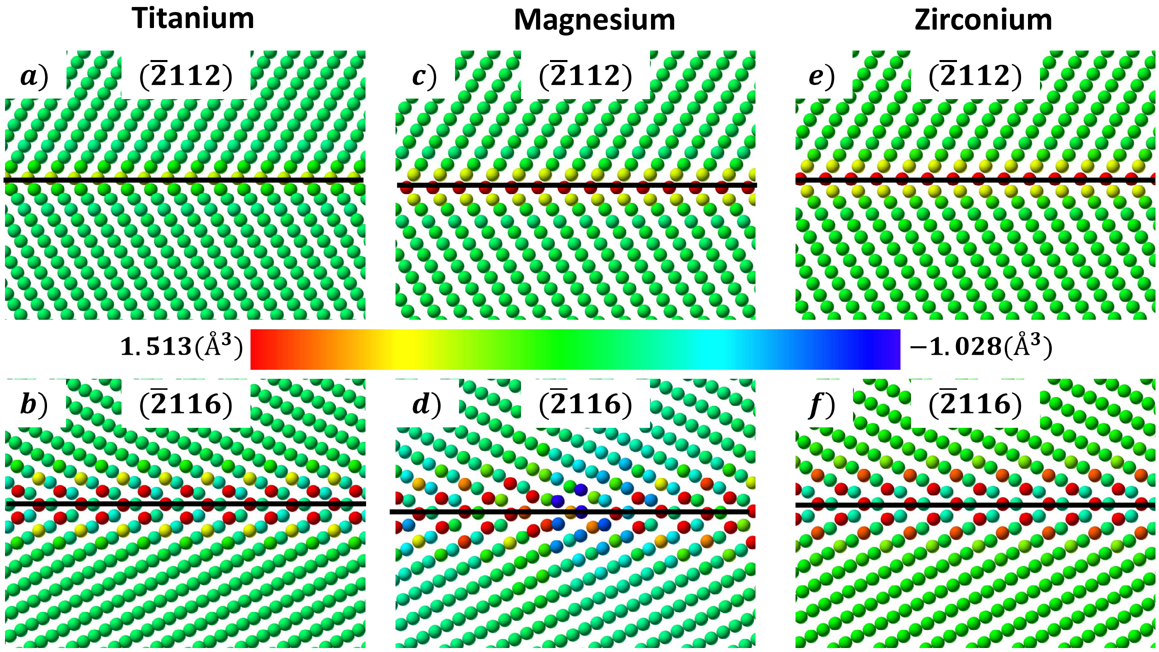

Figure 21: Atomic representation of $(\bar{2}112)$ and $(\bar{2}116)$ grain boundaries depicting the distribution of the excess Voronoi volume in Ti (a and b), Mg (b and c), and Zr for the $[0\bar{1}10]$ tilt axis. The black line indicates the twin boundary plane.

6.4 VACANCY BINDING ENERGY

Molecular statics (MS) was used to examine the vacancy binding energy as a function of the local atomic structure and distance from the GB center. Here, the vacancy was placed at all sites within in a block of 3x2 nm near the grain boundary. Then, the change in the vacancy binding energies with increasing distance from the GB center was used to quantify the nonlocal length scale associated with the vacancy binding. The vacancy binding energy (E_b) is essentially the formation energy of a particular site in the GB region, which is normalized with the bulk formation energy ($E_b = E_f – E_f$(bulk), where E_f(bulk) =1.819, 0.868 and 1.385 eV for Ti , Mg and Zr, respectively). Figures 22-24 show the spatial distribution of vacancy binding energies in selected grain boundaries, which is equivalent to representing the variation of vacancy formation energy for a grain boundary system after removing the bulk contribution. Notice that the atoms far away from the boundary are white (0 eV vacancy binding energy), indicating that there is no energy difference over the bulk lattice. For the $(\bar{1}011)$ twin boundary, the minimum vacancy binding energy for Ti, Mg and Zr was found to be -0.438 eV, -0.157 eV and -0.365 eV, respectively (see Figures 22 and 24a). Similarly, for the $(\bar{2}112)$ plane twin boundary, the minimum vacancy binding energy for Ti, Mg and Zr was found to be -0.294 eV, -0.167 eV and -0.134 eV, respectively (see Figure 23). Interestingly, the vacancy binding energy in the $(\bar{1}011)$ and $(\bar{2}112)$ plane twin boundaries were inversely proportional to the excess free volume. For example, the $(\bar{1}011)$ and $(\bar{2}112)$ plane twin boundaries in Ti had more negative vacancy binding energies and the lowest free volume when compared with Mg or Zr. In the case of the $(\bar{2}112)$ plane twin boundary in all three materials, the vacancy binding energy for the 1st layer was lower than that for 0th layer, indicating that the GB center is not necessarily the sink for vacancy. However, the $(\bar{1}011)$ plane twin boundary in all three materials exhibited lower vacancy binding energy for the 0th layer when compared with the 1st layer, suggesting a strong correlation between the GB structural unit and anisotropy associated with the vacancy binding energies. On average, the vacancy binding energies approached bulk values between 3 to 4 layers away from the GB center for the $(\bar{1}011)$ and $(\bar{2}112)$ plane twin boundaries in all different c/a ratio materials examined here.

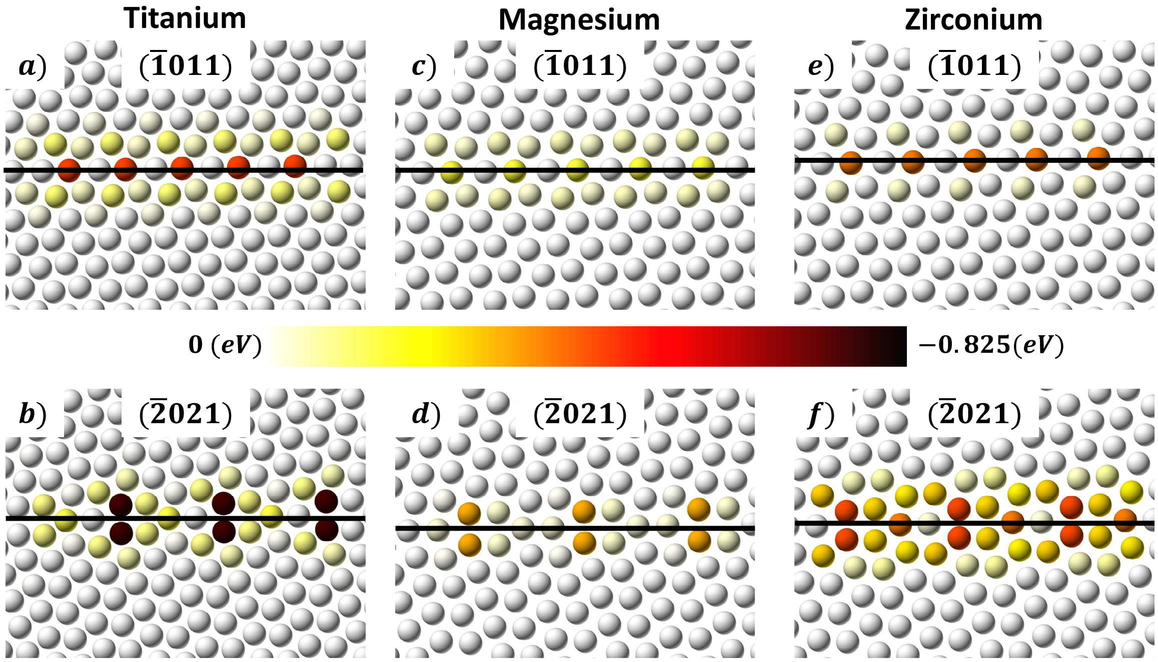

Figure 22: Atomic representation of $(\bar{1}011)$ and $(\bar{2}021)$ grain boundaries depicting the distribution of vacancy binding energies in Ti (a and b), Mg (c and d), and Zr (e and f) for the $[1\bar{2}10]$ tilt axis. The vacancy binding energy in bulk was found to be 1.819, 0.868 and 1.385 eV for Ti, Mg, and Zr, respectively. The black line indicates the twin boundary plane.

For the $(\bar{2}021)$ grain boundary, the minimum vacancy binding energy for Ti, Mg and Zr was found to be -0.743 eV, -0.304 eV and -0.425 eV, respectively (see Figures 22 and 24b). Similarly, for the $(\bar{2}116)$ grain boundary, the minimum vacancy binding energy for Ti, Mg and Zr was found to be -0.777 eV, -0.825 eV and -0.435 eV, respectively (see Figure 23). The vacancy binding energy results of $(\bar{2}021)$ and $(\bar{2}116)$ grain boundaries indicate that there is no significant correlation between the vacancy binding energy and the free volume. For example, the $(\bar{2}021)$ grain boundary in Ti and Zr had similar free volume but significantly different vacancy binding energies. Hence, vacancy binding is not correlated with only one atomic volume; rather, contributions from surrounding atoms also play a role in deciding the potential site for vacancy binding.

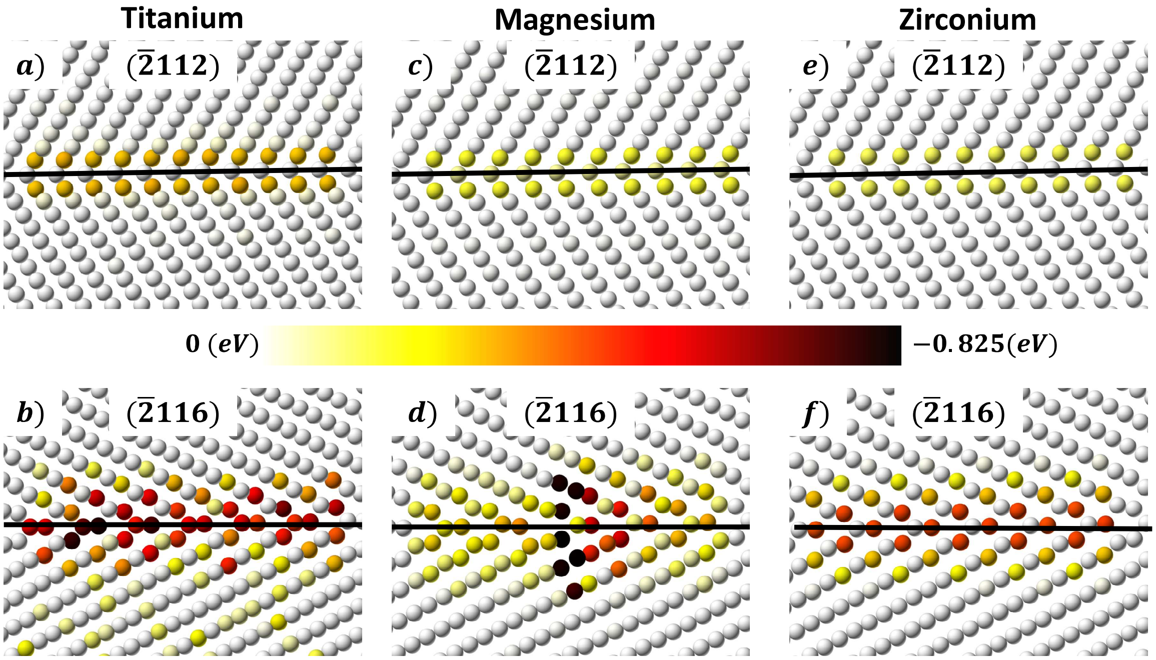

Figure 23: Atomic representation of $(\bar{2}112)$ and $(\bar{2}116)$ grain boundaries depicting the distribution of vacancy binding energies in Ti (a and b), Mg (c and d); and Zr (e and f) for the $[0\bar{1}10]$ tilt axis. Vacancy binding energy in bulk was found to be 1.819, 0.868 and 1.385 eV for Ti, Mg, and Zr, respectively. The black line indicates the boundary plane.

The binding energies of the vacancy can be plotted against the distance from the grain boundary to quantify the evolution of the binding energies near the GB and to quantify the nonlocal length scale associated with the vacancy. Figure 24 is an example of one such plot for vacancy binding energies at various sites for the $(\bar{1}011)$ and $(\bar{2}021)$ grain boundaries. In this plot, the vacancy binding energy was first calculated for each site. Next, a grain boundary region was defined to compare the vacancy binding energies for the $(\bar{1}011)$ and $(\bar{2}021)$ GBs in Ti, Mg, and Zr. Similar to earlier observations that the minimum vacancy binding energy is at 0^{th} layer (grain boundary plane) for the $(\bar{1}011)$ grain boundary (Figure 24a) as compared to the 1^{st} layer for the $(\bar{2}021)$ grain boundary

(Figure 24b), for all c/a ratio materials examined here. Furthermore, in both boundaries, the vacancy binding energies approach bulk values around 5 Å away from the GB center plane.

Overall, for all grain boundaries in the three materials examined here, there were atoms lying symmetrically along the grain boundary plane that had vacancy binding energies close to bulk values or even higher than the bulk values in some cases, i.e., these GBs may not provide pathways for vacancy diffusion. Finally, these figures show that the local environment strongly influences the vacancy binding energies and that these energies are not independent of one another.

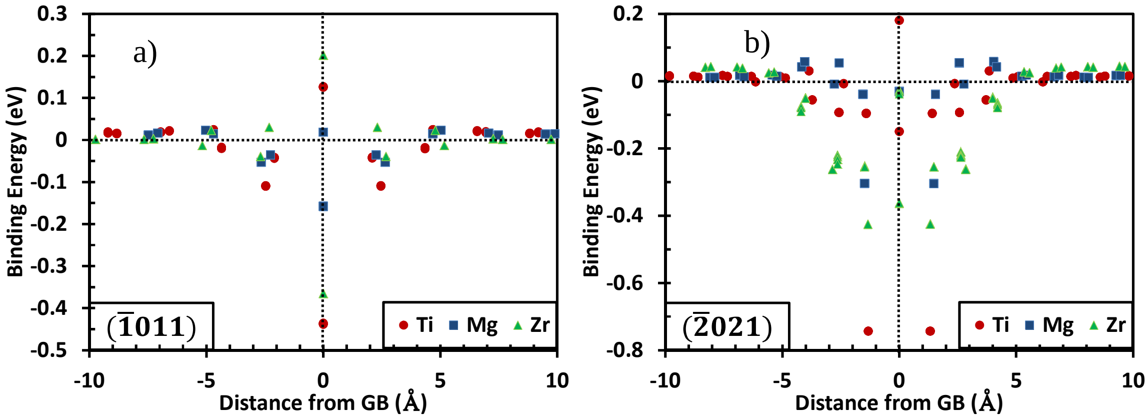

Figure 24: Vacancy binding energy as a function of distance from the grain boundary center: a) the $(\bar{1}011)$ plane boundary, where the vacancy binding energy is minimum energy at the 0th layer of the grain boundary plane, and b) the $(\bar{2}021)$ plane boundary, where the vacancy binding energy is minimum energy at the 1st layer from the grain boundary plane. The vacancy binding energies approach bulk values around 5 Å away from the GB center plane.

6.5 CORRELATING GRAIN BOUNDARY METRICS

The local environment surrounding each atom changes due to interactions with neighboring atoms, which in turn affects the vacancy binding energy and other per-atom properties. In this subsection, we will analyze and correlate calculated vacancy binding energies with grain boundary energies in Ti, Mg, and Zr. The grain boundary energies of all 190 boundaries in all three elements are plotted against the vacancy binding energies of the same boundaries, as shown in Figure 24. The solid line corresponds to a perfect fit with a proportionality constant of -25 Å^2. The results indicate that there is a strong correlation between the grain boundary energy and the vacancy binding energy. Furthermore, there is an overall trend of increasing boundary energy with decreasing binding energy. This could be due to atomic scale roughness when facing two tilted bicrystals together. As such a GB with higher atomic area density will have higher stress fields, which can be relieved through vacancy introduction. Therefore GBs with higher GB energies see a significant drop in the vacancy binding energy.

Here, the linear correlation coefficient r is used (Eq. 15) to compare the degree of correlation between the binding energy and the grain boundary energy, where r = 1 indicates a perfect positive correlation and r = -1 indicates a perfect negative correlation. Interestingly, the vacancy binding energy is highly negatively correlated (r = -0.7144) with the grain boundary energy.

$$r = \frac{\sum x_i y_i - \frac{\sum x_i \sum y_i}{N}}{\sqrt{\sum x_i^2 - \frac{(\sum x_i)^2}{N}}\sqrt{\sum y_i^2 - \frac{(\sum y_i)^2}{N}}} \tag{14}$$

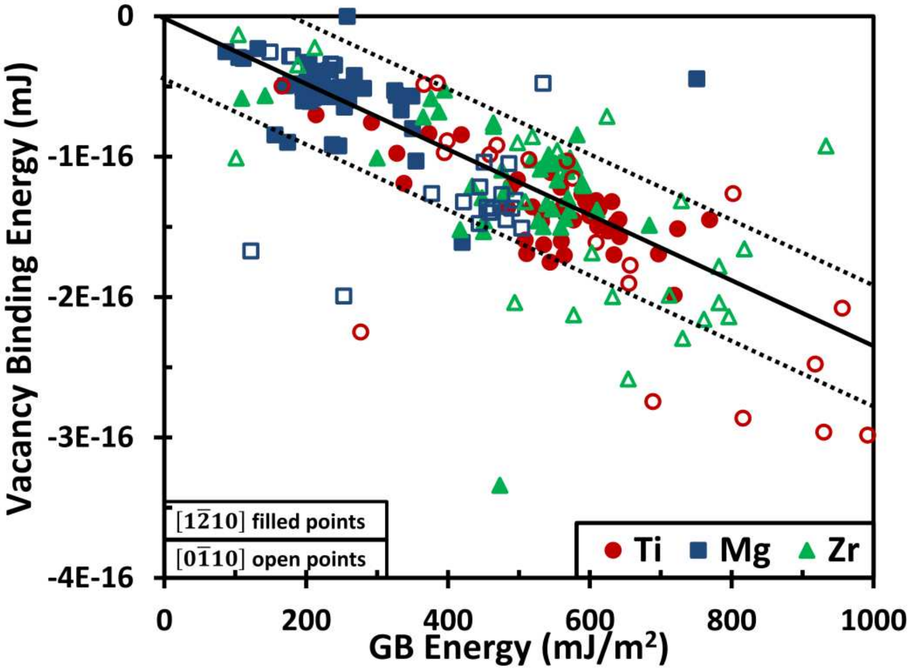

Figure 25: The grain boundary energies of all 190 boundaries in all three elements are plotted against the vacancy binding energies of the same boundaries. Closed data points are for the tilt axis and open data points for the tilt axis. Interestingly, the vacancy binding energy is highly negatively correlated (r = -0.7144) with the grain boundary energy.

6.6 SUMMARY

Molecular static simulations of 190 symmetric tilt grain boundaries in HCP metals were used to understand the energetics of point defects, such as vacancy, which is important for designing stable material interfaces for endurance in harsh environments. The simulation results reveal several interesting observations:

1) The grain boundary local arrangements and resulting structural units have a significant influence on the magnitude of vacancy binding energies, and the site-to-site variation within the boundary is substantial (Figures 22-23) ;

2) Comparing the vacancy binding energies for each site in different c/a ratio materials shows that the binding energy increases significantly with an increase in c/a ratio, see Figure 23-24. For example, in the $[1\bar{2}10]$ tilt axis, Ti and Zr with c/a=1.5811 have a lower vacancy binding energy than the Mg with c/a=1.6299;
3) For all grain boundaries in the three materials examined here, there were atoms lying symmetrically along the grain boundary plane that had vacancy binding energies close to bulk values or even higher than the bulk values in some cases, i.e., these GBs may not provide pathways for vacancy diffusion, see Figures 22-24;
4) In most grain boundaries examined here, the vacancy binding energies approach bulk values around 5 Å away from the GB center plane, see Figure 24;
5) There is no significant correlation between the vacancy binding energy and the atomic free volume; and
6) When the grain boundary energies of all 190 boundaries in all three elements are plotted against the vacancy binding energies of the same boundaries, a highly negative correlation (r = -0.7144) is revealed that has a linter fit with a proportionality constant of -25 Å^2, see Figure 25.

In summary, these new atomistic perspectives provide a physical basis for recognizing the incipient role between the GB character and vacancy binding energies in HCP materials. This is significant for applications where extreme environment damage generates lattice defects and grain boundaries act as sinks for both vacancies and interstitial atoms.

CHAPTER 7

7 SUBSTITUTION SOLUTE EFFECT ON $\{\mathbf{10\bar{1}2}\}$ TWIN BOUNDARY: A DENSITY FUNCTIONAL APPROACH

7.1 INTRODUCTION

Commercially pure titanium is a very attractive and important material with a wide range of application in the aerospace, biomedical, and light sporting material industries (Hanson 1986; Semlitsch, Staub, and Weber 1985). In order to meet the Taylor criteria of five independent deformation mechanisms, plastic deformation in titanium is controlled by slipping and twinning which ultimately controls the mechanical properties of materials (Randle 2004; K. Lu, Lu, and Suresh 2009; Harmer 2011). Earlier work of Akhtar (Akhtar 1975) and Teghtsoonian (Akhtar and Teghtsoonian 1975) on single crystal titanium concludes that deformation at lower temperature involves twinning; whereas, dislocation on the prismatic and basal planes is observed at higher temperature. Twinning in titanium occurs in $\{10\bar{1}2\}$, $\{11\bar{2}2\}$, and $\{10\bar{1}1\}$ planes (Paton and Backofen 1970). Moreover, yield strength and tension-compression asymmetry is closely related to twinning. Hence, understanding the stability of twins and factors affecting nucleation and growth of twins under different loading conditions is a key towards enhanced metal plasticity. Furthermore, as it is very difficult to study the effect of solutes, grain size, and sample size on deformation twins experimentally (L. Lu et al. 2009; Robson, Stanford, and Barnett 2011; Li et al. 2010), atomic scale experimentation or modeling is needed to understand the structure and chemistry of twins in materials.

Continuum theory of point defects in material was first established by Eshelby (Eshelby 1956) in 1956. Later on Maclean(MacLean 1957) used the Arrhenius equation and found that solute segregation is confined to three to four atomic layers from the grain boundary. Segregation of alloying elements in high angle symmetric tilt grain boundaries, which have a network of dislocations, has been thoroughly studied in FCC (Udler and Seidman 1998; Yamaguchi, Shiga, and Kaburaki 2005), BCC (Jin, Elfimov, and Militzer 2014; Kiejna and Wachowicz 2008), and HCP (Huber, Rottler, and Militzer 2014). Recently coherent twin boundaries in magnesium have been investigated by Nie et al. (Nie et al. 2013) where they have found that an ordered periodic segregation of solute at twin boundaries was driven by minimization of the total elastic energy hence providing stability and strengthening of twin boundaries.

7.2 METHODOLOGY

In this work, to elucidate the effect of solute on the $\{10\bar{1}2\}$ twin boundary in titanium, we use first principles methods. The $(10\bar{1}2)$ twin boundary was created initially in LAMMPS (Plimpton 1995) with the Zope and Mishin (Zope and Mishin 2003) interatomic potential. The twin boundary structure obtained using the EAM potential was further relaxed using the Vienna Ab-initio Simulation Package (VASP) plane wave electronic structure code (G. Kresse and Furthmüller 1996b; G. Kresse and Furthmüller 1996a) with a conjugate gradient algorithm and 1 meV total free energy change convergence criteria. Projector augmented wave (PAW) potentials (G. Kresse and Joubert 1999; P. E. Blöchl 1994) were used to represent the nuclei core with valence electrons on s and d orbitals for α-Ti. Exchange and correlation was treated with GGA using the PBE

(Perdew, Burke, and Ernzerhof 1997) form with an energy cutoff of 289 eV and the Monkhorst (Monkhorst and Pack 1976) Pack k-point with gamma mesh of 6 x 9 x 18 along the normal to the $(10\bar{1}1)$ (x-axis), $(10\bar{1}2)$ (y-axis), and $(1\bar{2}10)$ (z-axis) planes respectively. A single substitution solute atom was introduced at different potential sites around the twin boundary as shown in Figure 26a. It should be noted here that the solute atom was free to relax in all directions during the minimization.

7.3 SEGREGATION ENERGY

Figure 26a shows the spatial distribution of excess atomic volume for the $(10\bar{1}2)$ twin boundary in Ti. Notice that the atoms far away from the boundary are green (0 $Å^3$ excess Voronoi volume) indicating that there is no atomic volume difference over the bulk lattice. The bulk Voronoi volume was found to be 17.57 $Å^3$. The excess Voronoi volume is highest/lowest (tensile versus compressive) at the twin boundary center and converges to the bulk Voronoi volume as distance from the grain boundary increases. Moreover, the potential site for solute binding with the twin boundary has been marked by numbers where the twin boundary has two sites: one with compressive hydrostatic stress and another with tension. Figure 26b shows the segregation of solute atoms at different potential sites from the twin boundary which converge to zero at around 4-5 atomic layers (5 Å). Based on the atomic size, all atoms with size less than titanium will segregate at a compressive site (0) to relieve compressive stress whereas atoms with size bigger than titanium will prefer a tension site (0') due to the availability of excess volume. Cobalt has a maximum segregation of -0.544 eV at a compressive site and yttrium has a maximum segregation of -0.522 eV at a tension site whereas tin has a minimum segregation of -0.07 eV at tension site. This result can be explained by the difference in the atomic size of different solutes with titanium. Cobalt and yttrium have a bigger atomic size difference; whereas, tin has the lowest atomic size difference with titanium.

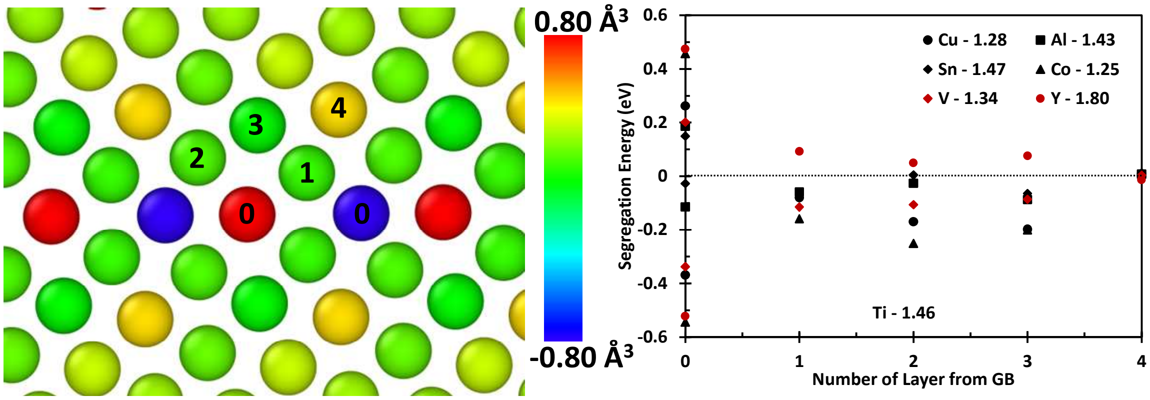

Figure 26: a) Potential site for substitution of atoms in (10$\bar{1}$2) twin boundary in titanium. Atoms are colored according to voronoi volume. b) Segregation of different atoms at different sites on (10$\bar{1}$2) twin boundaries. Blue atom at Layer 0 of twin boundary is under hydrostatic compression; whereas, red atom is under hydrostatic tension. Yttrium has high tendency to segregate only at Layer 0 with 0.522 eV due to high miscibility

7.4 SEGREGATION ENERGY WITH TEMPERATURE

The Langmuir-McLean theory (MacLean 1957) for segregation of a solute to a GB is

$$\frac{X_{GB}}{X_{GB}^{0}-X_{GB}} = \frac{X_b}{1-X_b}\exp\left({}^{E}/_{k_BT}\right) \tag{15}$$

where X_{GB}^{0} indicates saturation of the GB at 0 K, $X_b$is the solute concentration in bulk, E is the binding or segregation energy, and T is the temperature. White and Coghlan (White and Coghlan 1977) revised this equation for solute segregation at the boundary by taking into consideration binding distribution around the boundary as $X_{GB} = \sum F_i X_{GB,i}$, where $X_{GB,i}$ is given by

$$X_{GB,i} = (1 + \left(\frac{1-X_b}{X_b}\right) \exp\,(-E_i/k_B T))^{-1} \tag{16}$$

Figure 27a shows the weight average as a function of atomic volume for a $(10\bar{1}2)$ twin boundary. The dotted line represents the bulk atomic volume. Figure 27b shows the evolution of solute segregation as a function of temperature for 0.7 bulk concentration. Since atomic size difference between yttrium and titanium is very high, the twin boundary has very high solute segregation at lower temperature. This means all the solute will be concentrated at the twin boundary and none will be segregated in bulk. Moreover, as temperature increases yttrium migrates towards the bulk decreasing the segregation concentration at the twin boundary due to an increase in the lattice constant with temperature. Furthermore, all other solutes have a value in the range of 0.4 ~ 0.5 at 100 K. As temperature increases, more solute segregates at the twin boundary from the bulk.

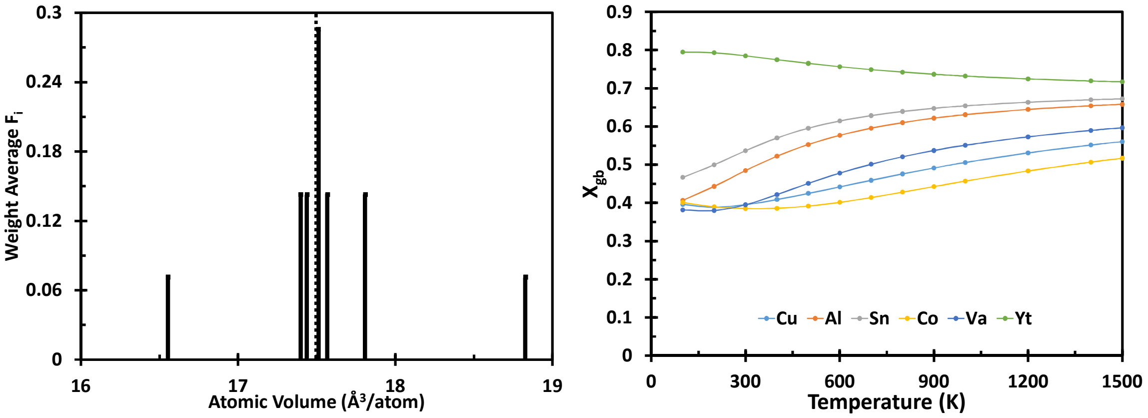

Figure 27: a) Weight average F_i as a function of voronoi volume for $(10\bar{1}2)$ twin boundary in titanium. Note: Dashed line represents the weight average of bulk voronoi volume. b) Solubility of different elements on $(10\bar{1}2)$ twin boundary for 0.7 bulk solubility as a function of temperature. Yttrium has lower miscibility with titanium, and hence, yttrium segregates more easily at the twin boundary as compared to other elements compared here.

7.5 CHARGE DENSITY WITH SOLUTE

The mechanical properties of a material are defined by the nature of the atomic bonding. Bonding between atoms is the result of the polarization of charge densities around the nuclei. Both the shear strength and cohesive strength are affected by bond directionality and also by charge distribution around atoms. Therefore, understanding the change in charge density with a solute is necessary for evaluating the shear strength of a material and the subsequent effect on the plastic deformation behavior (see Song, Guo, and Yang 2002). Figure 28 presents a 3D iso-surface plot for charge density (differential) showing the effect of solute at the twin boundary. The yellow and cyan iso-surfaces represent charge accumulation and depletion, respectively. In comparison with the charge density distribution of a pure twin boundary, the main change for a solute at the twin boundary seems to be different for different solutes as seen in Figure 28. The charge densities between Ti atoms were evidently changed with the addition of a solute at the boundary resulting in a change in the shear modulus which affects the twin boundary growth as the shear stress is proportional to the shear modulus. Cobalt (Co) has directional anisotropy in bonding with surrounding titanium atoms due to directional d-orbital binding. Cobalt shows strong bonding parallel and perpendicular to the twin boundary plane which can be attributed to valence d orbital bonding and, hence, will provide more barriers in twin boundary growth as compared to other solutes. On the other hand, tin (Sn) has very isotropic bonding with the surrounding titanium atoms because of the tin s-orbital binding with the titanium s-orbital which is spherical in nature; whereas, aluminum (Al) and copper (Cu) have the valence p-orbital interacting with the s-orbital of titanium and show a little anisotropy in bonding but not as much as Co.

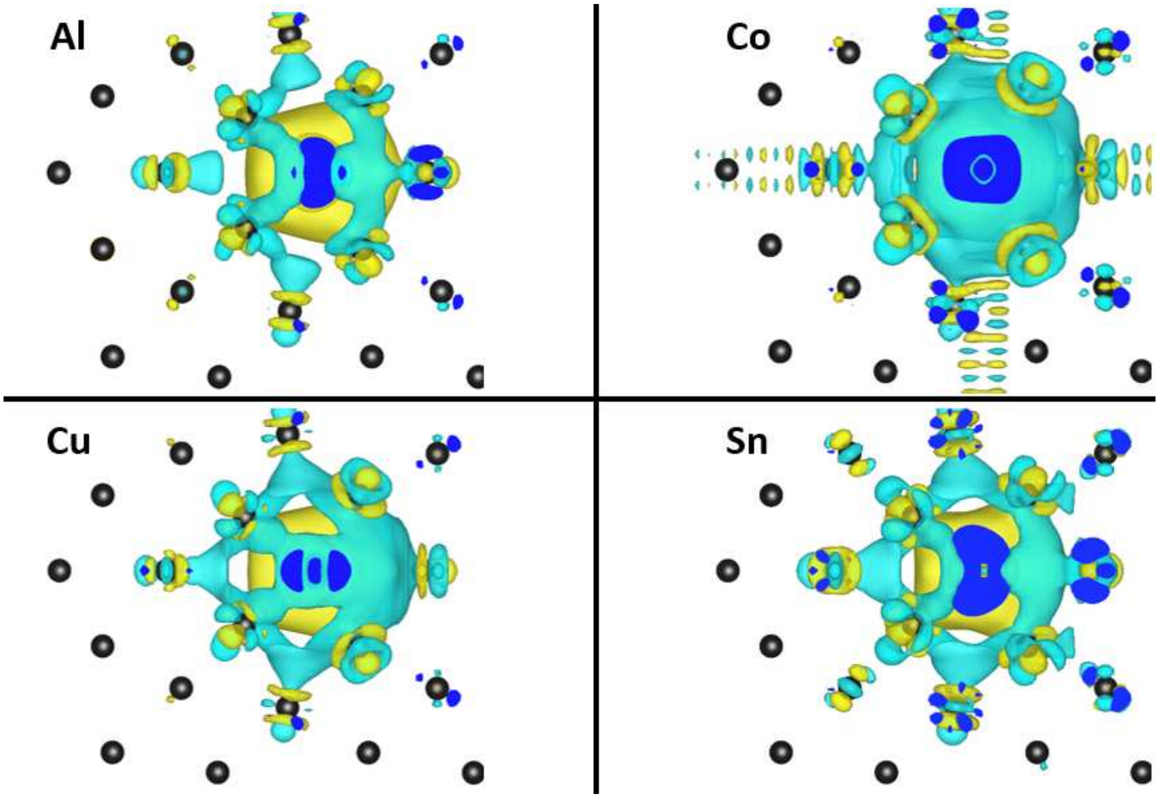

Figure 28: A 3D iso-surface plot for charge density showing the effect of a substitution atom on the $(10\bar{1}2)$ twin boundary in titanium. The yellow and cyan iso-surfaces represent charge accumulation and depletion, respectively. Aluminum and tin have isotropic bonding with titanium atoms; whereas, cobalt bonds anisotropically with the titanium grain boundary.

7.6 SUMMARY

In summary, all of the solute atoms prefer to bind at the 0^{th} plane of the grain boundary. Al which is smaller than titanium prefer compression sites; whereas, bigger solutes prefer tension sites. Moreover, using the revised McLean theory, we see 100% yttrium segregation at the $(10\bar{1}2)$ twin boundary at lower temperature because yttrium is 30% bigger in radius than titanium; whereas, at higher temperature, the tendency of yttrium segregation at the twin boundary decreases due to an increase in the lattice size. However, all other solute elements have a higher tendency to segregate at the twin boundary at higher temperatures rather than at lower temperatures. Furthermore, looking at the local bonding of a solute with the surrounding titanium atoms, cobalt shows anisotropy in bonding due to the interaction of the valence d orbital with the d orbital of titanium. All other elements show isotropy when bonded at the twin boundary.

CHAPTER 8

8 SLIP TRANSFER ACROSS A GRAIN BOUNDARY: A MOLECULAR DYNAMIC APPROACH

8.1 INTRODUCTION

The mechanical properties of crystalline materials are strongly governed by the presence of obstacles (point defects, solute atoms, dislocation network, grain boundaries, and precipitates) to dislocation motion. The GBs have the strongest influence on the strengthening by presenting an effective barrier to dislocation motion (Hall-Petch effect). On the other hand, strain accumulation at the GBs due to dislocation pileup can lead to crack nucleation if a feasible release for the dislocations is not available.

There are four possible outcomes of dislocation-grain boundary interactions (Figure 29): a) a direct transmission; b) a direct transmission with a residual dislocation along the grain boundary; c) an indirect transmission with a residual dislocation occurring because the incoming and outgoing slip planes do not intersect; and d) no transmission because the dislocation is absorbed at the grain boundary. Furthermore, the slip-grain boundary interactions can be summarized in terms of the Burgers vector of the incident (b_i), transmitted (b_t), and the residual dislocations (b_r).

$$\overrightarrow{b_\iota} \rightarrow \overrightarrow{b_t} + \overrightarrow{b_r} \tag{17}$$

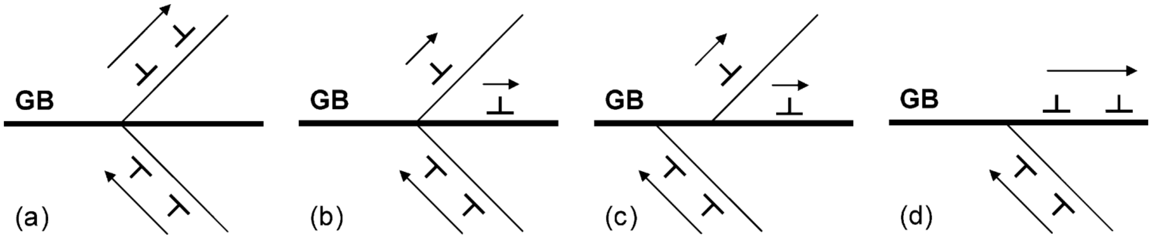

Figure 29: Slip-grain boundary interaction cases: (a) a direct transmission and dislocation cross-slip; (b) a direct transmission with a residual dislocation along the grain boundary; (c) an indirect transmission with a residual dislocation where slip planes in each grain do not intersect; and (d) no transmission.

A slip transmission criterion across the grain boundary was first proposed by Livingston (Livingston and Chalmers 1957). Later the model was extended by others to maximize the critical resolved shear stress on the transmitted slip system (Shen, Wagoner, and Clark 1986; Shen, Wagoner, and Clark 1988; Clark et al. 1992). Lee et al. (Lee, Robertson, and Birnbaum 1989) added a requirement on predicting the transmitted slip system by ensuring minimum residual dislocations along the grain boundary. Based on Stroh's theory, dislocation pileup at these interfaces induces a shear stress (formation of slip band (PSB) and extrusion) and combined with progressive applied stress, opens up to nucleate, instigate, or incubate a crack. Hence, stable pileup energy would govern the crack initiation and therefore is necessary to investigate this problem at a smaller scale.

The energy barrier for dislocation transmission across the GB can be calculated by placing a control volume at the site of the dislocation and GB interaction. Inside the control volume only the defected atoms (9 > centrosymmetry parameter (Kelchner, Plimpton, and Hamilton 1998) > 6) were retained for further analysis. The energy of these selected atoms is tracked (E_{load}) and the relaxed energy of these atoms ($E_{relaxed}$)

was subtracted during the loading process. The net energy was normalized with the atomic volume of occupied defect atoms (Equation 18).

$$E_{barrier} = \frac{\sum_i^n E_{load} - E_{relaxed}}{V} \tag{18}$$

Thus, in this chapter we present a preliminary understanding on the effect of grain boundary atomic structure on the GB-dislocation interaction. The dislocation grain boundary interactions were quantified by computing the barrier energy of the GB interface.

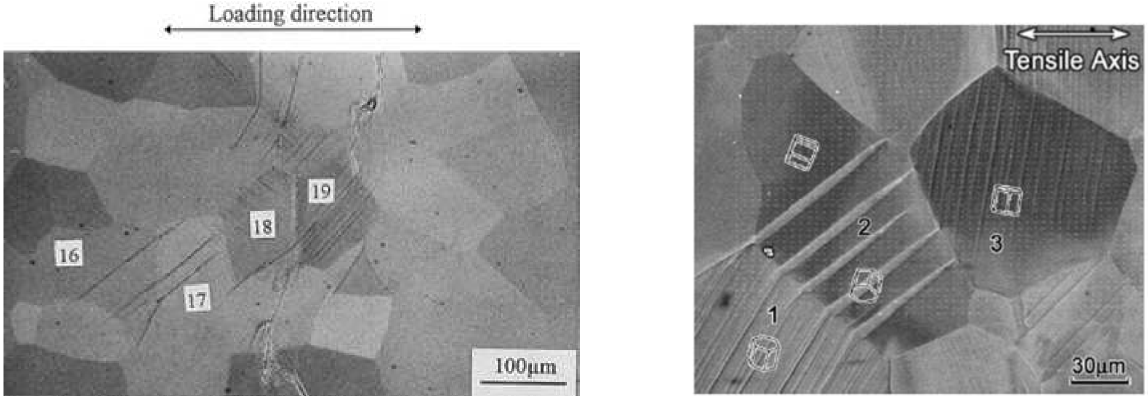

Figure 30: a) slip band cracks across the grain boundary in the case of grain 16 and grain 17 and b) deformation twins in grain 2 appear to have been nucleated at the grain boundary with grain 1. The slip bands in grain 1 and the deformation twins in grain 2 are correlated. Figure 30 was adopted from Wang et al. (L. Wang et al. 2010)

Recently, Wang et al. (L. Wang et al. 2010) showed formation of cracks due to the interaction of twin-twin and slip band formation as seen in Figure 30a. Moreover, he also has shown deformation twins nucleation from the grain 1-grain 2 grain boundary (Figure 30b) and propagates towards the grain boundary of grain 2-grain 3 (Figure 30b), based on the difference in the thickness of the twin at the grain boundary of grain 1-grain 2 as compared with the grain boundary of grain 2-grain 3. Furthermore, a slip-twin correlation with the help of the Luster-Morris parameter (Luster and Morris 1995); wherein, the prismatic slip interacts with the grain boundary and nucleates a deformation twin in the adjacent grain even though the c-axis of the grain is oriented at 45˚ to the loading axis which is unfavorable for twinning according to the Schmidt factor. Our main objective was to quantify all of the possible outcomes of slip/ twin interaction with the grain boundary interaction.

8.2 METHODOLOGY

MD simulations were used to study the dislocation interaction with twin boundaries and STGBs (Figure 31) in α-Ti using EAM potential developed by Zope et al. (Zope and Mishin 2003) at a temperature of 10 K. The GB structure and minimum energy were calculated using a bicrystal simulation cell with three-dimensional (3D) periodic boundary conditions using a methodology described in detail in chapter 6 section 2.

Figure 31 shows the variation of GB energy as a function of GB geometry in a stereographic triangle representation, which is widely used to represent crystal systems. This was achieved by defining the polar and azimuthal angles for the GB database studied (Rajagopalan et al. 2014; Bhatia and Solanki 2013). Some of the coincident site lattice (CSL) GBs corresponding to the local minima in the energy distribution for the respective tilt systems (Figure 31a). For example, the $(\bar{1}011)$, θ=61.28° GB corresponds to a coherent compression twin and the $(\bar{1}012)$, θ=42.39° GB corresponds to a coherent tension twin boundary showing a more pronounced cusp in the GB energy (refer to Figure 31a). All the GB energies were consistent with previously reported findings in literature (Jian Wang and Beyerlein 2012a; Jian Wang and Beyerlein 2012b).

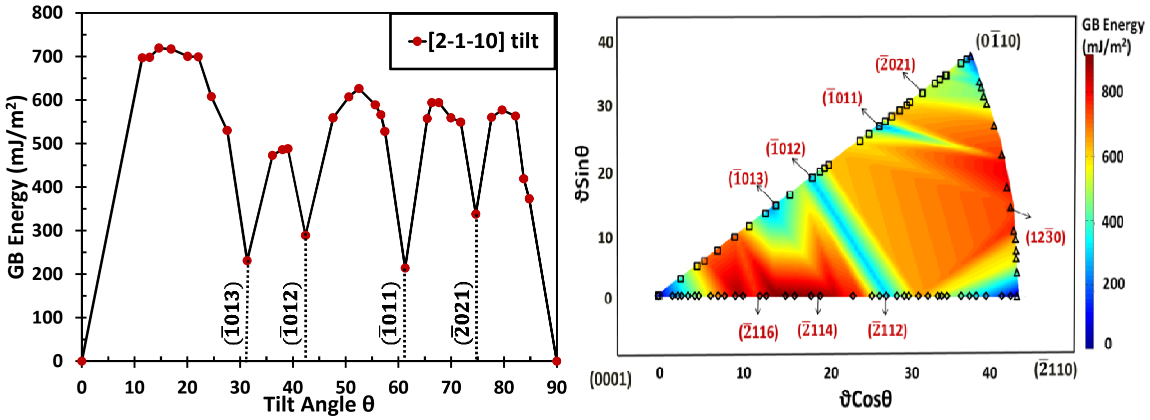

Figure 31: a) $[2\bar{1}\bar{1}0]$ symmetric tilt grain boundary energy (STGB) as a function of misorientation θ from the [0001] direction in Ti. b) Contour plot of GB energies for the three symmetric tilt systems of Ti represented using polar and azimuthal angles. The polar and azimuthal angles correspond to the degrees of freedom.

8.2 SLIP-TWIN CORRELATION

A $[\bar{2}114]$ STGB with c-axis at θ=42.39° to the loading axis is deformed under tension with a crack as the source of the dislocation. Figure 32 shows the microstructure evolution with applied strain and the corresponding evolution of energy with the control volume with applied strain. Basal dislocation nucleates from the crack in grain 1 (soft grain) and interacts with the grain boundary. Twin nucleation from the GB site of the dislocation absorption and propagation in grain 2 with increase in applied strain as seen in figure 32c. This behavior was consistent as it requires more stress to nucleate a twin in a hard grain (grain 2). Moreover, the Schmidt factor for $(11\bar{2}1)$ twin nucleation was found to be 0.36 which is lower compared to the Schmidt factor of 0.48 for basal slip. The Luster parameter (Luster and Morris 1995) can be calculated to correlate slip-twin behavior in subsequent grains.

$$E_{barrier} = \frac{\sum_i^n E_{load} - E_{relaxed}}{V}$$

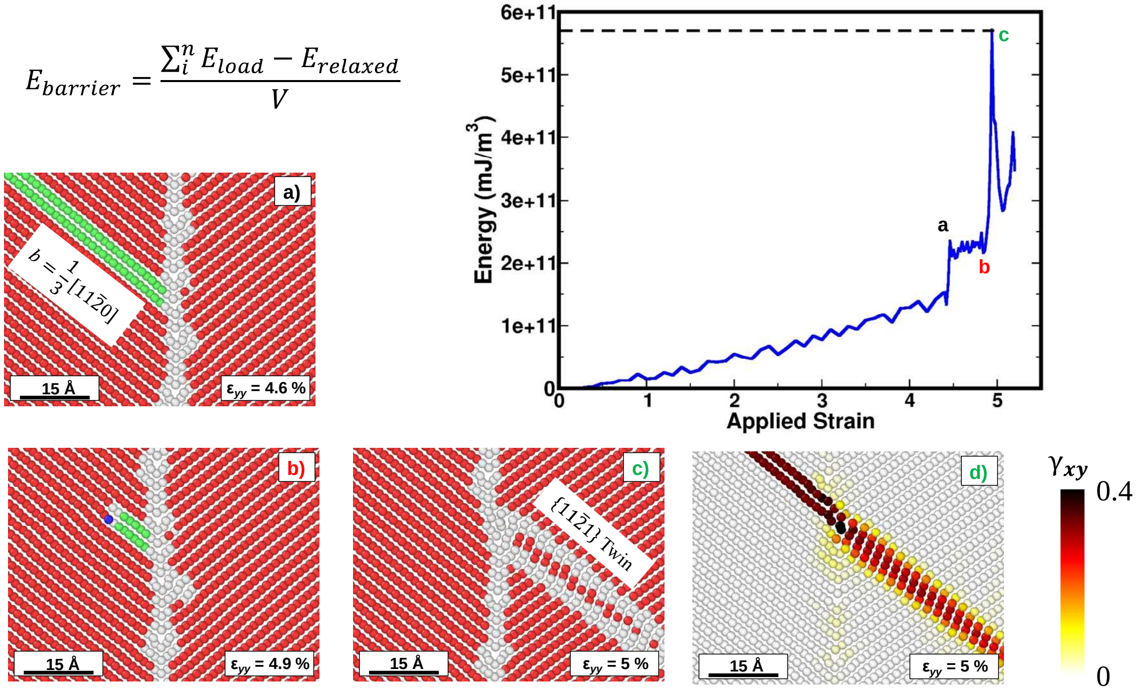

Figure 32: a) Interaction of basal dislocation with $(\bar{2}114)$ grain boundary b) dislocation is absorbed at the grain boundary at around 4.9% strain, c) $(11\bar{2}1)$ twin nucleation from grain boundary, and d) residual shear strain showing trace of dislocatin glide and nucleation of a twin. Equation is the energy barrier equation to measure the grain boundary barrier energy.

8.3 ENERGY BARRIER FOR SLIP TRANSMISSION

Seven different grain boundaries from the $[\bar{2}110]$ and $[0\bar{1}10]$ tilt axes were deformed to study the slip-grain boundary interaction. A power law similar to Sangid et al. (Sangid et al. 2011) was fitted between the energy barrier and the static grain boundary energy as shown in Figure 33. The $(10\bar{1}2)$ coherent twin boundary has the lowest interface energy, on the other hand the highest barrier to the slip transmission which contributes to the strengthening of the material as also seen in experiments. These findings are in agreement with intuition i.e. as interface energy increases, there is more excess volume available at the grain boundary and; hence, the lower barrier for slip transfers. From the power law fit obtained from our results two material parameters namely $E_{barrier} = 2 * 10^{14}$ and transfer rate $m = 1.05$ can be used for the higher length scale modeling.

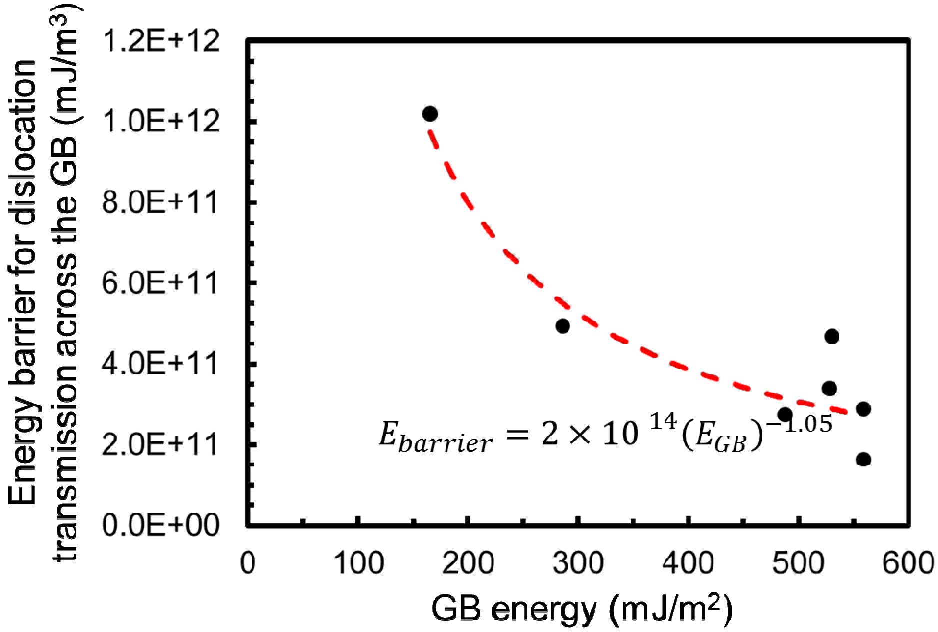

Figure 33: The dislocation transmission energy barrier across a grain boundary as a function of the grain boundary energy in Titanium.

Nine different grain boundaries from the $[\bar{2}110]$ and $[0\bar{1}10]$ tilt axis were selected to study the dislocation nucleation from the GB. A power law function was fit to the energy barrier against the static grain boundary energy as shown in figure 34 for a dislocation emission. The $(10\bar{1}2)$ coherent twin boundary has the lowest interface energy and, hence, the highest barrier for the dislocation emission, which contributes to strengthening of the material as also seen in experiments. Moreover, as interface energy increases, there is more excess volume available at the grain boundary and, hence, less barrier to nucleate a dislocation. From the power law fit of our result, we found two material parameters namely $E_{barrier} = 4 * 10^{17}$ and nucleation rate m = 2.18 which can be used for the higher length scale modeling. Due to the presence of a pristine defect free crystal around the grain boundary the energy barrier for nucleation of dislocations is higher than the energy barrier for slip transfer.

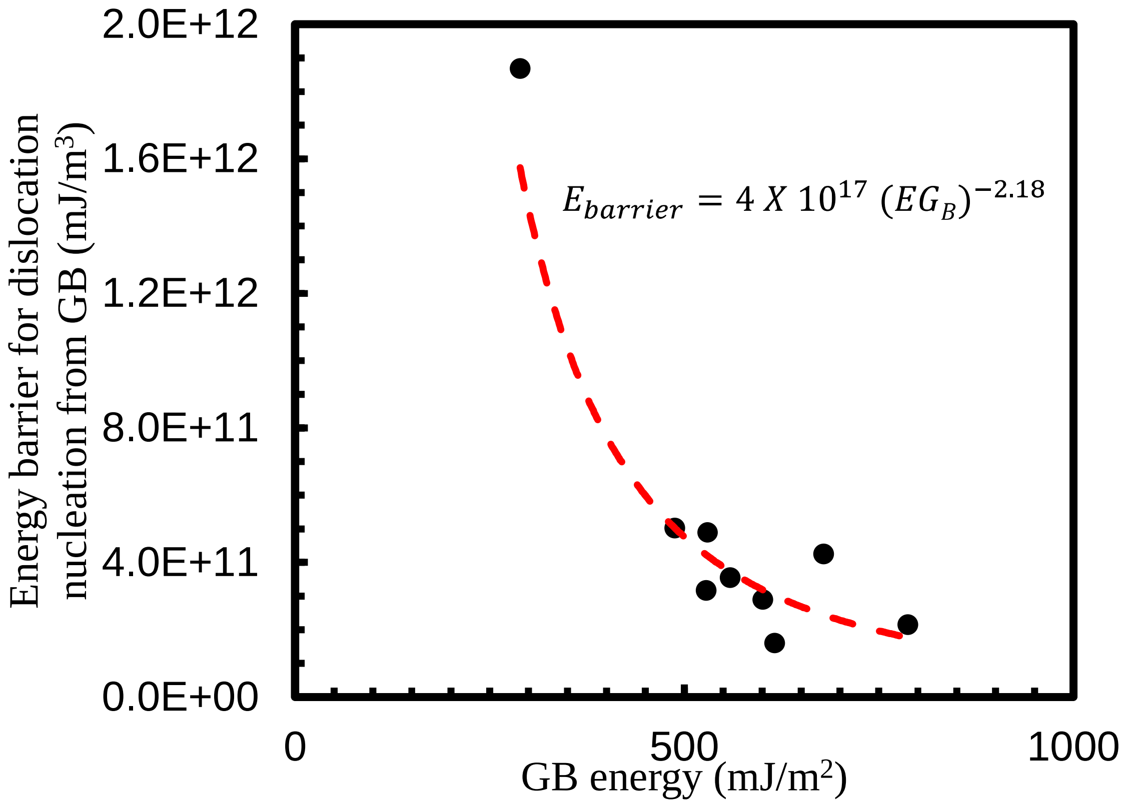

Figure 34: The dislocation nucleation energy barrier from various STGBs as a function of the grain boundary energy in Titanium.

8.4 SUMMARY

In summary, the energy barrier for dislocation nucleation is higher than that for the slip transfer due to the presence of a pristine lattice during nucleation. Moreover, $(10\bar{1}2)$ twin boundary has highest energy barrier for slip transfer and hence we proposed that a higher fraction of $(10\bar{1}2)$ in material will have higher fraction of transgranular fracture as compared to intergranular fracture.

CHAPTER 9

9 FUTURE WORK

9.1 Bond order potential (BOP)

The valence d-orbital electrons play a crucial role in the determination of cohesive energy and the ground state structure for transition metals such as titanium (Pettifor 1995). The energy equation with a tight binding scheme has two parts, i.e., the first term is the bond energy arising from the valence d-orbital band that depends on the bond angle and the second term is the pairwise part for the repulsion and electrostatic interaction of atoms (Sutton et al. 1988). Hence, in the tight binding framework, the free energy of N atoms in titanium situated at rest position R is given by:

$$F = \frac{1}{2}\sum_{i \neq j} V(R_{ij}) + F_i \tag{19}$$

where $V(R_{ij})$ is the pairwise repulsive part and F_i is the bond energy part which depends on both the bond integral and the bond order and is given by.

$$U_{bond}^{ij} = \sum_{\alpha\beta} 2H_{i\alpha,j\beta}\Theta_{j\beta,i\alpha} \tag{20}$$

where the bond energy U_{bond}^{ij} is a function of Hamiltonian $H_{i\alpha,j\beta}$ and the bond-order matrix element $\Theta_{j\beta,i\alpha}$ that are associated with an individual bonds *i-j* and corresponding atomic orbitals *α and β*. Moreover, the fitting of bond energy part involves the bond integral i.e., the hoping of electron along ddπ and ddσ for a Ti-Ti bonding which is by

$$dd\tau(R) = dd\tau_0(\frac{{R_0}^{Ti-Ti}}{R})^{n_{Ti-Ti}} \tag{21}$$

Where, Ro denotes the nearest Ti-Ti spacing in hcp Ti. R is the variable which is varied from Ro to R-cutoff. The π and σ are bond integrals, which form at the inter-site

Hamiltonian matrix can be obtained indirectly by fitting the band structure (Figure35). Another term in the fitting bond energy involves the bond order which is basically a subtraction of number of electrons in anti-bonding orbitals with number of electrons in bonding orbitals divided by two.

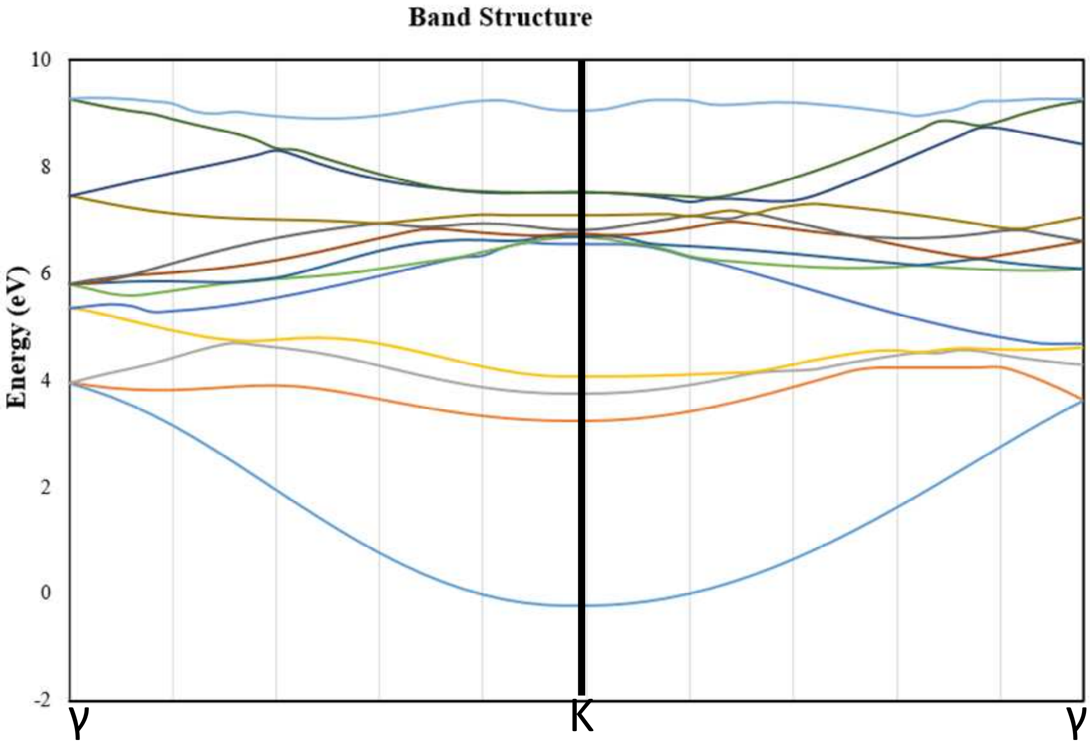

Figure 35: Band structure of bulk Ti from γ-K-γ, where γ is at (0,0,0)and K is at (a,0,0). Bond integral π and σ is obtained by fitting the band structure with the inverse Fourier transformation.

Fitting of pairwise repulsive part involves functional form of potential. Hence, equilibrium properties such as cohesive energy, electronic density of states, experimental elastic moduli and volume-energy curve for the equilibrium structure of titanium can be used to develop a functional form for a pairwise repulsive part.

REFERENCES

Ackland, Graeme J. 1992. “Theoretical Study of Titanium Surfaces and Defects with a New Many-Body Potential.” *Philosophical Magazine A* 66 (6): 917–32.

Akhtar, A. 1975. “Basal Slip and Twinning in A-Titanium Single Crystals.” *Metallurgical Transactions A* 6 (5): 1105–13.

Akhtar, A., and E. Teghtsoonian. 1975. “Prismatic Slip in A-Titanium Single Crystals.” *Metallurgical and Materials Transactions A* 6 (12): 2201–8.

Albaret, Tristan, Fabio Finocchi, and Claudine Noguera. 1999. “Ab Initio Simulation of Titanium Dioxide Clusters.” *Applied Surface Science* 144: 672–76.

Baskes, M. I. 1992. “Modified Embedded-Atom Potentials for Cubic Materials and Impurities.” *Physical Review B* 46 (5): 2727.

Bhatia, M. A., S. Groh, and K. N. Solanki. 2014. “Atomic-Scale Investigation of Point Defects and Hydrogen-Solute Atmospheres on the Edge Dislocation Mobility in Alpha Iron.” *Journal of Applied Physics* 116 (6): 064302. doi:10.1063/1.4892630.

Bhatia, M. A., and K. N. Solanki. 2013. “Energetics of Vacancy Segregation to Symmetric Tilt Grain Boundaries in Hexagonal Closed Pack Materials.” *Journal of Applied Physics* 114 (24): 244309. doi:10.1063/1.4858401.

Bieler, T. R., M. A. Crimp, Y. Yang, L. Wang, P. Eisenlohr, D. E. Mason, W. Liu, and G. E. Ice. 2009. “Strain Heterogeneity and Damage Nucleation at Grain Boundaries during Monotonic Deformation in Commercial Purity Titanium.” *JOM* 61 (12): 45–52.

Bieler, T. R., M. G. Glavicic, and S. L. Semiatin. 2002. “Using OIM to Investigate the Microstructural Evolution of Ti-6Ai-4V.” *JOM* 54 (1): 31–36.

Blöchl, P. E. 1994. “Projector Augmented-Wave Method.” *Physical Review B* 50 (24): 17953–79. doi:10.1103/PhysRevB.50.17953.

Blöchl, Peter E. 1994. “Projector Augmented-Wave Method.” *Physical Review B* 50 (24): 17953.

Brandes, M. C., M. Baughman, M. J. Mills, and J. C. Williams. 2012. “The Effect of Oxygen and Stress State on the Yield Behavior of Commercially Pure Titanium.” *Materials Science and Engineering: A* 551: 13–18.

Bulatov, Vasily V., and Efthimios Kaxiras. 1997a. “Semidiscrete Variational Peierls Framework for Dislocation Core Properties.” *Physical Review Letters* 78 (22): 4221.

———. 1997b. “Semidiscrete Variational Peierls Framework for Dislocation Core Properties.” *Physical Review Letters* 78 (22): 4221–24. doi:10.1103/PhysRevLett.78.4221.

Cerreta, E., G. T. Gray III, A. C. Lawson, T. A. Mason, and C. E. Morris. 2006. “The Influence of Oxygen Content on the A to $ømega$ Phase Transformation and Shock Hardening of Titanium.” *Journal of Applied Physics* 100 (1): 013530.

Chang, Jinpeng, Wei Cai, Vasily V Bulatov, and Sidney Yip. 2002. “Molecular Dynamics Simulations of Motion of Edge and Screw Dislocations in a Metal.” *Computational Materials Science* 23 (1–4): 111–15. doi:10.1016/S0927-0256(01)00221-X.

Chaussidon, Julien, Marc Fivel, and David Rodney. 2006. “The Glide of Screw Dislocations in Bcc Fe: Atomistic Static and Dynamic Simulations.” *Acta Materialia* 54 (13): 3407–16.

Chen, Di, Jing Wang, Tianyi Chen, and Lin Shao. 2013. “Defect Annihilation at Grain Boundaries in Alpha-Fe.” *Scientific Reports* 3. http://www.nature.com/srep/2013/130322/srep01450/full/srep01450.html?WT.ec_id=SREP-639-20130402.

Chen, Y. J., Y. J. Li, J. C. Walmsley, S. Dumoulin, P. C. Skaret, and H. J. Roven. 2010. “Microstructure Evolution of Commercial Pure Titanium during Equal Channel Angular Pressing.” *Materials Science and Engineering: A* 527 (3): 789–96.

Chichili, D. R., K. T. Ramesh, and K. J. Hemker. 1998. “The High-Strain-Rate Response of Alpha-Titanium: Experiments, Deformation Mechanisms and Modeling.” *Acta Materialia* 46 (3): 1025–43.

Christian, J. W., and V. Vítek. 1970. “Dislocations and Stacking Faults.” *Reports on Progress in Physics* 33 (1): 307. doi:10.1088/0034-4885/33/1/307.

Churchman, A. T. 1954. “The Slip Modes of Titanium and the Effect of Purity on Their Occurrence during Tensile Deformation of Single Crystals.” *Proceedings of the Royal Society of London. Series A. Mathematical and Physical Sciences* 226 (1165): 216–26.

Clark, W. A. T., R. H. Wagoner, Z. Y. Shen, T. C. Lee, I. M. Robertson, and H. K. Birnbaum. 1992. “On the Criteria for Slip Transmission across Interfaces in Polycrystals.” *Scripta Metallurgica et Materialia* 26 (2): 203–6. doi:10.1016/0956-716X(92)90173-C.

Conrad, Hans. 1981. “Effect of Interstitial Solutes on the Strength and Ductility of Titanium.” *Progress in Materials Science* 26 (2): 123–403.

Davis, Joseph R. 1990. *Properties and Selection: Nonferrous Alloys and Special-Purpose Materials*. Vol. 2. Asm Intl.

Daw, Murray S., and M. I. Baskes. 1983. “Semiempirical, Quantum Mechanical Calculation of Hydrogen Embrittlement in Metals.” *Physical Review Letters* 50 (17): 1285.

Daw, Murray S., and Michael I. Baskes. 1984. “Embedded-Atom Method: Derivation and Application to Impurities, Surfaces, and Other Defects in Metals.” *Physical Review B* 29 (12): 6443.

De la Rubia, Tomas Diaz, Hussein M. Zbib, Tariq A. Khraishi, Brian D. Wirth, Max Victoria, and Maria Jose Caturla. 2000. “Multiscale Modelling of Plastic Flow Localization in Irradiated Materials.” *Nature* 406 (6798): 871–74.

Dong, H., and X. Y. Li. 2000. “Oxygen Boost Diffusion for the Deep-Case Hardening of Titanium Alloys.” *Materials Science and Engineering: A* 280 (2): 303–10.

Ercolessi, Furio, and James B. Adams. 1994. “Interatomic Potentials from First-Principles Calculations: The Force-Matching Method.” *EPL (Europhysics Letters)* 26 (8): 583.

Eshelby, J. D. 1956. “The Continuum Theory of Lattice Defects.” *Solid State Physics* 3: 79–144.

Fisher, E. S., and C. J. Renken. 1964. “Single-Crystal Elastic Moduli and the Hcp→ Bcc Transformation in Ti, Zr, and Hf.” *Physical Review* 135 (2A): A482.

Franciosi, P., M. Berveiller, and A. Zaoui. 1980. “Latent Hardening in Copper and Aluminium Single Crystals.” *Acta Metallurgica* 28 (3): 273–83.

Friedel, J. 1952. “XIV. The Distribution of Electrons Round Impurities in Monovalent Metals.” *Philosophical Magazine* 43 (337): 153–89.

Ghazisaeidi, M., and D. R. Trinkle. 2012. “Core Structure of a Screw Dislocation in Ti from Density Functional Theory and Classical Potentials.” *Acta Materialia* 60 (3): 1287–92. doi:10.1016/j.actamat.2011.11.024.

Girshick, A., D. G. Pettifor, and V. Vitek. 1998. “Atomistic Simulation of Titanium. II. Structure of ⅓< 1 2 1 0> Screw Dislocations and Slip Systems in Titanium.” *Philosophical Magazine A* 77 (4): 999–1012.

Groh, S., E. B. Marin, M. F. Horstemeyer, and D. J. Bammann. 2009. “Dislocation Motion in Magnesium: A Study by Molecular Statics and Molecular Dynamics.” *Modelling and Simulation in Materials Science and Engineering* 17 (7): 075009. doi:10.1088/0965-0393/17/7/075009.

Hanson, B. H. 1986. “Present and Future Uses of Titanium in Engineering.” *Materials & Design* 7 (6): 301–7.

Harmer, Martin P. 2011. “The Phase Behavior of Interfaces.” *Science* 332 (6026): 182–83. doi:10.1126/science.1204204.

Henkelman, Graeme, Blas P. Uberuaga, and Hannes Jónsson. 2000. “A Climbing Image Nudged Elastic Band Method for Finding Saddle Points and Minimum Energy Paths.” *The Journal of Chemical Physics* 113 (22): 9901–4.

Hennig, R. G., T. J. Lenosky, D. R. Trinkle, S. P. Rudin, and J. W. Wilkins. 2008. “Classical Potential Describes Martensitic Phase Transformations between the A, B, and $ømega$ Titanium Phases.” *Physical Review B* 78 (5): 054121.

Hennig, Richard G., Dallas R. Trinkle, Johann Bouchet, Srivilliputhur G. Srinivasan, Robert C. Albers, and John W. Wilkins. 2005. “Impurities Block the A to $ømega$ Martensitic Transformation in Titanium.” *Nature Materials* 4 (2): 129–33.

Hirth, John P., and Jens Lothe. 1982. “Theory of Dislocations.” http://www.citeulike.org/group/1496/article/810651.

Hohenberg, P., and W. Kohn. 1964. “Inhomogeneous Electron Gas.” *Physical Review* 136 (3B): B864–71. doi:10.1103/PhysRev.136.B864.

Huber, Liam, Jörg Rottler, and Matthias Militzer. 2014. “Atomistic Simulations of the Interaction of Alloying Elements with Grain Boundaries in Mg.” *Acta Materialia* 80 (November): 194–204. doi:10.1016/j.actamat.2014.07.047.

Jin, Hao, Ilya Elfimov, and Matthias Militzer. 2014. “Study of the Interaction of Solutes with Σ5 (013) Tilt Grain Boundaries in Iron Using Density-Functional Theory.” *Journal of Applied Physics* 115 (9): 093506. doi:10.1063/1.4867400.

Kelchner, Cynthia L., S. J. Plimpton, and J. C. Hamilton. 1998. “Dislocation Nucleation and Defect Structure during Surface Indentation.” *Physical Review B* 58 (17): 11085–88. doi:10.1103/PhysRevB.58.11085.

Kiejna, Adam, and Elwira Wachowicz. 2008. “Segregation of Cr Impurities at Bcc Iron Surfaces: First-Principles Calculations.” *Physical Review B* 78 (11): 113403. doi:10.1103/PhysRevB.78.113403.

Kohn, W., and L. J. Sham. 1965. “Self-Consistent Equations Including Exchange and Correlation Effects.” *Physical Review* 140 (4A): A1133–38. doi:10.1103/PhysRev.140.A1133.

Kresse, Georg, and Jürgen Hafner. 1993. “Ab Initio Molecular Dynamics for Liquid Metals.” *Physical Review B* 47 (1): 558.

Kresse, G., and J. Furthmüller. 1996a. “Efficiency of Ab-Initio Total Energy Calculations for Metals and Semiconductors Using a Plane-Wave Basis Set.” *Computational Materials Science* 6 (1): 15–50. doi:10.1016/0927-0256(96)00008-0.

———. 1996b. “Efficient Iterative Schemes for Ab Initio Total-Energy Calculations Using a Plane-Wave Basis Set.” *Physical Review B* 54 (16): 11169–86. doi:10.1103/PhysRevB.54.11169.

Kresse, G., and J. Hafner. 1993. “Ab Initio Molecular Dynamics for Open-Shell Transition Metals.” *Physical Review B* 48 (17): 13115–18. doi:10.1103/PhysRevB.48.13115.

Kresse, G., and D. Joubert. 1999. “From Ultrasoft Pseudopotentials to the Projector Augmented-Wave Method.” *Physical Review B* 59 (3): 1758–75. doi:10.1103/PhysRevB.59.1758.

Leclercq, S., C. Nguy, and P. Bensussan. 1989. *Proceedings of the International Conference on the Mechanical Properties of Materials at High Rates of Strain*.

Lee, T. C., I. M. Robertson, and H. K. Birnbaum. 1989. “Prediction of Slip Transfer Mechanisms across Grain Boundaries.” *Scripta Metallurgica* 23 (5): 799–803. doi:10.1016/0036-9748(89)90534-6.

Legrand, B. 1985. “Core Structure of the Screw Dislocations 1/3< 112@ U-0> in Titanium.” *PHIL. MAG. A.* 52 (1): 83–98.

Legrand, Par B. 1984. “Relations Entre La Structure Électronique et La Facilité de Glissement Dans Les Métaux Hexagonaux Compacts.” *Philosophical Magazine B* 49 (2): 171–84.

Leyens, Christoph, and Manfred Peters. 2003. *Titanium and Titanium Alloys*. Wiley Online Library. http://onlinelibrary.wiley.com/doi/10.1002/3527608117.fmatter/summary.

Liu, Z., and G. Welsch. 1988. “Literature Survey on Diffusivities of Oxygen, Aluminum, and Vanadium in Alpha Titanium, Beta Titanium, and in Rutile.” *Metallurgical Transactions A* 19 (4): 1121–25.

Livingston, J. D, and B Chalmers. 1957. “Multiple Slip in Bicrystal Deformation.” *Acta Metallurgica* 5 (6): 322–27. doi:10.1016/0001-6160(57)90044-5.

Li, Xiaoyan, Yujie Wei, Lei Lu, Ke Lu, and Huajian Gao. 2010. “Dislocation Nucleation Governed Softening and Maximum Strength in Nano-Twinned Metals.” *Nature* 464 (7290): 877–80. doi:10.1038/nature08929.

Lu, Gang. 2005. “The Peierls—Nabarro Model of Dislocations: A Venerable Theory and Its Current Development.” In *Handbook of Materials Modeling*, edited by Sidney

Yip, 793–811. Springer Netherlands. http://link.springer.com.ezproxy1.lib.asu.edu/chapter/10.1007/978-1-4020-3286-8_41.

Lu, Gang, Nicholas Kioussis, Vasily V. Bulatov, and Efthimios Kaxiras. 2000a. “The Peierls-Nabarro Model Revisited.” *Philosophical Magazine Letters* 80 (10): 675–82.

———. 2000b. “Generalized Stacking Fault Energy Surfaces and Dislocation Properties of Aluminum.” *Physical Review B* 62 (5): 3099–3108. doi:10.1103/PhysRevB.62.3099.

Lu, K., L. Lu, and S. Suresh. 2009. “Strengthening Materials by Engineering Coherent Internal Boundaries at the Nanoscale.” *Science* 324 (5925): 349–52. doi:10.1126/science.1159610.

Lu, L., X. Chen, X. Huang, and K. Lu. 2009. “Revealing the Maximum Strength in Nanotwinned Copper.” *Science* 323 (5914): 607–10. doi:10.1126/science.1167641.

Luster, J., and M. A. Morris. 1995. “Compatibility of Deformation in Two-Phase Ti-Al Alloys: Dependence on Microstructure and Orientation Relationships.” *Metallurgical and Materials Transactions A* 26 (7): 1745–56. doi:10.1007/BF02670762.

MacLean, Donald. 1957. “Grain Boundaries in Metals.” http://cds.cern.ch/record/233207.

May, Katelun. 2010. “Small Scale Tensile Testing of Titanium Alloys.” The Ohio State University. http://rave.ohiolink.edu/etdc/view?acc_num=osu1282099780.

Mendelev, Mikhail I., and Graeme J. Ackland. 2007. “Development of an Interatomic Potential for the Simulation of Phase Transformations in Zirconium.” *Philosophical Magazine Letters* 87 (5): 349–59.

Minato, Taketoshi, Yasuyuki Sainoo, Yousoo Kim, Hiroyuki S. Kato, Ken-ichi Aika, Maki Kawai, Jin Zhao, et al. 2009. “The Electronic Structure of Oxygen Atom Vacancy and Hydroxyl Impurity Defects on Titanium Dioxide (110) Surface.” *The Journal of Chemical Physics* 130 (12): 124502.

Monkhorst, Hendrik J., and James D. Pack. 1976. “Special Points for Brillouin-Zone Integrations.” *Physical Review B* 13 (12): 5188–92.

Mordehai, D., Y. Ashkenazy, I. Kelson, and G. Makov. 2003. “Dynamic Properties of Screw Dislocations in Cu: A Molecular Dynamics Study.” *Physical Review B* 67 (2): 024112.

Möslang, Anton, and Thierry Wiss. 2006. “Materials for Energy: From Fission towards Fusion.” *Nature Materials* 5 (9): 679–80.

Nabarro, F. R. N. 1947. “Dislocations in a Simple Cubic Lattice.” *Proceedings of the Physical Society* 59 (2): 256. doi:10.1088/0959-5309/59/2/309.

Naka, S., A. Lasalmonie, P. Costa, and L. P. Kubin. 1988. “The Low-Temperature Plastic Deformation of A-Titanium and the Core Structure of a-Type Screw Dislocations.” *Philosophical Magazine A* 57 (5): 717–40. doi:10.1080/01418618808209916.

Nie, J. F., Y. M. Zhu, J. Z. Liu, and Xi-Ya Fang. 2013. “Periodic Segregation of Solute Atoms in Fully Coherent Twin Boundaries.” *Science* 340 (6135): 957–60.

Ogden, H. R., and R. I. Jaffee. 1955. *The Effects of Carbon, Oxygen, and Nitrogen on the Mechanical Properties of Titanium and Titanium Alloys*. Battelle Memorial Inst. Titanium Metallurgical Lab., Columbus, Ohio. http://www.osti.gov/scitech/biblio/4370612.

Okabe, T. H., T. Oishi, and K. Ono. 1992. “Preparation and Characterization of Extra-Low-Oxygen Titanium.” *Journal of Alloys and Compounds* 184 (1): 43–56.

Olmsted, David L., Louis G. Hector Jr, W. A. Curtin, and R. J. Clifton. 2005. “Atomistic Simulations of Dislocation Mobility in Al, Ni and Al/Mg Alloys.” *Modelling and Simulation in Materials Science and Engineering* 13 (3): 371.

Osetsky, Yu N., and David J. Bacon. 2003. “An Atomic-Level Model for Studying the Dynamics of Edge Dislocations in Metals.” *Modelling and Simulation in Materials Science and Engineering* 11 (4): 427.

Partridge, P. G. 2013. “The Crystallography and Deformation Modes of Hexagonal Close-Packed Metals.” http://www.maneyonline.com/doi/abs/10.1179/imr.1967.12.1.169.

Paton, N. E., and W. A. Backofen. 1970. “Plastic Deformation of Titanium at Elevated Temperatures.” *Metallurgical Transactions* 1 (10): 2839–47. doi:10.1007/BF03037822.

Peierls, R. 1940. “The Size of a Dislocation.” *Proceedings of the Physical Society* 52 (1): 34. doi:10.1088/0959-5309/52/1/305.

Pei, Z., L.-F. Zhu, M. Friák, S. Sandlöbes, J. von Pezold, H. W. Sheng, C. P. Race, et al. 2013. “Ab Initio and Atomistic Study of Generalized Stacking Fault Energies in Mg and Mg–Y Alloys.” *New Journal of Physics* 15 (4): 043020. doi:10.1088/1367-2630/15/4/043020.

Perdew, John P., Kieron Burke, and Matthias Ernzerhof. 1997. “Generalized Gradient Approximation Made Simple [Phys. Rev. Lett. 77, 3865 (1996)].” *Physical Review Letters* 78 (7): 1396–1396. doi:10.1103/PhysRevLett.78.1396.

Pettifor, D. G. 1995. *Bonding and Structure of Molecules and Solids*. Clarendon Press.

Plimpton, Steve. 1995. “Fast Parallel Algorithms for Short-Range Molecular Dynamics.” *Journal of Computational Physics* 117 (1): 1–19.

Rajagopalan, M., M. A. Bhatia, M. A. Tschopp, D. J. Srolovitz, and K. N. Solanki. 2014. “Atomic-Scale Analysis of Liquid-Gallium Embrittlement of Aluminum Grain Boundaries.” *Acta Materialia* 73 (July): 312–25. doi:10.1016/j.actamat.2014.04.011.

Randle, Valerie. 2004. “Twinning-Related Grain Boundary Engineering.” *Acta Materialia* 52 (14): 4067–81. doi:10.1016/j.actamat.2004.05.031.

Rao, S. I., A. Venkateswaran, and M. D. Letherwood. 2013. “Molecular Statics and Molecular Dynamics Simulations of the Critical Stress for Motion of a/3 Screw Dislocations in A-Ti at Low Temperatures Using a Modified Embedded Atom Method Potential.” *Acta Materialia* 61 (6): 1904–12. doi:10.1016/j.actamat.2012.12.011.

Robson, J. D., N. Stanford, and M. R. Barnett. 2011. “Effect of Precipitate Shape on Slip and Twinning in Magnesium Alloys.” *Acta Materialia* 59 (5): 1945–56. doi:10.1016/j.actamat.2010.11.060.

Rogers Jr, J. W., K. L. Erickson, D. N. Belton, R. W. Springer, T. N. Taylor, and J. G. Beery. 1988. “Low Temperature Diffusion of Oxygen in Titanium and Titanium Oxide Films.” *Applied Surface Science* 35 (1): 137–52.

Rogers Jr, J. W., K. L. Erickson, D. N. Belton, and S. J. Ward. 1986. “Thermal Diffusion of Oxygen in Titanium and Titanium Oxide Films.” *Journal of Vacuum Science & Technology A* 4 (3): 1685–87.

Sangid, Michael D., Tawhid Ezaz, Huseyin Sehitoglu, and Ian M. Robertson. 2011. “Energy of Slip Transmission and Nucleation at Grain Boundaries.” *Acta Materialia* 59 (1): 283–96. doi:10.1016/j.actamat.2010.09.032.

Schoeck, Gunther. 1999. “Peierls Energy of Dislocations: A Critical Assessment.” *Physical Review Letters* 82 (11): 2310–13. doi:10.1103/PhysRevLett.82.2310.

Semlitsch, M., F. Staub, and H. Weber. 1985. “Development of a Vital, High-Strength Titanium–Aluminium–Niobium Alloy for Surgical Implants.” *Biological and Biomechanical Performance of Biomaterials*, 69–74.

Serra, A., R. C. Pond, and D. J. Bacon. 1991. “Computer Simulation of the Structure and Mobility of Twinning Disclocations in HCP Metals.” *Acta Metallurgica et Materialia* 39 (7): 1469–80.

Shen, Z., R. H. Wagoner, and W. A. T. Clark. 1986. “Dislocation Pile-up and Grain Boundary Interactions in 304 Stainless Steel.” *Scripta Metallurgica* 20 (6): 921–26. doi:10.1016/0036-9748(86)90467-9.

———. 1988. “Dislocation and Grain Boundary Interactions in Metals.” *Acta Metallurgica* 36 (12): 3231–42. doi:10.1016/0001-6160(88)90058-2.

Solanki, Kiran N., Mark A. Tschopp, Mehul A. Bhatia, and Nathan R. Rhodes. 2013. “Atomistic Investigation of the Role of Grain Boundary Structure on Hydrogen Segregation and Embrittlement in A-Fe.” *Metallurgical and Materials Transactions A* 44 (3): 1365–75.

Song, Y, ZX Guo, and R Yang. 2002. “Influence of Interstitial Elements on the Bulk Modulus and Theoretical Strength of a-Titanium: A First-Principles Study.” *Philosophical Magazine A* 82 (7): 1345–59.

Stillinger, Frank H., and Thomas A. Weber. 1985. “Computer Simulation of Local Order in Condensed Phases of Silicon.” *Physical Review B* 31 (8): 5262–71. doi:10.1103/PhysRevB.31.5262.

Stringer, J. 1960. “The Oxidation of Titanium in Oxygen at High Temperatures.” *Acta Metallurgica* 8 (11): 758–66.

Sun, D. Y., M. I. Mendelev, C. A. Becker, K. Kudin, Tomorr Haxhimali, M. Asta, J. J. Hoyt, A. Karma, and D. J. Srolovitz. 2006. “Crystal-Melt Interfacial Free Energies in Hcp Metals: A Molecular Dynamics Study of Mg.” *Physical Review B* 73 (2): 024116.

Sutton, A. P., M. W. Finnis, D. G. Pettifor, and Y. Ohta. 1988. “The Tight-Binding Bond Model.” *Journal of Physics C: Solid State Physics* 21 (January): 35. doi:10.1088/0022-3719/21/1/007.

Sutton, A. P., and V. Vitek. 1983. “On the Structure of Tilt Grain Boundaries in Cubic Metals I. Symmetrical Tilt Boundaries.” *Philosophical Transactions of the Royal Society of London. Series A, Mathematical and Physical Sciences* 309 (1506): 1–36.

Thorwarth, G., S. Mändl, and B. Rauschenbach. 2000. “Plasma Immersion Ion Implantation Using Titanium and Oxygen Ions.” *Surface and Coatings Technology* 128: 116–20.

Trinkle, Dallas R., and Christopher Woodward. 2005. “The Chemistry of Deformation: How Solutes Soften Pure Metals.” *Science* 310 (5754): 1665–67.

Trinkle, D. R. 2007. “Lattice and Elastic Constants of Titanium–niobium Monoborides Containing Aluminum and Vanadium.” *Scripta Materialia* 56 (4): 273–76.

Trinkle III, Dallas Rhea. 2003. “A Theoretical Study of the HCP to Omega Martensitic Phase Transition in Titanium.” The Ohio State University. https://etd.ohiolink.edu/!etd.send_file?accession=osu1070481734&disposition=attachment.

Tschopp, Mark A., K. N. Solanki, Fei Gao, Xin Sun, Mohammad A. Khaleel, and M. F. Horstemeyer. 2012. “Probing Grain Boundary Sink Strength at the Nanoscale: Energetics and Length Scales of Vacancy and Interstitial Absorption by Grain Boundaries in A-Fe.” *Physical Review B* 85 (6): 064108.

Udler, D., and D. N. Seidman. 1998. “Solute Segregation at [001] Tilt Boundaries in Dilute F.c.c. Alloys.” *Acta Materialia* 46 (4): 1221–33. doi:10.1016/S1359-6454(97)00297-8.

Van Swygenhoven, H., P. M. Derlet, and A. G. Frøseth. 2004. “Stacking Fault Energies and Slip in Nanocrystalline Metals.” *Nature Materials* 3 (6): 399–403.

Vitek, V. 2005. “Dislocation Cores and Unconventional Properties of Plastic Behavior.” In *Handbook of Materials Modeling*, edited by Sidney Yip, 2883–96. Springer Netherlands. http://link.springer.com.ezproxy1.lib.asu.edu/chapter/10.1007/978-1-4020-3286-8_174.

Vitek, V., and M. Igarashi. 1991. “Core Structure of ⅓< 11 2 0> Screw Dislocations on Basal and Prismatic Planes in Hcp Metals: An Atomistic Study.” *Philosophical Magazine A* 63 (5): 1059–75.

Vitek, V., and V. Paidar. 2008. “Non-Planar Dislocation Cores: A Ubiquitous Phenomenon Affecting Mechanical Properties of Crystalline Materials.” *Dislocations in Solids* 14: 439–514.

Wang, J., I. J. Beyerlein, and J. P. Hirth. 2012. “Nucleation of Elementary $\{\bar {1}\,0\,1\,1\}$ and $\{\bar {1}\,0\,1\,3\}$ Twinning Dislocations at a Twin Boundary in Hexagonal Close-Packed Crystals.” *Modelling and Simulation in Materials Science and Engineering* 20 (2): 024001. doi:10.1088/0965-0393/20/2/024001.

Wang, Jian, and Irene J. Beyerlein. 2012a. “Atomic Structures of Symmetric Tilt Grain Boundaries in Hexagonal Close Packed (hcp) Crystals.” *Modelling and Simulation in Materials Science and Engineering* 20 (2): 024002.

———. 2012b. “Atomic Structures of [0\bar{1}10] Symmetric Tilt Grain Boundaries in Hexagonal Close-Packed (hcp) Crystals.” *Metallurgical and Materials Transactions A* 43 (10): 3556–69. doi:10.1007/s11661-012-1177-6.

Wang, Jian N. 1996. “A New Modification of the Formulation of Peierls Stress.” *Acta Materialia* 44 (4): 1541–46. doi:10.1016/1359-6454(95)00273-1.

Wang, Leyun, R. I. Barabash, Y. Yang, T. R. Bieler, M. A. Crimp, P. Eisenlohr, W. Liu, and Gene E. Ice. 2011. “Experimental Characterization and Crystal Plasticity Modeling of Heterogeneous Deformation in Polycrystalline A-Ti.” *Metallurgical and Materials Transactions A* 42 (3): 626–35.

Wang, L., Y. Yang, P. Eisenlohr, T. R. Bieler, M. A. Crimp, and D. E. Mason. 2010. “Twin Nucleation by Slip Transfer across Grain Boundaries in Commercial Purity Titanium.” *Metallurgical and Materials Transactions A* 41 (2): 421–30. doi:10.1007/s11661-009-0097-6.

Wang, Y. M., J. Y. Huang, T. Jiao, Y. T. Zhu, and A. V. Hamza. 2007. “Abnormal Strain Hardening in Nanostructured Titanium at High Strain Rates and Large Strains.” *Journal of Materials Science* 42 (5): 1751–56.

White, C. L., and W. A. Coghlan. 1977. “The Spectrum of Binding Energies Approach to Grain Boundary Segregation.” *Metallurgical Transactions A* 8 (9): 1403–12. doi:10.1007/BF02642853.

Williams, J. C., A. W. Sommer, and P. P. Tung. 1972. “The Influence of Oxygen Concentration on the Internal Stress and Dislocation Arrangements in A Titanium.” *Metallurgical Transactions* 3 (11): 2979–84. doi:10.1007/BF02652870.

Wu, Henry H., and Dallas R. Trinkle. 2011. “Direct Diffusion through Interpenetrating Networks: Oxygen in Titanium.” *Physical Review Letters* 107 (4): 045504. doi:10.1103/PhysRevLett.107.045504.

Wu, Xiaozhi, Rui Wang, and Shaofeng Wang. 2010. “Generalized-Stacking-Fault Energy and Surface Properties for HCP Metals: A First-Principles Study.” *Applied Surface Science* 256 (11): 3409–12.

Xing, H., and J. Sun. 2008. “Mechanical Twinning and Omega Transition By< 111>${$112$}$ Shear in a Metastable Β Titanium Alloy.” *Applied Physics Letters* 93 (3): 031908–031908.

Yamaguchi, Masatake, Motoyuki Shiga, and Hideo Kaburaki. 2005. “Grain Boundary Decohesion by Impurity Segregation in a Nickel-Sulfur System.” *Science* 307 (5708): 393–97.

Zaefferer, S. 2003. “A Study of Active Deformation Systems in Titanium Alloys: Dependence on Alloy Composition and Correlation with Deformation Texture.” *Materials Science and Engineering: A* 344 (1–2): 20–30. doi:10.1016/S0921-5093(02)00421-5.

Zeng, L., and T. R. Bieler. 2005. "Effects of Working, Heat Treatment, and Aging on Microstructural Evolution and Crystallographic Texture of Α, Α′, Α ″and Β Phases in Ti–6Al–4V Wire." *Materials Science and Engineering: A* 392 (1): 403–14.

Zhang, Xu, and Gang Lu. 2007. "Quantum Mechanics/molecular Mechanics Methodology for Metals Based on Orbital-Free Density Functional Theory." *Physical Review B* 76 (24): 245111. doi:10.1103/PhysRevB.76.245111.

Zhang, Xu, Gang Lu, and W. A. Curtin. 2013. "Multiscale Quantum/atomistic Coupling Using Constrained Density Functional Theory." *Physical Review B* 87 (5): 054113.

Zhao, Qingsheng, Robert C. Morrison, and Robert G. Parr. 1994. "From Electron Densities to Kohn-Sham Kinetic Energies, Orbital Energies, Exchange-Correlation Potentials, and Exchange-Correlation Energies." *Physical Review A* 50 (3): 2138.

Zhao, Qingsheng, and Robert G. Parr. 1993. "Constrained-search Method to Determine Electronic Wave Functions from Electronic Densities." *The Journal of Chemical Physics* 98 (1): 543–48. doi:10.1063/1.465093.

Zhao, Yi, and Gang Lu. 2011. "QM/MM Study of Dislocation—hydrogen/helium Interactions in Α-Fe." *Modelling and Simulation in Materials Science and Engineering* 19 (6): 065004.

Zope, Rajendra R., and Yu Mishin. 2003. "Interatomic Potentials for Atomistic Simulations of the Ti-Al System." *Physical Review B* 68 (2): 024102.

APPENDIX A

QM/MM METHODOLOGY AND IMPLEMENTATION

The total energy of the QM/MM system can be expressed as

$$E_{\mathrm{tot}} = E^{\mathrm{DFT}}[\rho_{\mathrm{QM}}; \vec{R}_{\mathrm{QM}}] + E^{\mathrm{MM}}[\vec{R}_{\mathrm{II}} \cup \vec{R}_{\mathrm{MM}}] - E^{\mathrm{MM}}[\vec{R}_{\mathrm{II}}] \qquad \text{(A1)}$$

where the first term denotes the energy of the entire QM region calculated via the constrained DFT. The last two terms are the energy of the combined region II/MM region and the region-II, respectively, as determined by the empirical MM simulations. $\vec{R}_{\mathrm{QM}}$, $\vec{R}_{\mathrm{II}}$, and $\vec{R}_{\mathrm{MM}}$ represent atomic coordinates in the QM region, region II, and MM region, respectively. ρ_{QM} indicates the QM charge density. As a key component of the QM/MM method, the constrained DFT allows a self-consistent determination of ρ_{QM} by constraining it to a predetermined charge density in the boundary region. The essence of the QM/MM method is to ensure that the QM region is treated in the presence of the appropriate boundary conditions provided by the charge density and potentials of the MM atoms. The technical details and validations of the QM/MM method can be found elsewhere. As shown in Figure 1, the entire dislocation system was partitioned into three regions. The QM region (I+II) had 196 atoms containing the dislocation core with/without oxygen impurity and the MM region (III) consists of the rest of the system (11926 atoms) including the long-range elastic field of the dislocation. The overall dimensions of different regions were: 30 Å x 27 Å x 9.26 Å for the region-I and region-II, and 143.67 Å x 155.07 Å x 9.26 Å for the region-III. The length along the dislocation line [0001] was set to 2*c* (*c* = 4.645 Å) to avoid interaction of oxygen atoms due to periodic boundary conditions.

Projector augmented wave (PAW) potentials were used to represent the nuclei core with valence electrons on *s* and *d* orbitals for α-Ti and valence electrons on *s* and *p* orbitals for oxygen atoms. Exchange and correlation was treated with GGA using the PBE form with an energy cutoff of 289 eV and the Monkhorst Pack k-point mesh of 1 x 1 x 5 along the $[1\bar{2}10]$, $[10\bar{1}0]$, and [0001], respectively. The ionic relaxation was carried out using a conjugate gradient algorithm with 30 meV/Å force and 1 meV energy convergence criteria. Moreover, for the pipe diffusion of an oxygen atom, the energy barrier was studied using the C-NEB method with sixteen intermediate images between the global minimums.

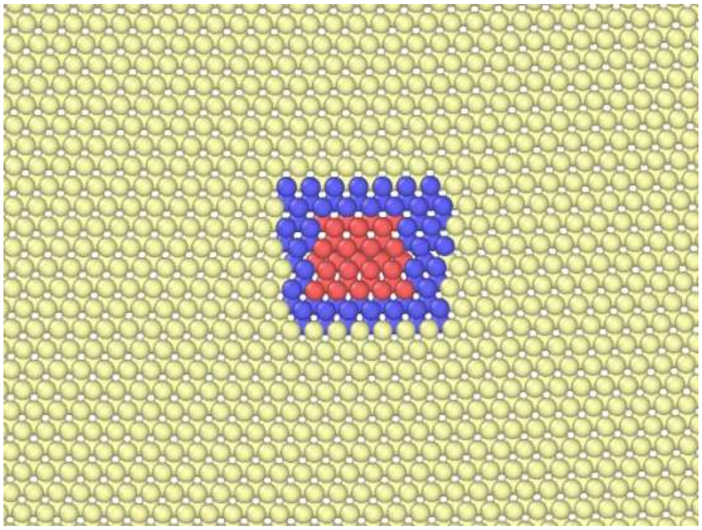

Figure 36: The prismatic edge dislocation core with different QM/MM regions. Red and blue atoms represent regions-I and II, respectively which were solved using the constrained DFT; whereas, yellow atoms belong to region-III solved using the MM approximation. There is no significant deformation in region-II. The overall dimensions of different regions were: 30 Å x 27 Å x 9.26 Å for region-I and region-II and 143.67 Å x 155.07 Å x 9.26 Å for region-III.

APPENDIX B

INTERATOMIC POTENTIAL AND CRYSTAL PROPERTIES

The semi-empirical embedded atom potential (EAM) developed by Zope and Mishin was used to model the defect free EAM region (region-III) in the QM/MM. This EAM potential was parameterized using an extensive database of energies and configurations from DFT calculations and has been used to accurately define different material behaviors such as surface energies, GSFEs, etc. Furthermore, Table 4 lists the lattice properties of Ti with EAM potential and their comparison with DFT data. The EAM potential was modified to match both the lattice constant and bulk modulus of DFT to minimize the misfit energy at the boundary of coupling.